CHAPTER 4

Motion control for passive rehabilitation

4.1 Overview

Passive rehabilitation is applied in early stages of the recovery process and it is based in mobilizing the articulations while the subjects leave their limbs inert. This kind of therapy requires a precise motion control for the articular positions.

In robot-assisted rehabilitation, it is not only important the performance of the device in applying the therapy to the subject, but the safety and efficiency are also critical aspects that should be addressed in the design of the robots as well as in their controllers. Efficiency can be fundamentally quantified or evaluated as the necessary time to don the exoskeleton, to place the sensors and to configure all the parameters for the application. Basically, this is the time that elapses between the entrance of the patient to the rehabilitation room and when the rehabilitation starts. From here on, this period will be named setup time. Also, the doffing time of the exoskeleton is important. An exoskeleton can be very good at applying the rehabilitation in terms of precision, adaptability and comfort, but its applicability to a real rehabilitation environment can be hindered, for example, by long configuration times. The research in all this kind of technologies must consider all these aspects in the design stages. It is true that the researchers should not be thinking in a final product when conducting preliminary research, but these ideas should definitely be in the list of requirements of any robotic rehabilitation device. Very often, an improvement in the performance of an exoskeleton can be associated to adding a new sensor. When considering that improvement, the impact that adding that sensor might have in the safety and stability of the control system should be analyzed (asking oneself questions such as "what could happen if the sensor unexpectedly moved?", "what risks does this imply?"), as well as the impact in the setup time.

The relevant exoskeleton aspects as precision, comfort, setup time and safety can be weighted differently, giving more importance to some of them and less to others. In this context, the work conducted in this thesis proposes two different control architectures for passive rehabilitation with ExoFlex, based on different criteria, each of them with different goals, advantages and disadvantages. The first one is a novel and complex control architecture: a cascade PI-SMC NDO-based motion controller. This controller has been named by the acronym CPISDO. The designed motion control architecture was conceived to control the shoulder and elbow flexion and extension movements for ExoFlex v1 (Section 3.2.2). In this case, articular motion was constrained to the sagittal plane, and it was measured with two IMUs, one placed on the upper-arm and the other one on the forearm. Precision in trajectory tracking, reduced setup time and adaptability to different users were prioritized. The major concern of this architecture is that, as the articular motion feedback is based on the IMU signals, misalignments due to relative movement of the sensor with respect to the subject's arm not only could generate positioning error of the articulations, but also could generate a safety issue if the limbs movement is not measured by the sensors.

According to what was observed in tests performed with subjects, relative movements of the sensors with respect to the subject's arms are relatively likely to happen at some point of the therapy. With the objective of avoiding these potential problems, a positioning algorithm based on a geometrical method was proposed. This method for shoulder positioning was designed for ExoFlex v2 (Section 3.2.3) and, instead of measuring motion feedback obtained by means of on-body sensors, the

angle of the shoulder is estimated via the robot's end effector position and the length of the cable released. Using this method, the position of each actuator is individually controlled, leading to a much simpler control architecture.

In the following subsections, the two proposed control techniques for passive rehabilitation are developed in depth. At the end of this chapter, a discussion posing the advantages and disadvantages of the two designed control methods is presented.

4.2 Cascade PI-SMC NDO-based controller

A cascade PI-SMC (Sliding Mode Controller) based on a NDO (Nonlinear Disturbance Observer) for motion control was designed for ExoFlex v1 of the exoskeleton (Section 3.2.2). The objective was to obtain a robust controller for flexion and extension movements of both elbow and shoulder, with low RMSE in trajectory tracking, to perform passive rehabilitation. Robustness to external disturbances and anatomical variations is necessary to achieve the goal. Moreover, the time invested in parameter tuning for each subject should be as short as possible since setup time is a crucial factor if this system is to be used in real rehabilitation environments. The economical viability of the use of the device in a rehabilitation center could depend on the time invested in this process, so reducing this period to the minimum or even avoiding the need of going through a tuning stage is crucial. This work was published in the author's publication *"Robust motion control architecture for an upper-limb rehabilitation Exosuit"*, IEEE Access, vol. 10, pp. 113631–113648, 2022. doi: 10.1109/ACCESS.2022.3217528.

4.2.1 System model

Due to the difficultly identifiable or quantifiable nonlinear phenomena present in the system (for example, hysteresis and slacks due to the wearable part of the exoskeleton) the obtention of a detailed and accurate model for the system is a difficult process. Additionally, model parameters will surely vary among different users, or they can even vary for a single user when using the exoskeleton in different moments. It is for all these reasons that it was decided to develop a robust controller that can account for all the unmodelled uncertainties and nonlinear behavior rather than trying to obtain a very complex and accurate system model.

Following the aforementioned approach, a simple two-rigid-bar mechanism was used to model the user's arm, as Fig. 4.1 shows. As the design of this controller is only focused in flexion and extension movements, motion is constrained to the sagittal plane, so both elbow and shoulder are adducted. Upper-limb dynamics were modelled employing the Euler-Lagrange method. To model the torque transmission through the cables between the motors and the human articulations, DC motors' differential equations were used. Two important modelling aspects are presented in the following subsections, prior to addressing the state-space model overall structure. Table. 4.1 gathers the main geometrical parameters involved in Fig. 4.1.

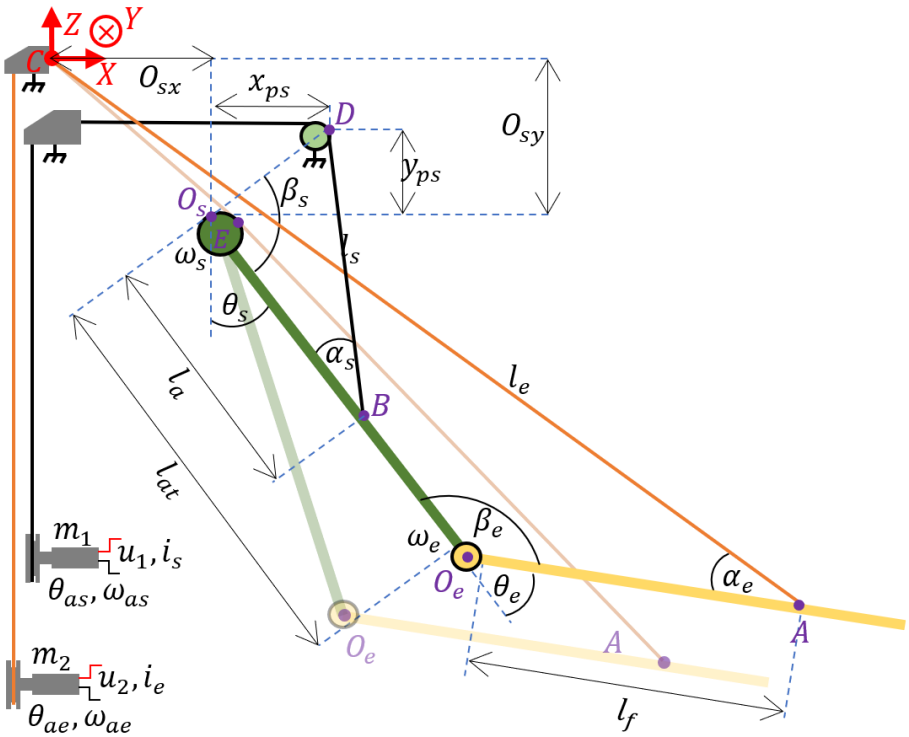


Figure 4.1: Exoskeleton model diagram. Contactless configuration between elbow cable and shoulder is painted in solid color. The contact configuration is shaded. Source: Author's publication ©David Pont Esteban et al. 2022; published by IEEE (http://doi.org/10.1109/ACCESS.2022.321 7528).

Table 4.1: Geometrical model parameters description.

Symbol	Description
A	Elbow cable anchor point
B	Shoulder cable anchor point
C	Elbow cable pivot point. Coordinate origin
D	Shoulder cable pivot point
E	Contact point between elbow cable and shoulder
O_{s}	Shoulder rotation center
O_{e}	Elbow rotation center
l_{s}	Shoulder cable length
l_{s}	Elbow cable length
θ_{x}	Shoulder or elbow flexion angle
θ_{ax}	Actuators' angles
ω_{x}	Shoulder or elbow articular speeds
ω_{ax}	Actuators' speeds
α_{x}	Cable insertion angle

Torque transmission

The torques applied by the exoskeleton to shoulder and elbow (τ_{exos}, τ_{exoe}) are due to the tension of the cables pulling the user's arm at the anchor points. These torques are determined by the tensions in the cables (T_{s}, T_{e}), the cable insertion angles and

the distances between the anchor points and the rotation axes. The torques applied to the articulations are defined by (4.1) and (4.2):

$$\tau_{\text{exos}}(t) = \mathrm{l_a} T_{\mathrm{s}}(t) \sin(\alpha_{\mathrm{s}}(t)) \tag{4.1}$$

$$\tau_{\text{exoe}}(t) = \mathrm{l_f} T_{\mathrm{e}}(t) \sin(\alpha_{\mathrm{e}}(t)) \tag{4.2}$$

Solving the triangle defined by the points $O_{\mathrm{s}}BD$, the shoulder cable angle α_{s} is easily obtained according to (4.3) to (4.5):

$$\alpha_{\mathrm{s}}(t) = \arcsin\left(\frac{\sin(\beta_{\mathrm{s}})\sqrt{\mathrm{x_{ps}^2} + \mathrm{y_{ps}^2}}}{l_{\mathrm{s}}(t)}\right) \tag{4.3}$$

$$l_{\mathrm{s}}(\theta_{\mathrm{s}}) = \sqrt{\left(\mathrm{l_a}\sin(\theta_{\mathrm{s}}) - \mathrm{x_{ps}}\right)^2 + \left(\mathrm{l_a}\cos(\theta_{\mathrm{s}}) + \mathrm{y_{ps}}\right)^2} \tag{4.4}$$

$$\beta_{\mathrm{s}} = \pi - \theta_{\mathrm{s}} - \arctan\left(\frac{\mathrm{x_{ps}}}{\mathrm{y_{ps}}}\right) \tag{4.5}$$

Nevertheless, there exist two geometrically different situations to obtain α_{e} according to the articular positions. In the first one, there does not exist contact between the shoulder and the elbow cable (solid drawing in Fig. 4.1). In this case, the triangle to be solved is determined by $CO_{\mathrm{e}}A$. In the second one, there exists contact between the shoulder and the elbow cable, and the triangle for this case is given by $EO_{\mathrm{e}}A$. For both geometrical configurations, the insertion angle for the elbow cable can be computed using (4.6) to (4.8):

$$\alpha_{\mathrm{e}}(t) = \arcsin\left(\frac{\sin(\beta_{\mathrm{e}})\,|\vec{\mathbf{q}}|}{l_{\mathrm{e}}(t)}\right) \tag{4.6}$$

$$\beta_{\mathrm{e}} = \arccos\left(\frac{\vec{\mathbf{q}} \cdot \overrightarrow{\mathbf{O_eA}}}{|\vec{\mathbf{q}}|\,|\overrightarrow{\mathbf{O_eA}}|}\right) \tag{4.7}$$

$$l_{\mathrm{e}}(\theta_{\mathrm{s}}, \theta_{\mathrm{e}}) = \sqrt{|\vec{\mathbf{q}}|^2 + \mathrm{l_f^2} + 2\mathrm{l_f}\,|\vec{\mathbf{q}}|\cos(\beta_{\mathrm{e}})} \tag{4.8}$$

For the contactless situation, $\vec{\mathbf{q}} = \overrightarrow{\mathbf{CO_e}} = (\mathrm{l_{at}}\sin(\theta_{\mathrm{s}}) + \mathrm{O_{sx}},\ -\mathrm{l_{at}}\cos(\theta_{\mathrm{s}}) - \mathrm{O_{sy}})$ and in the contact situation $\vec{\mathbf{q}} = \overrightarrow{\mathbf{EO_e}} = (\mathrm{l_{at}}\sin(\theta_{\mathrm{s}}) + \mathrm{E_x},\ -\mathrm{l_{at}}\cos(\theta_{\mathrm{s}}) - \mathrm{E_y})$. As the coordinates of A are known, it is straightforward to determine weather there exists contact or not.

Relation between actuator and articular speeds

Assuming that the transmission cables are not deformable, the linear speed v of the cable at the motor side is obviously the same as at the arm one. Choosing, for example, the shoulder cable, the linear speed can be described in terms of the shoulder actuator angular variation (4.9) and as a function of the shoulder angular variation (4.10):

$$v = \frac{\mathrm{d}l_{\mathrm{s}}(\theta_{\mathrm{as}})}{\mathrm{d}\theta_{\mathrm{as}}}\frac{\mathrm{d}\theta_{\mathrm{as}}}{\mathrm{d}t} = -\mathrm{r}\dot{\theta}_{\mathrm{as}}(t) \tag{4.9}$$

$$v = \frac{\mathrm{d}l_{\mathrm{s}}(\theta_{\mathrm{s}})}{\mathrm{d}\theta_{\mathrm{s}}}\frac{\mathrm{d}\theta_{\mathrm{s}}}{\mathrm{d}t} = \left(-\mathrm{l_a}\frac{\mathrm{x_{ps}}\cos(\theta_{\mathrm{s}}) + \mathrm{y_{ps}}\sin(\theta_{\mathrm{s}})}{l_{\mathrm{s}}(\theta_{\mathrm{s}})}\right)\dot{\theta}_{\mathrm{s}}(t) \tag{4.10}$$

being r the radius of the motor pulleys over which the cable winds. Articular speeds are considered positive in the positive Z axis direction in Fig. 4.1. Dividing (4.10) by (4.9) and reordering terms, the relationship between the actuator and articulation speed is obtained:

$$\dot{\theta}_{\mathrm{as}}(t) = \frac{\mathrm{l_a}}{\mathrm{r}} \left(\frac{\mathrm{x_{ps}} \cos(\theta_{\mathrm{s}}) + \mathrm{y_{ps}} \sin(\theta_{\mathrm{s}})}{l_s(\theta_{\mathrm{s}})} \right) \dot{\theta}_{\mathrm{s}}(t) \tag{4.11}$$

If the same process is followed, the kinematic relationship for the elbow is derived:

$$\dot{\theta}_{\mathrm{ae}}(t) = -\frac{\mathrm{l_f}}{\mathrm{r}} \left(\frac{q_{\mathrm{x}} \cos(\theta_{\mathrm{e}} + \theta_{\mathrm{s}}) + q_{\mathrm{y}} \sin(\theta_{\mathrm{e}} + \theta_{\mathrm{s}})}{l_{\mathrm{e}}(\theta_{\mathrm{e}})} \right) \dot{\theta}_{\mathrm{e}}(t) \tag{4.12}$$

The acceleration relationships are easily obtained by applying the time derivative to (4.11) and (4.12).

State-space model

The system is a nonlinear system defined by the state equation (4.13), but it is linear in the input

$$\dot{\mathbf{x}}(t) = \mathbf{f}(\mathbf{x}(t)) + \mathbf{g} \cdot \mathbf{u}(t) + \mathbf{g_d} \cdot \mathbf{d}(t) \tag{4.13}$$

with

$$\mathbf{f}(\mathbf{x}) = \Big[x_2, f_2(\mathbf{x}), f_3(\mathbf{x}), x_5, f_5(\mathbf{x}), f_6(\mathbf{x}) \Big]^\intercal$$
$$\mathbf{g} = \begin{bmatrix} 0 & 0 & \mathrm{b} & 0 & 0 & 0 \\ 0 & 0 & 0 & 0 & 0 & \mathrm{b} \end{bmatrix}^\intercal, \ \mathbf{g_d} = \mathbf{I_6}$$

where the number of state variables is $n = 6$, $\mathbf{x} \in \mathbf{X} \subset \mathbb{R}^6$ is the state vector belonging to the state space $\mathbf{X}$, $\mathbf{u} \in \mathbb{R}^2$ is the input vector and $\mathbf{d} \in \mathbb{R}^6$ is the disturbance vector. The model state variables are the shoulder position ($x_1 = \theta_{\mathrm{s}}$), shoulder speed ($x_2 = \dot{\theta}_{\mathrm{s}}$), shoulder motor current ($x_3 = i_{\mathrm{s}}$), elbow position ($x_4 = \theta_{\mathrm{e}}$), elbow speed ($x_5 = \dot{\theta}_{\mathrm{e}}$) and elbow motor current ($x_6 = i_{\mathrm{e}}$). Note that the input matrix $\mathbf{g}$ is constant.

As aforementioned, there exists uncertainty in model parameters. Among many other aspects, these uncertainties include the variability among users in anatomical parameters such as mass, length and inertia of arm and forearm. These can be modelled as additive uncertainties to the state function **f(x)** [138], [139]. In such a manner, **f(x)** can be defined as

$$\mathbf{f}(\mathbf{x}) = \mathbf{f_0}(\mathbf{x}) + \Delta\mathbf{f}(\mathbf{x}) \tag{4.14}$$

being the nominal and uncertainty models respectively

$$\mathbf{f_0}(\mathbf{x}) = \Big[x_2, f_{02}(\mathbf{x}), f_{03}(\mathbf{x}), x_5, f_{05}(\mathbf{x}), f_{06}(\mathbf{x}) \Big]^\intercal$$
$$\Delta\mathbf{f}(\mathbf{x}) = \Big[0, \Delta f_2(\mathbf{x}), \Delta f_3(\mathbf{x}), 0, \Delta f_5(\mathbf{x}), \Delta f_6(\mathbf{x}) \Big]^\intercal$$

The first and fourth elements of $\Delta\mathbf{f}$ are 0 since x_2 and x_5 are simply the derivatives of x_1 and x_4, so there is no model uncertainty in those relations. Considering that $\mathbf{g_d} = \mathbf{I_6}$, the following state equation is obtained

$$\dot{\mathbf{x}}(t) = \mathbf{f_0}(\mathbf{x}) + \mathbf{g} \cdot \mathbf{u}(t) + \mathbf{d}(t) + \Delta\mathbf{f}(\mathbf{x}) \tag{4.15}$$

Combining $\mathbf{d}(t)$ and $\Delta\mathbf{f}(\mathbf{x})$ vectors, the lumped disturbance and uncertainty vector $\mathbf{p}(t)$ is obtained

$$\dot{\mathbf{x}}(t) = \mathbf{f_0}(\mathbf{x}) + \mathbf{g} \cdot \mathbf{u}(t) + \mathbf{p}(t) \tag{4.16}$$

with $\|p_i\|_\infty < \dot{\mathrm{p}}_{\mathrm{i,max}}$. For subsequent control design and controllability analysis, it will be convenient to represent $f_{02}(\mathbf{x})$ and $f_{05}(\mathbf{x})$ as

$$f_{02}(\mathbf{x}) = f_{2b}\left(x_1, x_2, x_4, x_5, x_6\right) + f_{2is}\left(x_1, x_4\right) x_3 \tag{4.17}$$

$$f_{05}(\mathbf{x}) = f_{5b}\left(x_1, x_2, x_3, x_4, x_5\right) + f_{5ie}\left(x_1, x_4\right) x_6 \tag{4.18}$$

where

$$f_{2b}(x) = f_{2a}\left(x_1, x_2, x_4, x_5\right) + f_{2ie}\left(x_1, x_4\right) x_6 \tag{4.19}$$

$$f_{5b}(x) = f_{5a}\left(x_1, x_2, x_4, x_5\right) + f_{5is}\left(x_1, x_4\right) x_3 \tag{4.20}$$

Subscript "*is*" accounts for "*intensity shoulder*", as functions with this subscript are multiplied by the shoulder motor current x_3. Likewise, subscript "*ie*" accounts for "*intensity elbow*". Functions f_{02}, f_{03}, f_{05} and f_{06} depend on the anatomical parameters of the user's arms: mass, length and moment of inertia of both the forearm and the upper arm. Details on these functions can be found in Appendix C.1.

Controllability

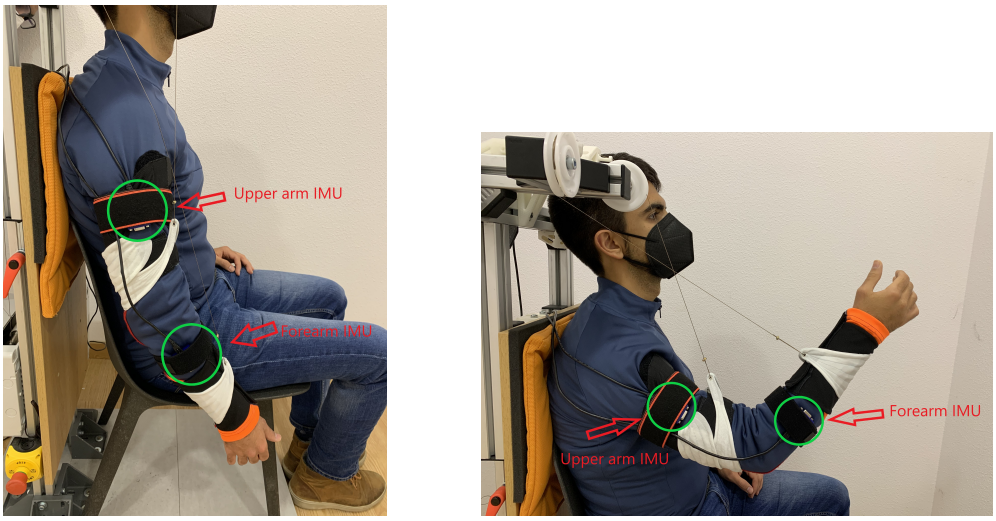
The elbow position is not controllable in all the state space $\mathbf{X}$, and this can be easily understood just thinking about how the system works, without the need to undergo any deeper analysis. In this way, let's assume that the shoulder is positioned at an angle of, for instance, 90°. If the elbow angle is $x_4 \geq 90°$ then, no matter what control action u_2 is applied to the actuator that moves the elbow cable (Fig. 4.1), the elbow will not be able to extend since the cable-driven transmission cannot push the forearm of the subject and gravity does not generate movement in that direction for this specific arm pose. Generalizing this behavior, it can be affirmed that the elbow position x_4 is not controllable if $x_1 + x_4 \geq 180°$, without the need of developing any deeper analysis. The inclusion in the system of another cable to assist elbow extension would solve the controllability issue that arises under the aforementioned circumstances. Nevertheless, this fact does not imply a limitation for the exoskeleton for rehabilitation therapies since elbow rehabilitation therapies are performed with the shoulder in the relaxed position. Although there is clearly a non-controllable subspace, there is a controllable one for which the controllability of the nonlinear system con be proven.

Proposition 1 *Assuming that there exists a subspace* $\mathbf{X_{\bar{c}}} \subset \mathbf{X}$ *given by* $x_1 + x_4 \geq 180°$ *in which the elbow position is not controllable, there exists another* $\mathbf{X_c} \subset \mathbf{X}$ *in which the whole system is controllable. The controllable subspace* $\mathbf{X_c} \ni \forall x_1, x_4 \mid x_1 + x_4 < 180°, x_1 \in [0°, 110°], x_4 \in [0°, 150°]$. *As for the articular speeds and motor currents* $x_2 \in [\omega_{\min}, \omega_{\max}]$, $x_3 \in [\mathrm{i}_{\min}, \mathrm{i}_{\max}]$, *where* $\omega_{\min}$, $\omega_{\max}$, $\mathrm{i}_{\min}$ *and* $\mathrm{i}_{\max}$ *depend on the actuator limitations. At a theoretical level,* $\omega_{\max} = \mathrm{i}_{\max} = \infty$ *and* $\omega_{\min} = \mathrm{i}_{\min} = -\infty$. *Shoulder angle* x_1 *is controllable in all its range of motion, no matter the elbow position* x_4.

Proof for the previous proposition is presented in Appendix C.2.

4.2.2 Motion measurement

Two LPMS-URS2 IMUs were placed on the subjects' arms to measure the angle and angular speed of elbow and shoulder in flexion and extension movements. The upper-arm IMU, used to measure shoulder flexion angle (θ_s), was placed in the external face of the upper-arm, between the biceps and the triceps. The forearm IMU, used to measure elbow flexion angle (θ_e), was located approximately between the wrist flexor group and the brachioradialis, also in the forearm external face. The placement of the IMUs can be observed in Fig. 4.2.



(a) **(b)**

Figure 4.2: Placement of the IMU sensors. Both sensors are placed in the external face of the arm.

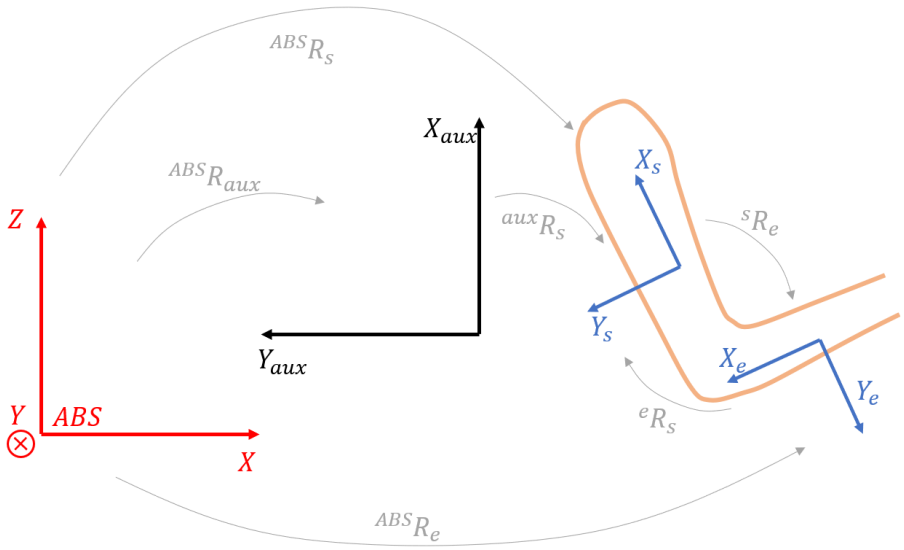


Figure 4.3: Diagram of the frame references and the rotation matrices involved in the obtention of the shoulder and elbow angles and speeds. Subscripts *"s"* and *"e"* stand for shoulder and elbow, respectively.

To obtain the flexion angles and speeds for both articulations, IMU data were processed in the following way (all the mentioned reference axes are represented in

Fig. 4.3). First, both IMUs were placed over a custom designed 3D-printed part for calibration. In this way, the absolute reference axes were placed as shown in the left upper corner of Fig. 4.1. Reference *"aux"* was defined as an intermediate reference that simplifies the obtention of θ_s, as the shoulder flexion angle is measured with respect to the vertical axis X_aux. The data given by the IMUs are expressed as quaternions. Each of the received quaternions expresses the rotation from the IMU reference to the absolute reference. In this way, from the shoulder and IMU quaternions (q_s and q_e, respectively), rotation matrices can be obtained as follows:

$$\boldsymbol{q}_\mathrm{s} \rightarrow {}^{\mathrm{s}}\boldsymbol{R}_\mathrm{ABS}; \quad \boldsymbol{q}_\mathrm{e} \rightarrow {}^{\mathrm{e}}\boldsymbol{R}_\mathrm{ABS} \tag{4.21}$$

The rotation matrix which relates the absolute reference with the *"aux"* reference is defined as two consecutive rotations around Y and X axes of the absolute reference:

$${}^{\mathrm{ABS}}\boldsymbol{R}_\mathrm{aux} = \boldsymbol{Rot}\left(-\frac{\pi}{2}, Y\right) \cdot \boldsymbol{Rot}\left(\frac{\pi}{2}, X\right) \tag{4.22}$$

According to Fig. 4.3, θ_s and θ_e can be obtained as follows:

$${}^{\mathrm{aux}}\boldsymbol{R}_\mathrm{s} = \left({}^{\mathrm{ABS}}\boldsymbol{R}_\mathrm{aux}\right)^{-1} \cdot {}^{\mathrm{ABS}}\boldsymbol{R}_\mathrm{s} \tag{4.23}$$

$$\theta_\mathrm{s} = \mathrm{atan2}\left({}^{\mathrm{aux}}\boldsymbol{R}_\mathrm{s}(1,0), {}^{\mathrm{aux}}\boldsymbol{R}_\mathrm{s}(0,0)\right) \tag{4.24}$$

$${}^{\mathrm{aux}}\boldsymbol{R}_\mathrm{e} = \left({}^{\mathrm{ABS}}\boldsymbol{R}_\mathrm{aux}\right)^{-1} \cdot {}^{\mathrm{ABS}}\boldsymbol{R}_\mathrm{e} \tag{4.25}$$

$$\theta_\mathrm{e} = \mathrm{atan2}\left({}^{\mathrm{aux}}\boldsymbol{R}_\mathrm{e}(1,0), {}^{\mathrm{aux}}\boldsymbol{R}_\mathrm{e}(0,0)\right) \tag{4.26}$$

The IMUs also provide the angular speeds around the three axes of the IMU reference. The shoulder angular speed around the $\mathrm{Z_s}$ axis is the z component of the speed provided by the IMU:

$$\omega_\mathrm{s}\big|_{z\mathrm{s}} = \omega_{\mathrm{IMU,s}}\big|_z \tag{4.27}$$

Similarly, the elbow angular speed around the $\mathrm{Z_e}$ axis is the difference between the angular speed provided by the elbow IMU in that axis and the shoulder flexion speed projected in that reference:

$$\omega_\mathrm{e}\big|_{z\mathrm{e}} = \omega_{\mathrm{IMU,e}}\big|_z - {}^{\mathrm{s}}\boldsymbol{R}_\mathrm{e} \cdot \boldsymbol{\omega}_{\mathrm{IMU,s}} \tag{4.28}$$

4.2.3 Control design

In this section, the exoskeleton motion control design is presented. It is frequent that sliding-mode control designs are developed for systems described in the controllable canonical form in (4.29) [140], [141].

$$\begin{cases} \dot{x}_i = x_{i+1} \\ \vdots \qquad\qquad\qquad i = 1, ..., n-1 \\ \dot{x}_n = f(x) + g \cdot u \end{cases} \tag{4.29}$$

Nevertheless, the system model obtained in Section 4.2.1 is not represented in the controllable canonical form. A coordinate transformation could be applied to obtain a new state vector that allows to represent the system in the controllable canonical form. However, this is not a good approach since, on the one hand, the original state vector is directly measurable, and, on the other hand, applying the

transformation to the measured original state variables would significantly increase the computation time of the controller in the software implementation. It is for these reasons that the controller was designed for the specific model structure presented from (4.13) to (4.20).

The proposed controller represents a significant upgrade to the one presented in [142]. The authors of that work proposed a sliding-mode controller based on a nonlinear disturbance observer for nonlinear SISO systems which are represented in the controllable canonical form with both matched and unmatched uncertainties and disturbances. The approach developed in this thesis extends that controller to a MIMO system which additionally is not represented in the canonical form. The SMC module of the controller provides robustness to matched disturbances and uncertainties. Nevertheless, it cannot handle unmatched ones. Thus, the NDO module was incorporated to estimate the lumped unmatched uncertainties and disturbances and compensate for them. The SMC and the NDO are tightly coupled since, not only the estimated lumped disturbances and uncertainties are used to compute the control actions, but also the sliding surface is modified according to those estimations. With the objective of chattering attenuation, a boundary layer was added. However, the addition of this element increases the tracking error [37]. A PI controller to control the motor current references x_3^{d} and x_6^{d} before they are introduced to the SMC was incorporated to reduce tracking error. The idea which holds this is to vary the current references such that the errors in the articular positions are reduced, which is the ultimate goal of the controller.

Control layout

The CPISDO is a motion controller. In this context, although the state vector x consists of 6 state variables, the reference for the controller consists only of the motion variables: two articular positions and two articular speeds. This vector is denoted as $\mathbf{x}_{\mathrm{m}}^{\mathrm{d}} = [x_1, x_2, x_4, x_5]^\intercal$. It is also necessary to define the articular position reference vector as $\mathbf{x}_{\mathrm{p}}^{\mathrm{d}} = [x_1, x_4]^\intercal$. These vectors are related as follows: the motion reference $\mathbf{x}_{\mathrm{d}}^{\mathrm{m}}$ is the input of the controller. Vector $\mathbf{x}_{\mathrm{p}}^{\mathrm{d}}$ is extracted from $\mathbf{x}_{\mathrm{m}}^{\mathrm{d}}$ and used to compute the position errors $\mathbf{e}_{\mathrm{p}}$. These errors are the input of the PI module of the CPISDO, which generates the motor current references $\mathbf{x}_{\mathrm{c}}^{\mathrm{d}} = [x_3^{\mathrm{d}}, x_6^{\mathrm{d}}]$. The current references $\mathbf{x}_{\mathrm{c}}^{\mathrm{d}}$ are grouped with the motion references $\mathbf{x}_{\mathrm{m}}^{\mathrm{d}}$ to create the full state reference vector $\mathbf{x}^{\mathrm{d}}$, which is the reference for the SMC module of the CPISDO. The control architecture diagram is shown in Fig. 4.4.

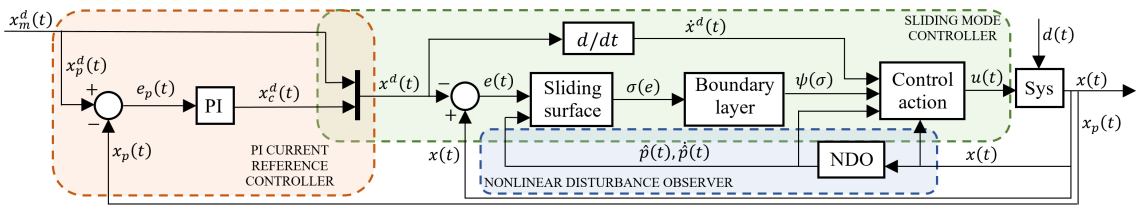


Figure 4.4: Block diagram of the CPISDO controller. The three main modules are shaded as follows: orange for the PI current reference controller, green for the SMC and blue for the nonlinear disturbance observer. Source: Author's publication ©David Pont Esteban et al. 2022; published by IEEE (http://doi.org/10.1109/ACCESS.2022.3217528).

Nonlinear disturbance and uncertainty observer

The nonlinear disturbance observer used in this work is the one presented in [143]. It has been used before in many other works ([142], [144], [145]) to estimate disturbances and increase the robustness of their proposed sliding mode controllers. In the approach developed in this work, the observer estimates the lumped uncertainties and disturbances $\mathbf{p}(t)$ (although, for brevity, it will be called nonlinear disturbance observer), consequently with the model in (4.16). The observer is described by (4.30)

$$\begin{cases} \dot{\mathbf{z}} = -\mathbf{L}\mathbf{g_d}\mathbf{z} - \mathbf{L}\left[\mathbf{g_d}\mathbf{L}\mathbf{x} + \mathbf{f_0}(\mathbf{x}) + \mathbf{g}\mathbf{u}\right] \\ \hat{\mathbf{p}}(t) = \mathbf{z} + \mathbf{L}\mathbf{x} \end{cases} \tag{4.30}$$

where $\hat{\mathbf{p}} \in \mathbb{R}^6$ is the estimation of the disturbance and uncertainty vector $\mathbf{p} \in \mathbb{R}^6$, $\mathbf{z} \in \mathbb{R}^6$ is the internal state vector of the nonlinear observer and $\mathbf{L} \in \mathbb{R}^{6\times6}$ is the observer gain diagonal matrix. Defining the estimation error as $\tilde{\mathbf{p}}(t) = \mathbf{p}(t) - \hat{\mathbf{p}}(t)$, then its dynamics can be derived as

$$\dot{\tilde{\mathbf{p}}}(t) = \dot{\mathbf{p}}(t) - \mathbf{L}\mathbf{g_d}\tilde{\mathbf{p}}(t) \tag{4.31}$$

It is assumed that the unmatched disturbances and uncertainties $\mathbf{p}$ and their derivatives are bounded for the system ([142], [144], [145]). Plus, if they satisfy

$$\lim_{t\to\infty} p_i^{(j)}(t) = 0,\ i = 1, ..., n;\ j = 1, ..., n-1 \tag{4.32}$$

then, the estimation error will converge to 0 asymptotically if $\mathbf{L}$ is chosen such that $\mathbf{L}\mathbf{g_d} > \mathbf{0}$ holds [144].

However, although the assumption in (4.32) is reasonable in some cases, it is not likely to hold in others. Therefore, the estimation error has to be addressed when $\dot{p}_i \neq 0$. The stability and tracking accuracy analysis of the nonlinear observer that proves the following proposition is provided in Appendix C.3.

Proposition 2 *Considering that the lumped uncertainties and disturbances variations are bounded such that* $\|\dot{p}_i\|_\infty < \dot{\mathrm{p}}_{\mathrm{i,max}}$*, the estimation error* $\tilde{\mathbf{p}}(t)$ *of the NDO in (4.30) is globally uniformly ultimately bounded by* $\tilde{p}_i(t) \leq \dot{\mathrm{p}}_{\mathrm{i,max}}/\mathrm{L_{ii}}$*, and the nonlinear observer is globally asymptotically stable.*

It is important to highlight that these bounds are worst-case estimation errors defined by the maximum values of lumped disturbance and uncertainty variations $\dot{\mathrm{p}}_{\mathrm{i,max}}$. The lower the values of $\dot{p}_i$ are, the closer p_i is to meet (4.32) and the more reduced the estimation errors $\tilde{p}_i$ will be.

Sliding mode controller

According to the system model (4.16), the error dynamics are derived as

$$\begin{cases} \dot{e}_1 = x_2 + p_1 - \dot{x}_1^{\mathrm{d}} \\ \dot{e}_2 = f_{2b}(\mathbf{x}) + f_{2is}(\mathbf{x})x_3 + p_2 - \dot{x}_2^{\mathrm{d}} \\ \dot{e}_3 = f_{03}(\mathbf{x}) + bu_1 + p_3 - \dot{x}_3^{\mathrm{d}} \\ \dot{e}_4 = x_5 + p_4 - \dot{x}_4^{\mathrm{d}} \\ \dot{e}_5 = f_{5b}(\mathbf{x}) + f_{5ie}(\mathbf{x})x_6 + p_5 - \dot{x}_5^{\mathrm{d}} \\ \dot{e}_6 = f_{06}(\mathbf{x}) + bu_2 + p_6 - \dot{x}_6^{\mathrm{d}} \end{cases} \tag{4.33}$$

with $e_i = x_i - x_i^{\mathrm{d}}$, being x_i^{d} the reference for the state x_i. Note that f_{2is} and f_{5ie} only depend on x_1 and x_4. Representing the system in this form will be useful for designing the sliding manifolds and for dynamics analysis. The proposed sliding manifolds are defined as

$$\boldsymbol{\sigma} = \begin{bmatrix} \sigma_{\mathrm{s}} \\ \sigma_{\mathrm{e}} \end{bmatrix} = \begin{bmatrix} \sigma_1 e_1 + \sigma_2 e_2 + e_3 + \sigma_2 \hat{p}_1 + \frac{\hat{p}_2 + \dot{\hat{p}}_1}{f_{2is}(x)} \\ \sigma_4 e_4 + \sigma_5 e_5 + e_6 + \sigma_5 \hat{p}_4 + \frac{\hat{p}_5 + \dot{\hat{p}}_4}{f_{5ie}(x)} \end{bmatrix} \tag{4.34}$$

where $\hat{p}_i$ is the estimate of the unmatched disturbances and uncertainties over the i^{th} state variable, $\dot{\hat{p}}_i$ its derivative and σ_1, σ_2, σ_4 and σ_5 are design parameters. The control inputs are designed as

$$u_1(t) = -\frac{1}{\mathrm{b}} \Bigg[\sigma_1 \left(x_2 + \hat{p}_1 - \dot{x}_1^{\mathrm{d}} \right) + \sigma_2 \left(f_{02}(\mathbf{x}) + \hat{p}_2 - \dot{x}_2^{\mathrm{d}} \right) + f_{03}(\mathbf{x}) - \dot{x}_3^{\mathrm{d}} + \mathrm{k_s} \psi(\sigma_s) + \sigma_2 \dot{\hat{p}}_1 + \frac{\mathrm{d}}{\mathrm{d}t} \left(\frac{\hat{p}_2 + \dot{\hat{p}}_1}{f_{2is}(\mathbf{x})} \right) \Bigg] \tag{4.35}$$

$$u_2(t) = -\frac{1}{\mathrm{b}} \Bigg[\sigma_4 \left(x_5 + \hat{p}_4 - \dot{x}_4^{\mathrm{d}} \right) + \sigma_5 \left(f_{05}(\mathbf{x}) + \hat{p}_5 - \dot{x}_5^{\mathrm{d}} \right) + f_{06}(\mathbf{x}) - \dot{x}_6^{\mathrm{d}} + \mathrm{k_e} \psi(\sigma_e) + \sigma_5 \dot{\hat{p}}_4 + \frac{\mathrm{d}}{\mathrm{d}t} \left(\frac{\hat{p}_5 + \dot{\hat{p}}_4}{f_{5ie}(\mathbf{x})} \right) \Bigg] \tag{4.36}$$

being $\mathrm{k_s}$ and $\mathrm{k_e}$ control gains. The boundary layer included to attenuate chattering is defined as

$$\psi(\sigma_j) = \begin{cases} -1 \text{ if } \frac{\sigma_j}{\phi_{\mathrm{j}}} \leq -1 \\ \frac{\sigma_j}{\phi_{\mathrm{j}}} \text{ if } -1 < \frac{\sigma_j}{\phi_{\mathrm{j}}} < 1 \\ 1 \text{ if } \frac{\sigma_j}{\phi_{\mathrm{j}}} \geq 1 \end{cases} \tag{4.37}$$

being ϕ_{j} the width of the boundary layer associated to σ_{s} or σ_{e}.

Remark 1 *Note that in (4.35) and (4.36), the lumped disturbance and uncertainty estimations $\hat{p}_3$ and $\hat{p}_6$ are not included. State variables x_3 and x_6 are the motor currents, which have very fast dynamics and intrinsic coupled noise. Attempting to estimate those disturbances at the specified control frequency (1 kHz) is not feasible. However, p_3 and p_6 are matched disturbances and uncertainties, so they can be directly compensated by the SMC module of the controller.*

Proposition 3 *The controller defined by the control laws (4.35) and (4.36), the sliding manifold (4.34) and the NDO (4.30) for the system (4.16) assures that the system reaches the sliding mode, if* $\mathrm{k_s}$ *and* $\mathrm{k_e}$ *are properly chosen.*

The proof of the previous proposition can be found in Appendix C.4.

Error dynamics in sliding mode

Dynamics of position errors of shoulder and elbow (e_1 and e_4 respectively) when the system is in sliding mode are studied in the present subsection. The mathematical development will only be presented for e_1 dynamics since e_4 ones can be obtained analogously.

When the system is in an ideal sliding mode, the sliding manifold $\sigma_s = 0$, hence, the following equality holds:

$$\sigma_1 e_1 + \sigma_2 \left(x_2 - x_2^{\mathrm{d}}\right) + e_3 + \sigma_2 \hat{p}_1 + \left(\hat{p}_2 + \dot{\hat{p}}_1\right) f_{2is}^{-1}(\mathbf{x}) = 0 \tag{4.38}$$

Solving (4.38) for x_2, solving the second equation of (4.33) for x_3 and substituting both in the first equation of (4.33):

$$\dot{e}_1 = \frac{1}{\sigma_2}\left[- \sigma_1 e_1 - \left(\frac{\dot{x}_2 - f_{2b}(\mathbf{x}) - p_2 + \hat{p}_2 + \dot{\hat{p}}_1}{f_{2is}(\mathbf{x})} \right) + x_3^{\mathrm{d}} \right] + \tilde{p}_1 + x_2^{\mathrm{d}} - \dot{x}_1^{\mathrm{d}} \tag{4.39}$$

From the first equation of (4.33) it can be derived that $\dot{x}_2 = \ddot{x}_1 - \dot{p}_1$. Applying this substitution to (4.39), adding at both sides of the equality the term $-\ddot{x}_1^{\mathrm{d}} \left(\sigma_2 f_{2is}(\mathbf{x})\right)^{-1}$ and rearranging terms, (4.40) is obtained. Analogously, the error dynamics for e_4 are given by (4.41). Recall that $\tilde{p}_i = p_i - \hat{p}_i$.

$$\begin{aligned} \frac{\ddot{e}_1(t)}{\sigma_2 f_{2is}(\mathbf{x})} + \dot{e}_1(t) + \frac{\sigma_1}{\sigma_2} e_1(t) = \frac{f_{2b}(\mathbf{x})}{\sigma_2 f_{2is}(\mathbf{x})} \\ + \frac{x_3^{\mathrm{d}}}{\sigma_2} - \frac{\ddot{x}_1^{\mathrm{d}}(t)}{\sigma_2 f_{2is}(\mathbf{x})} + \tilde{p}_1(t) + \frac{\tilde{p}_2(t)}{\sigma_2 f_{2is}(\mathbf{x})} + \frac{\dot{\tilde{p}}_1(t)}{\sigma_2 f_{2is}(\mathbf{x})} \end{aligned} \tag{4.40}$$

$$\begin{aligned} \frac{\ddot{e}_4(t)}{\sigma_5 f_{2ie}(\mathbf{x})} + \dot{e}_4(t) + \frac{\sigma_4}{\sigma_5} e_4(t) = \frac{f_{5b}(\mathbf{x})}{\sigma_5 f_{5ie}(\mathbf{x})} \\ + \frac{x_6^{\mathrm{d}}}{\sigma_5} - \frac{\ddot{x}_4^{\mathrm{d}}(t)}{\sigma_5 f_{5ie}(\mathbf{x})} + \tilde{p}_4(t) + \frac{\tilde{p}_5(t)}{\sigma_5 f_{5ie}(\mathbf{x})} + \frac{\dot{\tilde{p}}_4(t)}{\sigma_5 f_{5ie}(\mathbf{x})} \end{aligned} \tag{4.41}$$

According to the analysis for the NDO in Section 3.2, if the lumped disturbance and uncertainty variations $\dot{p}_i \approx 0$, the estimations $\hat{p}_i(t)$ converge to real values $p_i(t)$. Hence, the dynamics of e_1 and e_4 do not depend on neither the disturbances nor the uncertainties.

$$\frac{\ddot{e}_1(t)}{\sigma_2 f_{2is}(\mathbf{x})} + \dot{e}_1(t) + \frac{\sigma_1}{\sigma_2} e_1(t) = \frac{f_{2b}(\mathbf{x})}{\sigma_2 f_{2is}(\mathbf{x})} + \frac{x_3^{\mathrm{d}}}{\sigma_2} - \frac{\ddot{x}_1^{\mathrm{d}}(t)}{\sigma_2 f_{2is}(\mathbf{x})} \tag{4.42}$$

$$\frac{\ddot{e}_4(t)}{\sigma_5 f_{5ie}(\mathbf{x})} + \dot{e}_4(t) + \frac{\sigma_4}{\sigma_5} e_4(t) = \frac{f_{5b}(\mathbf{x})}{\sigma_5 f_{5ie}(\mathbf{x})} + \frac{x_6^{\mathrm{d}}}{\sigma_5} - \frac{\ddot{x}_4^{\mathrm{d}}(t)}{\sigma_5 f_{5ie}(\mathbf{x})} \tag{4.43}$$

As the right-hand sides of (4.42) and (4.43) are not 0, to eliminate the tracking errors in steady state, one could think to choose the current references as

$$x_3^{\mathrm{d}} = \frac{\ddot{x}_1^{\mathrm{d}}(t)}{f_{2is}(\mathbf{x})} - \frac{f_{2b}(\mathbf{x})}{f_{2is}(\mathbf{x})},\ x_6^{\mathrm{d}} = \frac{\ddot{x}_4^{\mathrm{d}}(t)}{f_{5ie}(\mathbf{x})} - \frac{f_{5b}(\mathbf{x})}{f_{5ie}(\mathbf{x})} \tag{4.44}$$

However, two restrictive assumptions have been made in this analysis. Firstly, it has been supposed that perfect sliding mode ($\boldsymbol{\sigma} = \mathbf{0}$) is taking place, which is not

true since the boundary layer in (4.37) has been introduced (therefore, $\boldsymbol{\sigma} \approx \mathbf{0}$). In second place, small variations in the lumped disturbance and uncertainty vector have been assumed ($\dot{p}_i \approx 0$). This has not necessarily to be true and, in that case, the estimation errors $\tilde{p}_i$ do not converge to zero, but to the upper-bounds estimation errors obtained in Appendix C.3 and given by $\tilde{p}_i(t) \leq \dot{\mathrm{p}}_{\mathrm{i,max}}/\mathrm{L}_{\mathrm{ii}}$. Therefore, x_3^{d} and x_6^{d} do have to account for those errors, as (4.40) and (4.41) show. For these reasons, adding an additional controller to control x_3^{d} and x_6^{d} is a justified approach to reduce tracking error when the system is under the sliding mode dynamics.

PI control of current references

A PI controller is chosen to control x_3^{d} and x_6^{d}. It shall be remarked that the controller architecture does not use the PI controller to control the currents, but the current references using the articular position errors ($e_{\mathrm{p1}} = -e_1$, $e_{\mathrm{p4}} = -e_4$) as feedback. The maximum and minimum reference values for the currents are matched with the saturation values for the motor currents $\mathrm{i}_{\mathrm{sat}}$. Additionally, a saturation for the integral errors ($e_{\mathrm{i1}} = \int_0^t e_{\mathrm{p1}}\,\mathrm{d}\tau$, $e_{\mathrm{i4}} = \int_0^t e_{\mathrm{p4}}\,\mathrm{d}\tau$) is included and fixed to $0.5\mathrm{i}_{\mathrm{sat}}$. The current control references for shoulder and elbow motors are then respectively given by (4.45) and (4.46).

$$x_3^{\mathrm{d}} = \mathrm{k}_{\mathrm{ps}} e_{\mathrm{p1}} + \mathrm{k}_{\mathrm{is}} e_{\mathrm{i1}} \tag{4.45}$$

$$x_6^{\mathrm{d}} = \mathrm{k}_{\mathrm{pe}} e_{\mathrm{p4}} + \mathrm{k}_{\mathrm{ie}} e_{\mathrm{i4}} \tag{4.46}$$

The possibility of adding an additional SMC for current references was also explored. However, simulation showed that motor currents have such fast dynamics that chattering generation was a difficultly avoidable issue. In the context of the global controller, this PI auxiliary module represents a good trade-off between behavior smoothness and tracking error reduction.

4.2.4 Experimental tests

The experimental results obtained after implementing the CPISDO controller over the ExoFlex v1 are presented in this section. The purpose of the experimentation was to evaluate the performance of the controller, in terms of accuracy for trajectory tracking in passive rehabilitation therapy. To obtain a broader picture of how the new controller performs, a simple PI controller and a super-twisting SMC were also implemented and tested for comparison with the CPSIDO controller. Notwithstanding the PI-family controllers are not frequently implemented over exoskeletons, there are some examples of their use in literature, as the low-level PID implmeneted in [11] or [22], a work in which the authors used a PID as a baseline to evaluate the performance of their fuzzy SMC controller. Moreover, PI controllers have been used for decades to control systems of different nature, specially electromechanical systems, so the author considers that including this controller in the study can be useful to obtain a view of how the CPISDO controller performs in comparison to classical controllers in the trajectory tracking problem. In regard to the super-twisting SMC [146], it is a type of sliding mode controller focused in chattering attenuation. It reduces chattering proposing a control law that diminishes the intrinsic discontinuity of the control action via its integration. This controller was also used in previous

work of the research group [147], and is defined by:

$$\begin{cases} u = \begin{bmatrix} u_1 \\ u_2 \end{bmatrix} = \begin{bmatrix} c_\mathrm{s} \left|\sigma_\mathrm{s}\right|^{\frac{1}{2}} \mathrm{sign}(\sigma_\mathrm{s}) + w_\mathrm{s} \\ c_\mathrm{e} \left|\sigma_\mathrm{e}\right|^{\frac{1}{2}} \mathrm{sign}(\sigma_\mathrm{e}) + w_\mathrm{e} \end{bmatrix} \\ \dot{w} = \begin{bmatrix} \dot{w}_\mathrm{s} \\ \dot{w}_\mathrm{e} \end{bmatrix} = \begin{bmatrix} b_1 \mathrm{sign}\left(\sigma_1\right) \\ b_2 \mathrm{sign}\left(\sigma_2\right) \end{bmatrix} \end{cases} \tag{4.47}$$

$$\begin{cases} c_\mathrm{s} = 1.5\sqrt{C_\mathrm{s}},\ c_\mathrm{e} = 1.5\sqrt{C_\mathrm{e}} \\ b_\mathrm{s} = 1.1C_\mathrm{s},\ b_\mathrm{e} = 1.1C_\mathrm{e} \\ \sigma = \begin{bmatrix} \sigma_\mathrm{s} \\ \sigma_\mathrm{e} \end{bmatrix} = \begin{bmatrix} \sigma_1 e_1 + \sigma_2 e_2 + e_3 \\ \sigma_3 e_4 + \sigma_4 e_5 + e_6 \end{bmatrix} \end{cases} \tag{4.48}$$

where C_s and C_e are control parameters and σ_s and σ_e the sliding surfaces.

The experiments were conducted over ten healthy participants (seven males and three females), with an average height of 1.77 ± 0.08 m (mean ± standard deviation), an average weight of 68.46 ± 10.21 kg and an average age of 26.4 ± 4.43 years. All experimental procedures were carried out in accordance with the Declaration of Helsinki on research involving human subjects and approved by the ethical committee of the Universidad Politécnica de Madrid.

Experiment description

Two experiments were performed for each one of the three controllers. The first one was a trajectory tracking without adding external disturbances (called in the experiment as free movement) and, in the second one, an external disturbance was applied as explained further on. The second experiment was important to evaluate how the controller rejects disturbances.

Preparation of the subjects The exoskeleton and the proposed controller are intended for passive rehabilitation. Therefore, the conditions under which the tests were performed aimed to be as similar as possible to what a real rehabilitation therapy could be. All the participants were instructed to leave their arms completely relaxed during the experiments. Ensuring that the subjects leave their arms inert and do not favor the movement of the exoskeleton is crucial to make the evaluation of the controllers as rigorously as possible, obtaining unbiased results.

At the beginning of each of the experiments the participants were told to sit on the chair incorporated in the fixed frame. Then, they donned the wearable part of the exoskeleton, adjusting the Velcro straps to the user's arm. Afterwards, the two IMU sensors were attached to the upper-arm and forearm with additional elastic Velcro fastenings. Adjustments in the fastenings tightness were made according to the users' feedback, guaranteeing comfort and a good fixation of the exoskeleton.

Two emergency buttons were available during the experimental tests. One of them was given to the subject and the other one was held by one of the researchers conducting the study. The users were allowed to press the button whenever they considered necessary: if they felt some kind of pain, were frightened or any other reason. By pressing these buttons, power supply was removed from the motors, stopping immediately the movement.

Trajectory generation The trajectory performed in each of the experiments can be divided in three movements. En each of the movements, both articulations started in the relaxed position. In movement one, an elbow flexion to 75° and a posterior extension to the initial position were performed. In this movement, the shoulder remained in the relax position. Movement 2 consisted of a shoulder flexion to 75° (with the elbow fully extended) and a posterior extension to the initial position. Finally, in movement three, flexion of both elbow and shoulder to 75° were simultaneously performed. The range of 75° was chosen for all the participants since the articular ROM for patients is usually very restricted a rehabilitation early stages. In each of the three movements, the angular references were maintained for a certain time between each flexion and extension. The trajectory was designed to have a fixed duration of 134 seconds, divided in 34 seconds for movement one, 42 seconds for movement 2 and 58 seconds for movement 3. In each of the movements, the flexion segment began at the start of each interval and the extension one began at the half. Both flexion and extension trajectories were designed as trapezoidal speed profiles. The acceleration for all the profiles of both articulations was set to 2.86 deg/s^2. The absolute values of the maximum speeds of the flexion and extension segments of each movement were set to $\omega_1 = 5.67$ deg/s, $\omega_2 = 4.58$ deg/s and $\omega_3 = 2.29$ deg/s. Every subject has their own relaxed position, being then the

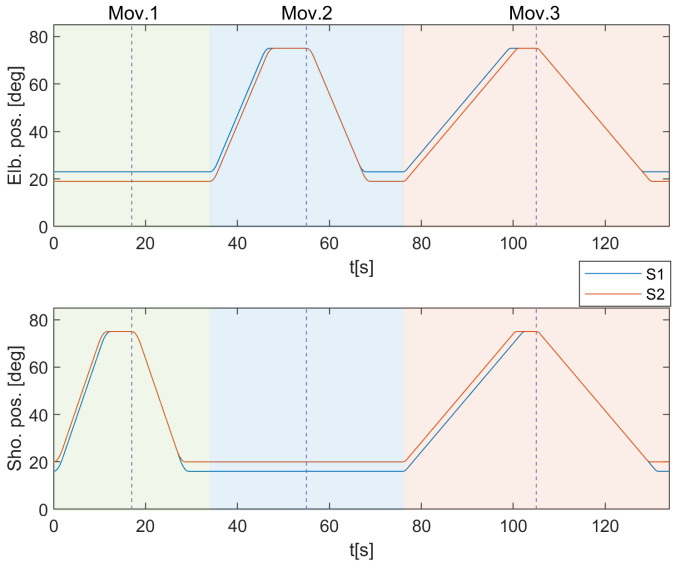


Figure 4.5: Trajectory reference for elbow and shoulder for two subjects. References slightly vary according to subject's rest position. Each shaded area corresponds to each of the three movements and dashed lines separate flexion and extension segments within the same movement.

initial angles for the trajectories different among subjects. These initial angles for both elbow and shoulder can even slightly vary for a single subject between different trajectories depending, for example, on the way they were sat on the chair or how the exoskeleton was donned. The average initial position among subjects for the shoulder was 22.83 ± 1.83° (mean ± standard deviation) and for the elbow it was 18.67 ± 2.66°. The previous description of the trajectory and the effect that different rest positions have in the trajectory creation can be observed in Fig. 4.5.

Experiments with disturbances The disturbances that were applied to the system were step-like disturbances, which are the most aggressive disturbances that can be introduced to a system. This was done by giving a ballast bag to the users at some point of the flexion motions and asking them to drop it at some point of the extension segments. When the users grabbed the bag, they were told to only open and close their hands so that their arm still remained limp. Likewise, they were told just to open their hand in order to release the weight. The ballast used in these experiments had a weight of 0.75 kg (Fig. 4.6), which represents a wide range of objects that are caught during activities of daily life, like a lunch box, handbag or a bottle of water [26]. Application of slower-evolving disturbances are more relaxed scenarios than the one studied in this experiment.



Figure 4.6: Subject performing an experiment with disturbances.

Parameter's tuning The available time to prepare subjects before starting the rehabilitation therapy is very reduced. The longer it takes to prepare the subject, the shorter will be the remaining time for therapy. For this reason, to eventually use the exoskeleton in a real rehabilitation environment, it is desirable that the controller does not need to be tuned. According to these requirements, control parameters were only tuned for an average subject once before starting the experiments. This was done for the CPISDO, super-twisting and PI controllers. The control action of the CPISDO also depends on the anatomical parameters of the subject, according to (4.35) and (4.36). For this controller, the average anatomical parameters for all the subjects gathered in Table. 4.2 were used.

Table 4.2: Average arm model parameters.

Upper arm			**Forearm + hand**		
m [kg]	l [m]	I [kgm^2]	m [kg]	l [m]	I [kgm^2]
2.423	0.305	0.0751	2.260	0.313	0.0738

If the same values are assigned to CPISDO control parameters for each subject, the lumped uncertainty will increase for some of them (the more as more different are the assigned parameters to the real ones) but this should be overcome by the controller's robustness, as shown in Section 4.2.3 and the analyses in Appendix C.3 and Appendix C.4. Regarding the other two controllers, the PI should be the most affected one by not specifically tuning control parameters for each subject and the super-twisting should be affected to some extent because it is robust to matched uncertainties but not to unmatched ones.

Control parameters were first estimated via Matlab simulations. For the CPSIDO controller, the values of the switching gains k_s and k_e were incremented until the tracking error was very reduced. Afterwards, the widths of the boundary layers ϕ_s and ϕ_e were gradually incremented to reduce chattering. The larger the widths of the boundary layers are, the lower the chattering is, but the greater the tracking error is. In order to obtain a good trade-off between chattering and tracking error, some iterative adjustments were performed. The NDO gain matrix $\mathbf{L}$ was tuned to get reasonably fast but damped disturbance estimations. Similarly to what was done with the CPISDO, the parameters of the super-twisting controller were also tuned to obtain low tracking error with low chattering. The sliding manifold was the same for the two sliding mode controllers, selected to provide a damped response. Finally, the parameters for the PI controller were adjusted to obtain a fast response, allowing a maximum overshoot of 5%.

After simulation tuning, the three controllers were tested over subject S10, who had a weight and height near to the average of the ten participants. Most of the parameters were left as in simulation, but some adjustments had to be done to some of them. For both sliding mode controllers (the CPISDO and the super-twisting controller) the observed chattering was greater than expected. For this reason, switching gains k_s and k_e for the CPSIDO and parameters C_s and C_e for the super-twisting controller were slightly reduced. At the same time, the widths of the boundary layers ϕ_i were marginally increased. In regard to the PI parameters, the results obtained in the preliminary tests with subject S10 were similar to the simulation ones, so no changes in any parameters were performed. Values assigned to all control parameters are gathered in Table 4.3.

Table 4.3: Control parameters used in experimental tests.

CPISDO	**Super-twisting**	**PI**
$[k_s, k_e] = [28000, 28000]$	$[C_s, C_e] = [10, 5]$	$k_{ps} = 120$
$[\sigma_1, \sigma_2] = [50, 10]$	$[\sigma_1, \sigma_2] = [50, 10]$	$k_{pe} = 100$
$[\sigma_4, \sigma_5] = [50, 10]$	$[\sigma_4, \sigma_5] = [50, 10]$	$k_{is} = 70$
$[\phi_s, \phi_e] = [2, 3]$		$k_{ie} = 55$
$[L_{11}, L_{22}] = [2, 2]$		
$[L_{33}, L_{44}] = [0.01, 5]$		
$[L_{55}, L_{66}] = [5, 0.01]$		
$[k_{ps}, k_{is}] = [10, 0.1]$		
$i_{sat} = 0.4$		
$[k_{pe}, k_{ie}] = [10, 0.1]$		

Table 4.4: Average RMSE for each joint and movement

Controller	Dist.	RMSE [deg]								σ [deg]	
		Mov. 1		Mov. 2		Mov. 3		Total		Total	
		Elb	Sho	Elb	Sho	Elb	Sho	Elb	Sho	Elb	Sho
CPISDO	No	0.56	0.14	0.85	0.37	0.86	0.31	0.79	0.31	0.10	0.11
	Yes	1.30	0.67	1.11	0.97	1.14	0.47	1.12	0.75	0.32	0.57
Super-twisting	No	0.63	0.23	0.92	0.96	1.50	0.63	1.16	0.70	0.42	0.11
	Yes	1.72	1.01	2.41	1.40	1.81	1.08	2.12	1.26	1.26	0.73
PI	No	2.06	0.45	2.10	2.28	2.20	1.67	2.14	1.71	0.50	0.39
	Yes	2.56	0.82	2.70	2.26	2.23	1.45	2.68	1.86	0.82	0.39

Experimental results

In this section, the experimental results of the conducted study are analyzed. Tracking RMSEs were obtained for all the experiments performed over each subject. Table 4.4 presents the average RMSEs among the ten subjects for each controller and articulation. The RMSEs are segmented for each of the three movements. The standard deviation of the total RMSE among subjects is also presented. Figure 4.7 graphically shows the results in Table 4.4 with a bar diagram.

The total average RMSEs obtained with the three controllers for both articulations are low, obtaining a maximum RMSE of 2.68° for the elbow using the PI

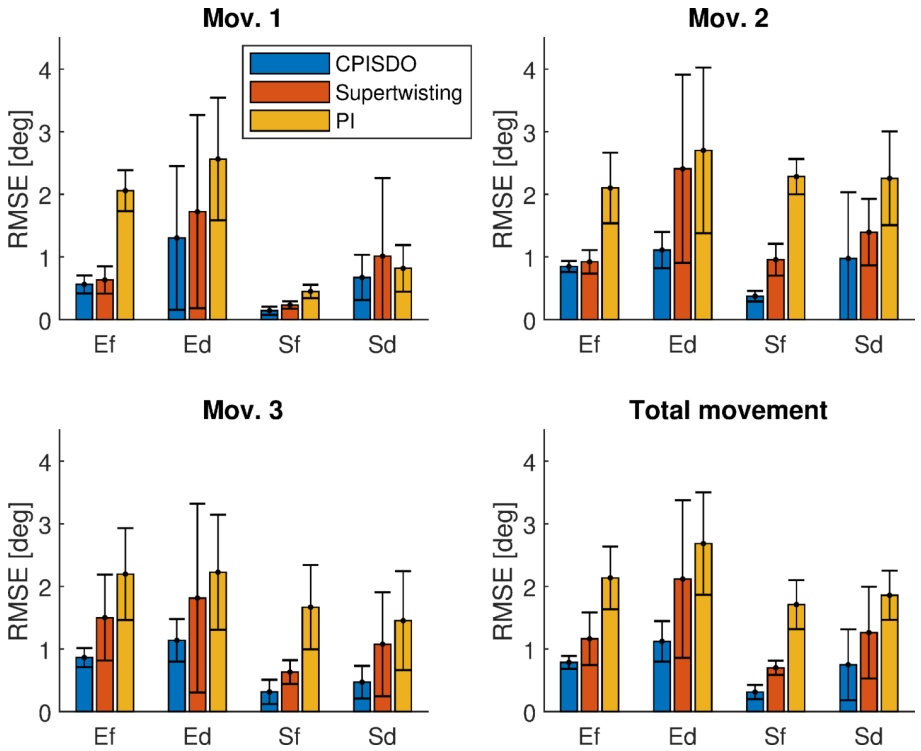


Figure 4.7: Bar diagram of the mean RMSEs for each movement. Error bars represent the standard deviation among subjects. E stands for elbow, S for shoulder and f and d subscripts stand for free and disturbed movements, respectively. Source: Author's publication ©David Pont Esteban et al. 2022; published by IEEE (http://doi.org/10.1109/ACCE SS.2022.3217528).

controller. This shows that the parameters of the three controllers were properly tuned. The CPISDO controller offers the lowest total average RMSE for elbow (0.79° in non-disturbed movement and 1.12° in disturbed one) and shoulder (0.31° in undisturbed movement and 0.75° in disturbed one). Although the RMSEs are low for all the controllers, the relative increments of total RMSEs for super-twisting and PI controllers with respect to CPISDO are significant, and vary from 47% to 126% for the super-twisting controller and from 139% to 452% for the PI. As Table 4.4 shows, the RMSE standard deviation for the CPISDO controller is the lowest in three of the four combinations of articulation and disturbance application. The super-twisting controller delivers a good performance in terms of RMSE, offering intermediate results between the CPISDO and the PI. Nevertheless, the standard deviations for RMSES under the application of disturbances are the highest in both articulations for all the disturbed experiments. This suggests that, although disturbances are reasonably effectively rejected, the grade of rejection depends on the user's characteristics. Regarding the PI controller, the total average RMSEs are the highest, as it was expected to its simplicity. However, the standard deviations are reasonably bounded, what implies that the behavior of the controller over different subjects is relatively similar.

If the RMSEs are segmented by type of movement, interesting results can be observed. The lowest RMSEs for the shoulder in the six types of experiments are obtained in movement one. This is as expected, since this movement consists of elbow flexion and extension, leaving the upper-arm in a constant relaxed position. Similarly, one could expect that the lowest RMSEs for the elbow are obtained for movement two, where shoulder flexion and extension movements are performed leaving the elbow relaxed. However, the lowest elbow average RMSEs for undisturbed movements are also obtained in movement one. What prevents to obtain lower RMSEs in movement two is that the elbow relax position when the shoulder is also relaxed is different to the one obtained when the angle of the shoulder varies. Initial elbow positions were around 18°, but as the shoulder flexes and the forearm is left inert, gravity pushes down the forearm, varying that initial position and the controller has to compensate for it. The average RMSEs for each movement in disturbed and undisturbed experiments are lower for the shoulder than for the elbow (with the exception of undisturbed movements for movement 2 using the PI). This is due to the fact that the elbow is located farther in the kinematic chain, therefore, shoulder movements affect the elbow in a higher grade than elbow ones do over the shoulder. Not only the average total RMSEs are the lowest for the CPISDO for both joints and in presence and absence of disturbances, but also this controller presents the average lowest RMSEs for each movement segment.

The individualized tracking RMSEs for each subject, articulation and controller are presented in Table 4.5 and Table 4.6, and are graphically represented in Fig. 4.8. The RMSEs using the CPISDO controller for all the subjects are very homogeneous, with the exception to the shoulder RMSE for S1 when applying disturbances. Probably, this is due to an issue when grabbing the load during the experiment in one of the segments. For undisturbed movements, CPISDO RMSEs for the ten subjects almost form a regular decagon in Fig. 4.8. This figure gives a clear insight of the contrast between the homogeneity of performance over different subjects offered by CPISDO and the one provided by the super-twisting and PI controllers. In regard to the PI controller, it can perform pretty well for some subjects, as S5, but much

Table 4.5: Shoulder RMSE for each subject and experiment.

Controller	Dist.	Shoulder RMSE [deg]									
		S1	**S2**	**S3**	**S4**	**S5**	**S6**	**S7**	**S8**	**S9**	**S10**
CPISDO	No	0.29	0.28	0.59	0.33	0.28	0.41	0.27	0.25	0.19	0.24
	Yes	2.28	0.60	0.42	0.95	0.57	0.43	0.45	0.51	0.47	0.80
Super-twisting	No	0.65	0.68	0.84	0.74	0.78	0.66	0.72	0.51	0.87	0.56
	Yes	2.58	2.44	1.00	1.17	1.60	0.94	0.32	0.68	0.93	0.96
PI	No	1.51	1.90	1.63	1.35	1.82	2.55	1.39	2.07	1.62	1.25
	Yes	2.07	1.70	1.70	1.72	1.59	2.64	2.32	1.90	1.28	1.68

Table 4.6: Elbow RMSE for each subject and experiment.

Controller	Dist.	Elbow RMSE [deg]									
		S1	**S2**	**S3**	**S4**	**S5**	**S6**	**S7**	**S8**	**S9**	**S10**
CPISDO	No	0.80	0.69	0.77	0.80	0.71	0.96	0.85	0.89	0.60	0.80
	Yes	1.32	0.82	0.93	1.67	0.89	1.12	0.91	1.00	0.90	1.67
Super-twisting	No	0.85	0.72	1.08	1.61	0.94	1.43	0.91	1.04	2.08	0.99
	Yes	3.38	3.12	1.10	1.08	1.38	4.62	0.97	1.29	1.51	2.73
PI	No	1.88	1.84	1.88	1.93	1.97	3.19	2.23	2.9	1.69	1.85
	Yes	2.60	1.81	2.73	2.63	1.82	4.34	2.92	2.56	1.80	3.63

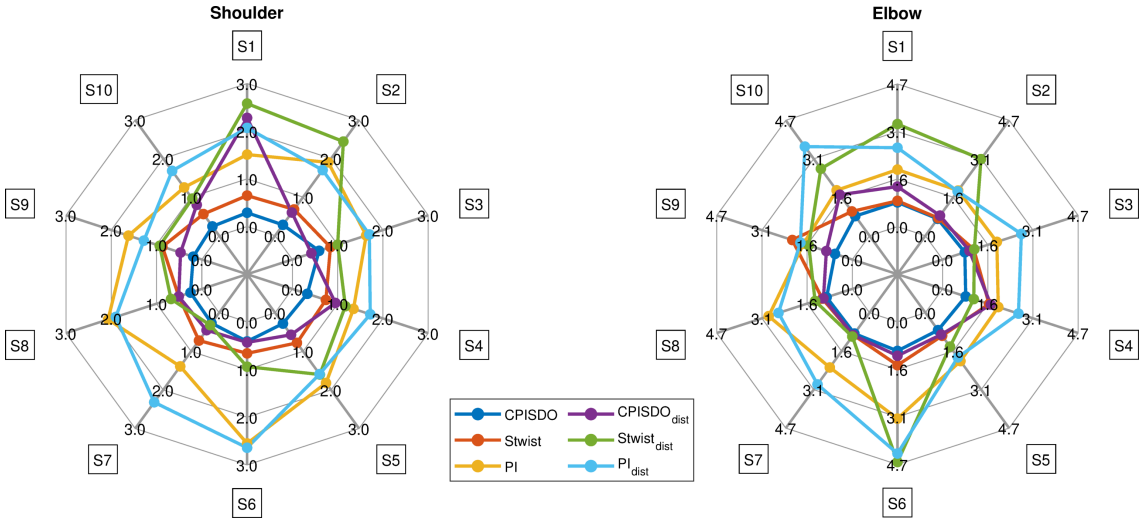


Figure 4.8: Tracking RMSE for each articulation, controller and subject for both disturbed and undisturbed movements. RMSE units are degrees. Source: Author's publication ©David Pont Esteban et al. 2022; published by IEEE (http://doi.org/10.1109/ACCESS.2022.3217528).

worse for others, as S6. Similar behavior can be observed for the super-twisting controller. It is remarkable the fact that the RMSEs obtained with CPISDO for disturbed movements in both articulations are still lower than the ones obtained in undisturbed movement with the PI controller and even with the super-twisting one for most of the subjects.

Figure 4.9 represents a data collection of each of the six different experiments for a different subject. The goal of showing graphical results of different subjects us-

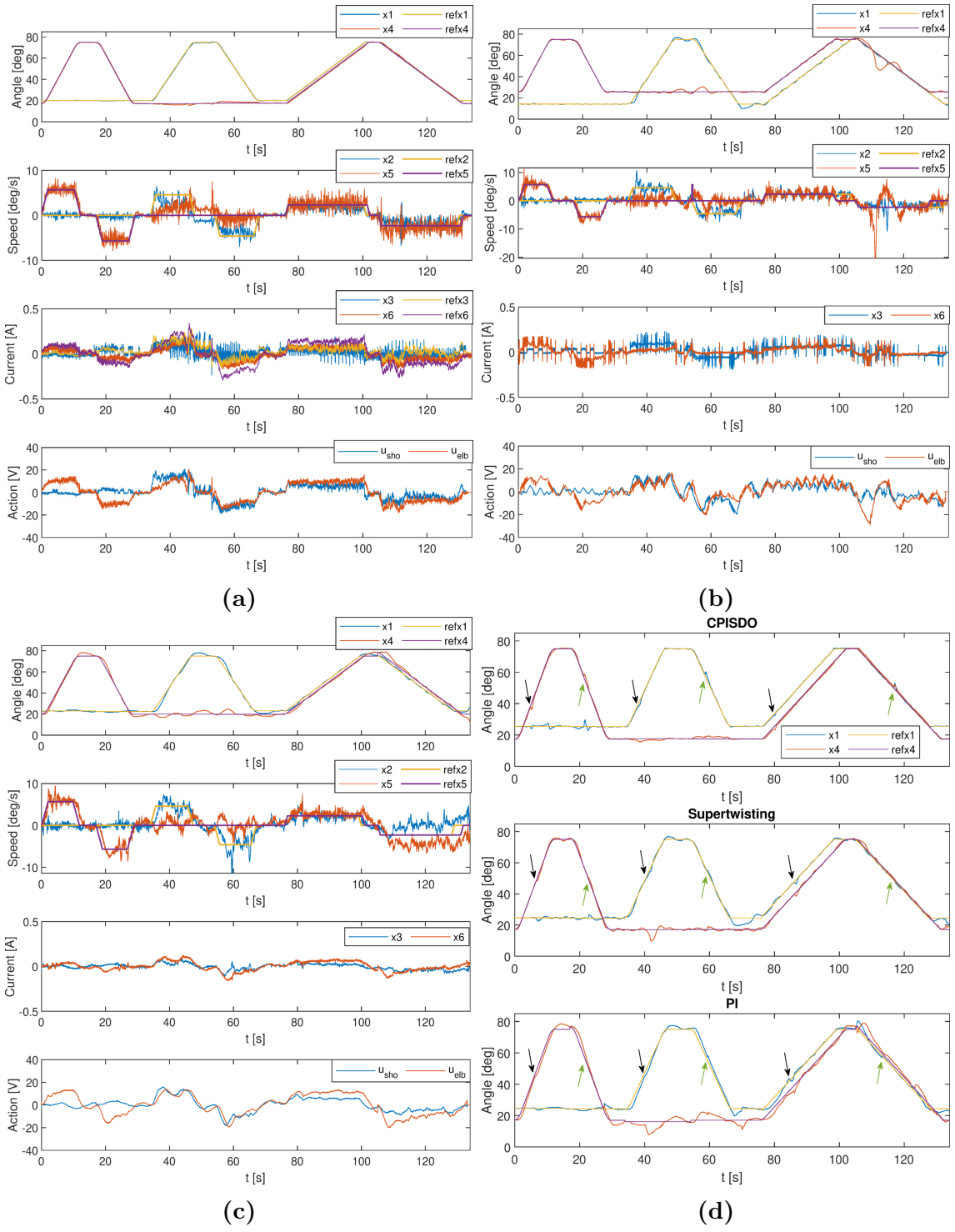


Figure 4.9: Data obtained during the experiments. The first three figures show the positions, speeds, currents and control actions in undisturbed movements for: (a) CPISDO over subject S2, (b) Super-twisting SMC over subject S9 and (c) PI over subject S10. (d) Position plots for the three controllers in disturbed movements. Downward arrows indicate the disturbance application and upward ones point the disturbance removal. From up to down, the plots correspond to S5, S4 and S7. Source: Author's publication ©David Pont Esteban et al. 2022; published by IEEE (http://doi.org/10.1109/ACCESS.2022.3217528).

Table 4.7: Average overshoot for each controller, joint and movement, for undisturbed movements.

Controller	Joint	Average overshoot [%]			
		Mov. 1	Mov. 2	Mov. 3	Avg.
CPISDO	**Elb.**	0.23	—	0.33	0.28
	Sho.	—	0.12	0.20	0.16
Super-twisting	**Elb.**	1.65	—	2.24	1.94
	Sho.	—	2.37	1.47	1.92
PI	**Elb.**	4.55	—	4.96	4.73
	Sho.	—	4.46	3.14	3.80

ing different controllers is to provide more evidence about the tests were conducted over different subjects. On the one hand, for undisturbed movements, position, speed current and control action signals are plotted. On the other hand, only position signals are shown for disturbed ones. Differently to the position responses observed for the super-twisting and PI controllers, the CPISDO controller does not present oscillations in the response. Oscillations in angular position and speed for super-twisting and PI controllers are noticeable not only in the plots, but also the participants informed during the experiments that they could feel those oscillations. The oscillatory behavior is more appreciable in the elbow joint, specifically in movement two. Specially, PI controller struggles to hold the elbow position while shoulder is being flexed and extended.

The average overshoot of the three controllers for undisturbed movements was studied. The percentages of overshoot for each articulation, controller and movement are presented in Table 4.7. The CPISDO controller presents insignificant overshoot percentages, which are below 0.4% in all cases which, given the reference of 75° it is less than 0.3°. The PI controller is the one with largest overshoot, obtaining absolute values of around 3.6° for the elbow and 2.9° for the shoulder. The overshoot obtained with the super-twisting controller is intermediate between the other two controllers.

The estimation of the lumped uncertainties and disturbances for subject S6 using the CPISDO controller in new trials of free and disturbed movements are presented in Fig. 4.10. For the undisturbed movement, the estimations are far from being zero, specially the acceleration disturbances. These estimations gathered all the parameter uncertainties and the model simplifications that were done in the modelling stage. Moreover, when disturbances are applied to the system, the estimations are quite similar to the undisturbed experiment. This implies that unmodelled dynamics and uncertainties have more weight than the externally added disturbances. Nevertheless, the CPISDO is able to provide high-accuracy trajectory tracking, as proven by Tables 4.4, 4.5 and 4.6, what means that the NDO module is able to properly estimate the lumped disturbances and uncertainties and compensate for them.

As observed in the current plot for the CPISDO controller (Fig. 4.9a), a remarkable error exists between the current references and the actual currents. This is more noticeable for the elbow joint (x_6 and ref_{x6}). The observed behavior is completely expected. The PI auxiliary controller was not introduced to control the motors' currents, but their references. In this way, the position error generated by the intro-

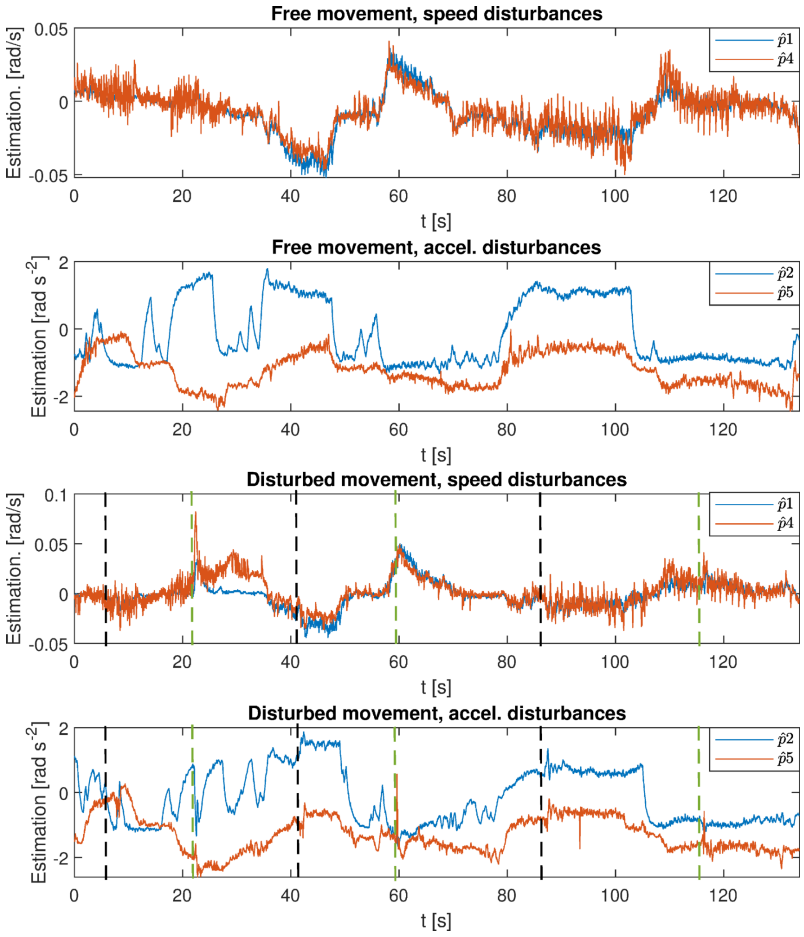


Figure 4.10: Estimations of lumped disturbances and uncertainties over shoulder and elbow in free and disturbed movements, with and without disturbance application. Black dashed lines indicate when the disturbance is applied. Green ones mark the instant in which the disturbance is removed. Source: Author's publication ©David Pont Esteban et al. 2022; published by IEEE (http://doi.org/10.1109/ACCESS.2022.321 7528).

duction of the limit layer is absorbed by generating the appropriate current errors e_3 and e_6. This allows the right-hand sides of (4.40) and (4.41) to be closer to 0, therefore reducing position errors beyond the limitation introduced by the boundary layers.

Evaluating the influence that the inclusion of the PI controller has over the tracking error is necessary. For this purpose, simulations of the CPISDO with and without the PI module were executed. In the simulation in which the PI was removed, references for the motor currents were given according to the model-based method given by (4.44). In both simulations, an error of 15% was added to all the mass and geometrical parameters in relation to the nominal system ones that are gathered in Table C.1. These errors were added to consider user variability and model uncertainty in the simulations. The control parameters and the trajectory profiles used in the simulation were the same ones that were used in the experimental tests with subjects. The RMSEs obtained including the PI to set the current references were 0.115° for the elbow and 0.022° for the shoulder. Without the PI, the elbow error was 3 times larger, ascending to 0.375° and 13 times larger for the

shoulder, reaching 0.290°. It is important to note that, even a difference between nominal and control parameters was added in simulation, all the unmodelled and unknown dynamics of the system were obviously not included. This is the reason why the RMSEs obtained in simulation were lower than experimental ones.

The last issue to be treated is the chattering. The PI control signal is obviously chattering-free, but although the amplitude and frequency are low, a small chattering exists for both the CPISDO and super-twisting controllers. On the one hand, the super-twisting design by itself is focused on highly attenuating the chattering. On the other hand, the boundary layer added to the CPISDO successfully attenuates the chattering. No noise associated to the low-amplitude chattering nor motor heating were observed during experiments. The control actions were perfectly assumable by the actuators.

The tracking RMSEs obtained with the CPSISDO controller and ExoFlex are lower than other state of the art solutions, with the handicap for control accuracy that using a soft exoskeleton supposes in comparison to controlling a rigid one. The results obtained in other relevant works using exoskeletons for position control are summarized in Table 4.8 for comparison.

Table 4.8: RMSE comparison of different control methods.

Controller	**Sho. RMSE**	**Elb. RMSE**
AITSMC [27]	0.600°	1.065°
PD-based fuzzy SMC [26]	0.584°	0.602°
SMC with backlash compensation [8]	1.440°	-
CPISDO	0.310°	0.790°

4.3 Geometrical method for motion control

This method was designed to perform shoulder passive rehabilitation for ExoFlex v2. The target motion consists of arm elevation movements in different planes. The elevation plane (the plane in which motion takes place) is determined by the angle between the arm and the sagittal plane along the transverse plane, named in this work as shoulder aperture angle and noted as θ. The arm elevation angle is noted as φ. As mentioned in Section 4.1, no on-body sensors are employed in this method. Instead, shoulder pose is estimated by a geometrical model of the system.

Being known the trajectory in the space desired for the projection over the arm of the anchor point between the exoskeleton and the textile (point A), this method intends to generate the proper trajectory for the end effector of the exoskeleton (point Y) such that, controlling the cable length in each control period $l_{\mathrm{c}}\,[\mathrm{k}]$ the trajectory of the point A corresponds with the desired one. A diagram of a concrete position for shoulder motion is shown in Fig. 4.11. Arm elevation and aperture angles φ and θ are represented. A segment between the acromion (point H) and A of length d_{AH} is defined. The arm will be considered by the algorithm as this simple segment. The distance between A and Y is l, the sum of the cable length l_{c} and the length of the textile l_{t}. The system absolute reference is placed at the connection of the spindle attached to motor M6, with the X axis pointing at the front, the Y axis parallel to the direction of motion generated by M6 and the Z axis in the

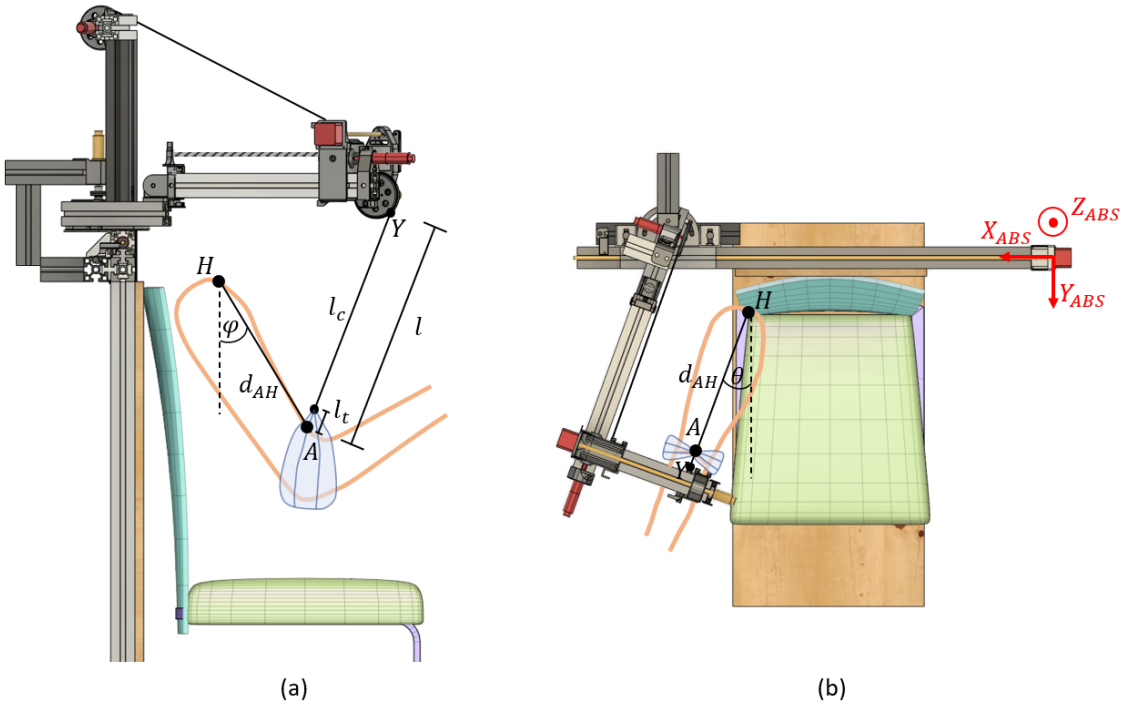


Figure 4.11: Diagram of a position for shoulder passive rehabilitation with ExoFlex v2. Main geometrical variables are represented. (a) Lateral view. (b) Top view.

vertical pointing from down to up. The proposed geometrical method computes the motor positions which place A at its reference, therefore controlling shoulder pose. As individual references for the motors are computed by the algorithm, individual controllers are applied for each of the actuators.

4.3.1 Forward kinematics

A definition of an appropriate set of reference frames is necessary to address the geometrical analysis for generating shoulder motion. A new reference frame is defined for each degree of freedom involved in the rigid frame movement. The reference frames involved in the forward kinematics of the rigid structure are presented in Fig. 4.12. The geometrical configuration of the structure has been varied with respect to Fig. 4.11 for visual purposes. The homogeneous transformation matrices between consecutive reference frames can have rotational components or displacement components. The displacements between references are due to physical magnitudes of the robot or to the displacements generated by the actuators. The parameters involved in each rotation matrix are grouped in Table 4.9. The subscript of each degree of freedom corresponds to the subscript of the corresponding actuator which generates that motion.

All the homogeneous transformation matrices involved in the forward kinematics of the robot are presented in Appendix D.2. Here, ${}^{\text{ABS}}\boldsymbol{T}_3$ and ${}^{\text{ABS}}\boldsymbol{T}_6$ are presented since they are necessary for posterior analysis:

$$ {}^{\text{ABS}}\boldsymbol{T}_3 = \begin{bmatrix} C_3 & S_3 & 0 & Y_{\text{x3}} \\ -S_3 & C_3 & 0 & Y_{\text{y3}} \\ 0 & 0 & 1 & Y_{\text{z3}} \\ 0 & 0 & 0 & 1 \end{bmatrix} \tag{4.49} $$

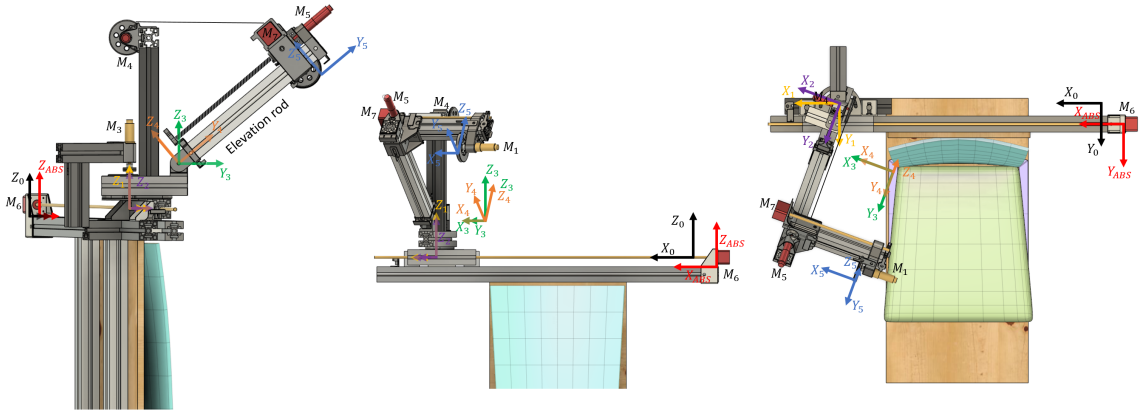


Figure 4.12: Reference frames involved in the forward kinematics of the rigid structure. Each of the axes are represented and labeled in the most representative views. Actuators are also labeled. (a) Side view. (b) Frontal view. (c) Top view.

Table 4.9: ExoFlex v2 kinematic parameters.

Transformation	Fixed parameters	Degree of freedom
${}^{\text{ABS}}\boldsymbol{T}_0$	k_{AOX}, k_{AOY}	-
${}^{0}\boldsymbol{T}_1$	-	d_6
${}^{1}\boldsymbol{T}_2$	-	θ_3
${}^{2}\boldsymbol{T}_3$	$\text{k}_{23\text{X}}$, $\text{k}_{23\text{Y}}$, $\text{k}_{23\text{Z}}$	d_7
${}^{3}\boldsymbol{T}_4$	-	θ_4
${}^{4}\boldsymbol{T}_5$	$\text{k}_{45\text{Y}}$, $\text{k}_{45\text{Z}}$	d_5

$$
{}^{\text{ABS}}\boldsymbol{T}_6 = \begin{bmatrix} C_3 & S_3C_4 & -S_3S_4 & S_3S_4\,|\text{k}_{45\text{z}}| + S_3C_4\,|D_5| + Y_{\text{x3}} \\ -S_3 & C_3C_4 & -C_3S_4 & C_3S_4\,|\text{k}_{45\text{z}}| + C_3C_4\,|D_5| + Y_{\text{y3}} \\ 0 & S_4 & C_4 & S_4\,|D_5| - C_4\,|\text{k}_{45\text{z}}| + Y_{\text{z3}} \\ 0 & 0 & 0 & 1 \end{bmatrix} \tag{4.50}
$$

with $C_{\text{x}} = \cos(x)$, $S_{\text{x}} = \sin(x)$, $Y_{\text{x3}} = -C_3\,|D_7| + S_3\,|\text{k}_{23\text{Y}}| + D_6$, $Y_{\text{y3}} = S_3\,|D_7| + C_3\,|\text{k}_{23\text{Y}}| + \text{k}_{\text{AOY}}$, $Y_{\text{z3}} = |\text{k}_{23\text{Z}}|$, $D_5 = d_5 + \text{k}_{45\text{Y}}$, $D_6 = d_6 + \text{k}_{\text{AOX}}$ and $D_7 = d_7 + \text{k}_{23\text{X}}$.

Values of geometric parameters and position and speed limits for the motors are gathered in Appendix D.1.

4.3.2 Algorithm design

Algorithm 1 was designed to generate the references for the actuators. Given the reference of both elevation and aperture angles for the arm in a certain control period ($\varphi\,[\text{k}]$ and $\theta\,[\text{k}]$, respectively), the coordinates of H with respect to the absolute reference frame, the distance d_{AH} and l_{t}; Y and l are computed. Once the end effector pose and total length (cable plus textile) are obtained for a control period ($Y\,[\text{k}]$, $l\,[\text{k}]$), references for the actuators are computed (θ_1^{d}, θ_3^{d}, θ_4^{d}, d_5^{d}, d_6^{d} and d_7^{d}). Recall that motor M2 is responsible of elbow flexion, which is not involved in the present method. For a certain pair of shoulder reference angles φ, θ, different combinations of $Y\,[\text{k}]$ and $l\,[\text{k}]$ can achieve the desired pose for the shoulder. The proposed algorithm positions the end effector of the actuator such that the cable belongs to the

Algorithm 1: Procedure to compute actuator references to obtain an arbitrary shoulder pose.

Data: Shoulder reference angles: $\varphi\,[\mathrm{k}]$, $\theta\,[\mathrm{k}]$
Data: User dependent parameters: $H|_{\mathrm{ABS}}$, d_{AH}, l_{t}, d
Result: Actuator references: $\theta_1^{\mathrm{d}}\,[\mathrm{k}]$, $\theta_3^{\mathrm{d}}\,[\mathrm{k}]$, $\theta_4^{\mathrm{d}}\,[\mathrm{k}]$, $d_5^{\mathrm{d}}\,[\mathrm{k}]$, $d_6^{\mathrm{d}}\,[\mathrm{k}]$, $d_7^{\mathrm{d}}\,[\mathrm{k}]$

0. Computation of M3, M6 and M7 references for motion generation.
1. Obtention of $A|_{\mathrm{ABS}}$ from φ, θ, $H|_{\mathrm{ABS}}$ and d_{AH}.
2. Obtention of the elevation plane equation P_2.
3. Obtention of $Y\,[\mathrm{k}]$, with $\boldsymbol{AY}$ perpendicular to $\boldsymbol{AH}$.
   3.1 Obtention of straight s, perpendicular to vector $\boldsymbol{AH}$, belonging to P_2 and which contains point A.
   3.2. Compute length $l\,[\mathrm{k}]$, arbitrarily imposed for control period k.
   3.3. Find point belonging to s which is at distance $l\,[\mathrm{k}]$ of point A.
4. Check reachability of $Y\,[\mathrm{k}]$:
   4.1. Computation of rigid frame actuators' references using inverse kinematics.
   4.2. Check if actuators' references are physically reachable.
   if *any actuator is saturated* **then**
      I. Compute $Y_{\mathrm{sat}}\,[\mathrm{k}]$ using forward kinematics.
      II. Compute $l\,[\mathrm{k}]$ through $Y_{\mathrm{sat}}\,[\mathrm{k}]$:
         a) Projection of $Y_{\mathrm{sat}}\,[\mathrm{k}]$ and H onto the motion plane (O_3 axes).
         b) Solve the HAY_{sat} triangle in the motion plane.
         c) Saturate the obtained $l\,[\mathrm{k}]$.
5. Compute $\theta_1^{\mathrm{d}}\,[\mathrm{k}]$ through $l\,[\mathrm{k}]$.

motion plane (named P_2). This is achieved through properly computing the reference positions for actuators M3, M6 and M7 (step 0 of Algorithm 1). Under those conditions, the algorithm intends to position the cable perpendicularly to the subject's arm, whenever this is possible. By imposing the perpendicularity condition, there is only one possible solution for the pair $Y\,[\mathrm{k}]$, $l\,[\mathrm{k}]$. The perpendicularity optimizes the necessary torque to mobilize the subjects arm and also increases comfort in comparison to other approaches in which the cable is not perpendicular to the arm. However, it is not always possible to achieve a perpendicular configuration. This is due to workspace limitations for the robot and also to speed limitations of the actuators (a configuration $Y\,[\mathrm{k}]$, $l\,[\mathrm{k}]$ might be achievable, but not within the time given for a control period). For this reason, the algorithm checks if the pair $Y\,[\mathrm{k}]$, $l\,[\mathrm{k}]$ is reachable. In case it is not, the saturated end effector position $Y_{\mathrm{sat}}\,[\mathrm{k}]$ is computed using the robot's forward kinematics and the new necessary cable length that positions point A where desired is computed. Finally, the reference for M1 that generates $l\,[\mathrm{k}]$ is computed.

It it important to remark that the positions of M3, M6 and M7 do not vary during an arm elevation exercise, since the elevation plane is not modified and it only depends on the positions of those three motors. For this reason, step 0 of Algorithm 1 just needs to be executed once prior to the trajectory generation, not in each control period. The geometrical positioning method is described in the following subsections. Steps 1 and 2 of Algorithm 1 are presented first as the mathematical developments of those two steps are also used in step 0.

Obtention of point $A|_{\mathbf{ABS}}$

It can be considered that point H remains in a fixed position during all elevation movements. The distance d_{AH} is also constant. Given the aperture and elevation angles, the coordinates of A are easily computed:

$$A|_{\mathrm{ABS}} = \begin{bmatrix} H_{\mathrm{x}} + d_{\mathrm{AH}} \sin(\varphi) \sin(\theta) \\ H_{\mathrm{y}} + d_{\mathrm{AH}} \sin(\varphi) \cos(\theta) \\ H_{\mathrm{z}} - d_{\mathrm{AH}} \cos(\varphi) \end{bmatrix} \tag{4.51}$$

Obtention of the elevation plane

The elevation plane (P_2) meets two conditions:

1. It contains the straight r determined by the points A and H.
2. It is perpendicular to the ground plane since the motion to be performed by the arm is elevation in a single plane.

The ground plane (P_1) is determined by its normal vector $\boldsymbol{n}_1 = (0, 0, 1)$. As the planes P_1 and P_2 are perpendicular, the equation of any plane parallel to ground can be used. For simplicity, $P_1 : \ z = 0$ is set. The straight r which contains A and H is given by:

$$r : \ \frac{x - A_{\mathrm{x}}}{v_1} = \frac{y - A_{\mathrm{y}}}{v_2} = \frac{z - A_{\mathrm{z}}}{v_3} \tag{4.52}$$

with

$$\boldsymbol{v} = \begin{bmatrix} H_{\mathrm{x}} - A_{\mathrm{x}} \\ H_{\mathrm{y}} - A_{\mathrm{y}} \\ H_{\mathrm{z}} - A_{\mathrm{z}} \end{bmatrix} = \begin{bmatrix} v_1 \\ v_2 \\ v_3 \end{bmatrix} \tag{4.53}$$

The vector normal to P_2 ($\boldsymbol{n}_2$) is perpendicular to the vector normal to P_1 ($\boldsymbol{n}_1$) and it is also perpendicular to $\boldsymbol{v}$ (this conditions makes P_2 to contain r). Therefore, $\boldsymbol{n}_2$ is computed as the cross product of $\boldsymbol{v}$ and $\boldsymbol{n}_1$:

$$\boldsymbol{n}_2 = \boldsymbol{v} \times \boldsymbol{n}_1 = \begin{bmatrix} v_2 \\ -v_1 \\ 0 \end{bmatrix} \tag{4.54}$$

Given $\boldsymbol{n}_2$ and using H as a point contained in P_2, the elevation plane is defined as follows:

$$P_2 : \ v_2 x - v_1 y + v_1 H_{\mathrm{y}} - v_2 H_{\mathrm{x}} = 0 \tag{4.55}$$

In a more generic way, the equation defining the plane can be written as:

$$P_2 : \ P_{2\mathrm{x}} x + P_{2\mathrm{y}} y + P_{2\mathrm{D}} = 0 \tag{4.56}$$

Positioning of M3, M6 and M7

Two main conditions are imposed to position the robot for the elevation trajectory realization:

1. The end effector pulley (Y) must be positioned in the elevation plane, defined by the shoulder aperture angle θ. This implies that the reference for M3, θ_3^{d}, must be equal to θ: $\theta_3^{\mathrm{d}} = \theta$.

2. An initial distance between the pulley (Y) and the shoulder (H) is imposed, d. For simplicity, this distance d is actually the projection on the ground plane of the distance in the 3D space between H and Y, so the z component is not considered.

The second condition is important because it has an impact in the ergonomics of the movement. There exist different combinations of the positions of motors M6 and M7 which place the pulley in the elevation plane P_2, but there is only one combination that places it at a selectable distance d to H. As previously mentioned, the references for M3, M6 and M7 do not vary during the elevation motion. They are computed for the robot configuration at the start of the arm elevation. Naturally, for this initial configuration, θ_5^{d} is chosen as the maximum allowable value, which places the end effector as close as physically possible from the external end of the elevation rod (Fig. 4.12), and θ_4^{d} is set to 0° (elevation rod parallel to the ground) as the arm elevation angle at the beginning of the trajectory is minimal.

Using both aforementioned conditions, displacements for M6 (d_6) and M7 (d_7) can be computed according to the following procedure. Distance d is computed as

$$d = \sqrt{(Y_{\mathrm{y}} - H_{\mathrm{y}})^2 + (Y_{\mathrm{x}} - H_{\mathrm{x}})^2} \tag{4.57}$$

From the forward kinematics in (4.50):

$$Y_{\mathrm{x}} = S_3 S_4 \left|\mathrm{k}_{45\mathrm{Z}}\right| + S_3 C_4 \left|D_5\right| + -C_3 \left|D_7\right| + S_3 \left|\mathrm{k}_{23\mathrm{Y}}\right| + D_6 \tag{4.58}$$

$$Y_{\mathrm{y}} = C_3 S_4 \left|\mathrm{k}_{45\mathrm{Z}}\right| + C_3 C_4 \left|D_5\right| + S_3 \left|D_7\right| + C_3 \left|\mathrm{k}_{23\mathrm{Y}}\right| + \mathrm{k}_{\mathrm{AOY}} \tag{4.59}$$

$$Y_{\mathrm{z}} = S_4 \left|D_5\right| - C_4 \left|\mathrm{k}_{45\mathrm{Z}}\right| + \left|\mathrm{k}_{23\mathrm{Z}}\right| \tag{4.60}$$

Grouping terms, Y_{x}, Y_{y} and Y_{z} can be written as:

$$Y_{\mathrm{x}} = a_{\mathrm{x}} + b_{\mathrm{x}} \left|D_7\right| + D_6 \tag{4.61}$$

$$Y_{\mathrm{y}} = a_{\mathrm{y}} + b_{\mathrm{y}} \left|D_7\right| \tag{4.62}$$

$$Y_{\mathrm{z}} = a_{\mathrm{z}} \tag{4.63}$$

Substituting in (4.57) and reordering terms:

$$D_6^2 + \left(2a'_{\mathrm{x}} + 2b_{\mathrm{x}} \left|D_7\right|\right) D_6 + C = 0 \tag{4.64}$$

with

$$a'_{\mathrm{y}} = a_{\mathrm{y}} - H_{\mathrm{y}}$$

$$a'_{\mathrm{x}} = a_{\mathrm{x}} - H_{\mathrm{x}}$$

$$C = k + 2a'_{\mathrm{y}} b_{\mathrm{y}} \left|D_7\right| + b_{\mathrm{y}}^2 \left|D_7\right|^2 + 2a'_{\mathrm{x}} b_{\mathrm{x}} \left|D_7\right| + b_{\mathrm{x}}^2 \left|D_7\right|^2 - d^2$$

$$k = a'^2_{\mathrm{y}} + a'^2_{\mathrm{x}}$$

Point Y must belong to the elevation plane P_2, so substituting the coordinates of Y in (4.56):

$$Y_{\mathrm{x}} P_{2\mathrm{x}} + Y_{\mathrm{y}} P_{2\mathrm{y}} + P_{2\mathrm{D}} = 0 \tag{4.65}$$

Solving (4.65) for $|D_7|$, the following expression is obtained

$$\left|D_7\right| = \frac{-1}{P_{2\mathrm{y}} b_{\mathrm{y}} + P_{2\mathrm{x}} b_{\mathrm{x}}} \left(P_{2\mathrm{x}} \left(a_{\mathrm{x}} + D_6\right) + P_{2\mathrm{y}} a_{\mathrm{y}} + P_{2\mathrm{D}}\right) = k_1 D_6 + k_2 \tag{4.66}$$

Substituting (4.66) in (4.64), a second order equation for $|D_6|$ is obtained. Solving that equation, the greatest of the two values is the one that should be chosen since it positions Y in front of the subject (positive region of the Y_{ABS} axis). The reference for motor M6 is then computed as

$$d_6^{\mathrm{d}} = d_6 = D_{6,\max} - \mathrm{k_{AOX}} \tag{4.67}$$

Substituting $|D_6|$ in (4.66), the reference for motor M7 is similarly obtained through

$$d_7^{\mathrm{d}} = d_7 = |D_7|_{\max} - \mathrm{k_{23X}} \tag{4.68}$$

For each aperture angle θ, the subset of feasible distances d between H and Y varies. It is necessary to know which values of d can be achieved for each θ in case the demanded d is not achievable. Details on how to compute the subset of achievable d are shown in Appendix D.3.

Obtention of $\boldsymbol{Y}\,[\boldsymbol{k}]$ point

The point $Y\,[k]$ is obtained through the following three steps.

a) Obtention of straight $\boldsymbol{s}$, perpendicular to vector $\boldsymbol{AH}$, belonging to $\boldsymbol{P_2}$ and which contains point $\boldsymbol{A}$. The director vector of s, $\boldsymbol{q}$, is contained in P_2 and is perpendicular to $\boldsymbol{v}$, so $\boldsymbol{q}$ is computed using the cross product between $\boldsymbol{v}$ and $\boldsymbol{n}_2$:

$$\boldsymbol{q} = \boldsymbol{v} \times \boldsymbol{n}_2 = \begin{bmatrix} q_1 \\ q_2 \\ q_3 \end{bmatrix} \tag{4.69}$$

With $\boldsymbol{q}$ and imposing that s contains A, the straight equation is:

$$s: \ \frac{x - A_{\mathrm{x}}}{q_1} = \frac{y - A_{\mathrm{y}}}{q_2} = \frac{z - A_{\mathrm{z}}}{q_3} \tag{4.70}$$

and the x and y coordinates of the points contained in s are:

$$x = \frac{q_1}{q_3}\,(z - A_{\mathrm{z}}) + A_{\mathrm{x}} \tag{4.71}$$

$$y = \frac{q_2}{q_3}\,(z - A_{\mathrm{z}}) + A_{\mathrm{y}} \tag{4.72}$$

b) Computation of length $\boldsymbol{l}\,[\boldsymbol{k}]$. The cable and textile length in the control period $[k]$, $l\,[k]$, is arbitrarily increased or decreased according to an ascending or descending motion for the arm. The proposed policy for cable length reference generation is based on adding and subtracting an incremental length to the length of the previous control period:

$$\begin{cases} l\,[k] = -fTv_{\max} + l\,[k-1]\,, \text{ascending motion} \\ l\,[k] = fTv_{\max} + l\,[k-1]\,, \text{descending motion} \end{cases} \tag{4.73}$$

where $v_{\max}$ is the cable maximum speed, T is the period at which the trajectory points are computed and $f \in [0, 1]$ is a factor that scales cable speed. Through

simulation it was observed that $f = 0.03\omega_{\mathrm{s}}^{\mathrm{d}}$ (with $\omega_{\mathrm{s}}^{\mathrm{d}}$ the desired angular speed for arm elevation), a fluent movement composition is achieved.

The initial cable length l_0 is computed by the software by winding all the cable over the pulley and setting that position as 0 mm of cable length. From then on, when the cable is unwinded, the system can compute the cable length using the encoder information and the pulley radius.

c) Point belonging to s which is at distance l [k] of point A. The distance between A and Y is determined by:

$$l\,[\mathrm{k}] = \sqrt{(Y_{\mathrm{x}} - A_{\mathrm{x}})^2 + (Y_{\mathrm{y}} - A_{\mathrm{y}})^2 + (Y_{\mathrm{z}} - A_{\mathrm{z}})^2} \tag{4.74}$$

Squaring both sides, substituting Y_{x} and Y_{y} by the coordinate expressions (4.71) and (4.72) and grouping terms:

$$l\,[\mathrm{k}]^2 = (Y_{\mathrm{z}} - A_{\mathrm{z}})^2 \left(1 + \frac{q_1^2}{q_3^2} + \frac{q_2^2}{q_3^2}\right) \tag{4.75}$$

Developing the previous expression:

$$Y_{\mathrm{z}}^2 - 2Y_{\mathrm{z}}A_{\mathrm{z}} + \left(A_{\mathrm{z}}^2 - C_2\right) = 0 \tag{4.76}$$

with

$$C_2 = \frac{l\,[\mathrm{k}]^2}{1 + \frac{q_1^2 + q_2^2}{q_3^2}}$$

Solving (4.76), solutions $Y_{\mathrm{z}1}$ and $Y_{\mathrm{z}2}$ are obtained since s contains two points at a distance l [k] of A. The solution with physical sense is the one with greatest value since the end effector Y is always over the arm, so $Y_{\mathrm{z}} = \max(Y_{\mathrm{z}1}, Y_{\mathrm{z}2})$ is chosen. The coordinates of Y [k] are:

$$Y\,[\mathrm{k}] = \begin{bmatrix} \frac{q_1}{q_3}(Y_{\mathrm{z}} - A_{\mathrm{z}}) + A_{\mathrm{x}} \\ \frac{q_2}{q_3}(Y_{\mathrm{z}} - A_{\mathrm{z}}) + A_{\mathrm{y}} \\ Y_{\mathrm{z}} \end{bmatrix} \tag{4.77}$$

If the arm elevation angle is $\varphi = 0$, a singularity is produced since $q_3 = 0$. In that case, it is straightforward to geometrically obtain the coordinates of Y [k] as:

$$Y\,[\mathrm{k}] = \begin{bmatrix} A_{\mathrm{x}} + l\,[\mathrm{k}]\sin(\theta) \\ A_{\mathrm{y}} + l\,[\mathrm{k}]\cos(\theta) \\ A_{\mathrm{z}} \end{bmatrix} \tag{4.78}$$

Reachability of Y [k]

Once the target Y [k] which guarantees perpendicularity is obtained, it is necessary to check if that point is reachable. If it is not possible to place the end effector in that position, the closest possible position has to be computed and commanded.

a) Computation of rigid frame actuators' references using inverse kinematics. The positions of the actuators that generate Y [k] have to be computed. References for motors M3, M6 and M7 have been previously calculated to position the end effector in the elevation plane, so these are already available. The reference for M1 controls the cable length and it it will be addressed further on. In this way, the resolution of the inverse kinematics is reduced to calculate M4 and M5 positions, d_5 and θ_4.

To solve the kinematics, Y [k] has to be projected in the O_3 frame. The projection is obtained through (4.79), using the forward kinematics in (4.49). A diagram of the elevation rod projected in the YZ plane of the O_3 frame is shown in Fig. 4.13.

$$Y|_3 = \left({}^{\mathrm{ABS}}\boldsymbol{T}_3\right)^{-1} \cdot Y|_{\mathrm{ABS}} = \begin{bmatrix} 0 \\ \mathrm{Y_y}|_3 \\ \mathrm{Y_z}|_3 \end{bmatrix} \tag{4.79}$$

Solving the triangles in Fig. 4.13, references d_5^{d} and θ_4^{d} are obtained:

$$d_5^{\mathrm{d}} = d_5 = \cos\left(\theta_{42}\right)\sqrt{\left(\mathrm{Y_y}|_3\right)^2 + \left(\mathrm{Y_z}|_3\right)^2} - \mathrm{k_{45Y}} \tag{4.80}$$

$$\theta_4^{\mathrm{d}} = \theta_4 = \arcsin\left(\frac{\mathrm{k_{45Z}}}{\sqrt{\left(\mathrm{Y_y}|_3\right)^2 + \left(\mathrm{Y_z}|_3\right)^2}}\right) + \arctan\left(\frac{\mathrm{Y_z}|_3}{\mathrm{Y_y}|_3}\right) \tag{4.81}$$

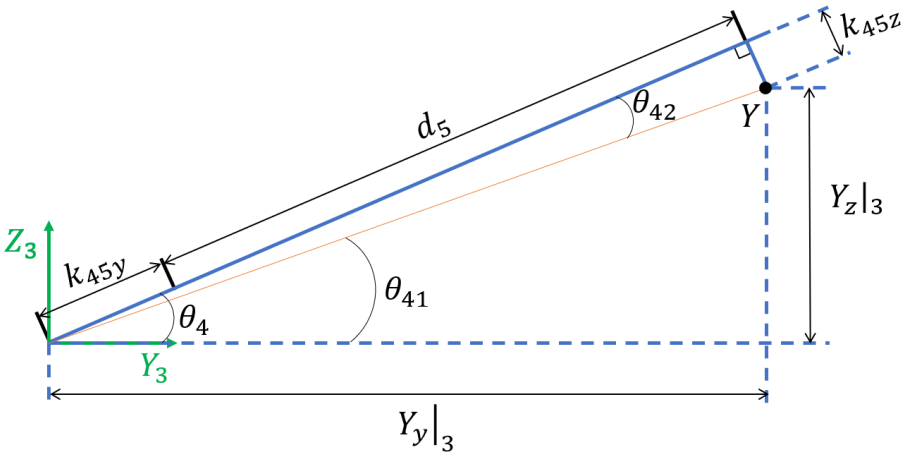


Figure 4.13: Diagram of the elevation rod for the obtention of θ_4 and d_5 given a certain Y [k]. Projection in the O_3 frame.

b) Check if actuator's references are physically reachable. There are two reasons for which an actuator reference can be unreachable. The first one is that the target position is out of range, and the second one is that the necessary actuator speed to achieve the reference within the control period is too high. The first condition is easily evaluated by checking if the actuator reference is within its specific allowable range. To check the second one, the positions obtained if maximum speed were applied, in both senses, are computed. Both conditions are combined in (4.82), which is used to check if there exists position saturation in any of the actuators. The position limits of the i^{th} actuator are denoted by $\mathrm{M_{i,min}}$ and $\mathrm{M_{i,max}}$, the position of

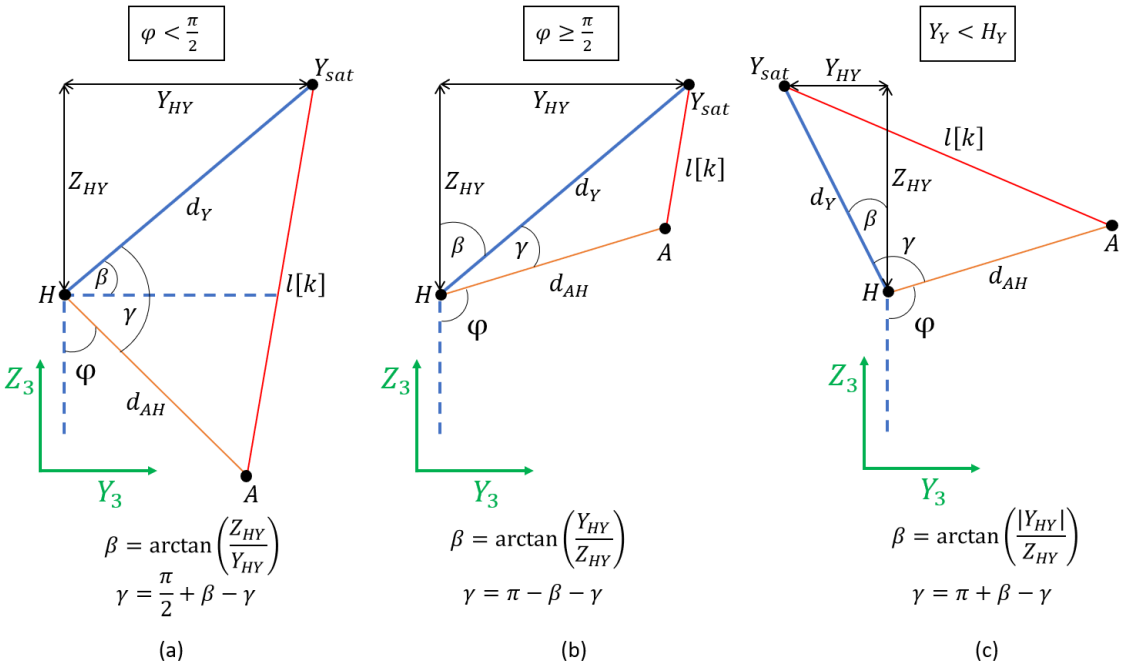


Figure 4.14: Diagram of the possible configurations for the triangle determined by H, A and Y_{sat} for the computation of $l\,[k]$. a) $\varphi < \frac{\pi}{2}$. b) $\varphi \geq \frac{\pi}{2}$. c) $Y_{\text{Y}} < H_{\text{Y}}$, the end effector is behind the shoulder.

the actuator (linear or angular) is pos_i and the actuator maximum speed (linear or angular) is denoted as $\text{v}_{i,\text{max}}$

$$\begin{cases} \text{ref}_{\text{i,min}} = \max\left(\text{M}_{\text{i,min}}, \text{pos}_i\,[k-1] - T\text{v}_{i,\text{max}}\right) \\ \text{ref}_{\text{i,max}} = \min\left(\text{M}_{\text{i,max}}, \text{pos}_i\,[k-1] + T\text{v}_{i,\text{max}}\right) \end{cases} \tag{4.82}$$

If any of the actuators' positions references is unreachable, the new point $Y_{\text{sat}}\,[\text{k}]$ has to be calculated with the saturated positions, according to the forward kinematics in (4.50). Given $Y_{\text{sat}}\,[\text{k}]$, the necessary $l\,[k]$ is computed. For this purpose, it is convenient to work in the O_3 frame:

$$Y_{\text{sat}}| = {}^3\boldsymbol{T}_{\text{ABS}} \cdot Y_{\text{sat}}|_{\text{ABS}} \tag{4.83}$$

$$H|_3 = {}^3\boldsymbol{T}_{\text{ABS}} \cdot H|_{\text{ABS}} \tag{4.84}$$

In this frame, the triangle defined by the points H, A and Y_{sat} has to be solved to determine the length l. Three different geometrical configurations can arise, depending on the arm elevation angle φ and the relative position between H and Y_{sat}. Figure 4.14 shows these configurations and the particularities of each of those. For the three cases, $l\,[k]$ is obtained as follows:

$$l\,[k] = \sqrt{d_{\text{Y}}^2 + d_{\text{AH}}^2 - 2d_{\text{Y}}d_{\text{AH}}\cos\left(\gamma\right)} \tag{4.85}$$

Similarly to the saturation realized over the actuators of the fixed frame, apart from the fact that negative distances for the cable can not be generated, the maximum cable speed is also considered and used to saturate $l\,[k]$:

$$\begin{cases} l_{\text{min}}\,[\text{k}] = \max\left(l_{\text{t}}, -Tv_{\text{l,max}} + l\,[\text{k}-1]\right) \\ l_{\text{max}}\,[\text{k}] = Tv_{\text{l,max}} + l\,[\text{k}-1] \end{cases} \tag{4.86}$$

where $v_{\mathrm{l,max}}$ is the maximum cable speed.

Computation of $\boldsymbol{\theta}_1^{\mathrm{d}}$

The reference for motor M1 is obtained as follows:

$$\theta_1^{\mathrm{d}}[k] = \frac{l\,[\mathrm{k}] - l_{\mathrm{t}}}{\mathrm{r}} \tag{4.87}$$

where r is the radius of the pulley attached to M1 over which the cable winds.

4.3.3 Simulation

A simulation of one full trajectory is presented. The initial arm elevation angle φ_0 was set to 23° (which is around the relaxed shoulder position for the subjects), and the maximum elevation angle was set to 150°. The trajectory profile for this simulation was a simple constant speed trajectory (with $\omega = 10$ deg/s) for elevation and posterior descending of the arm. The aperture angle of the shoulder was set to $\theta = 45°$ and the point generation period T was set to 2 ms. The initial distance between Y and H was set to 0.2 m. The coordinates of H, d_{AH} and l_{t} were extracted from a subject and were $H = [0.69, 0.1925, -0.11, 1]$, $d_{\mathrm{AH}} = 0.28$, $l_{\mathrm{t}} = 0.1$, units in meters.

Evolution of the cable length and speed are presented in Fig. 4.15. Cable speed is within the actuator limits. The position of actuator M1 can be obtained using (4.87). The evolution of the actuators' positions of the structure are plotted in Fig. 4.16. Positions for motors M3, M6 and M7 are constant during the trajectory since the elevation plane is not modified. However, positions for M4 and M5 vary to generate the elevation motion. In time intervals from 0 s to 5.3 s and from 22.7 s to the end of the trajectory, shoulder motion is uniquely generated by M1.

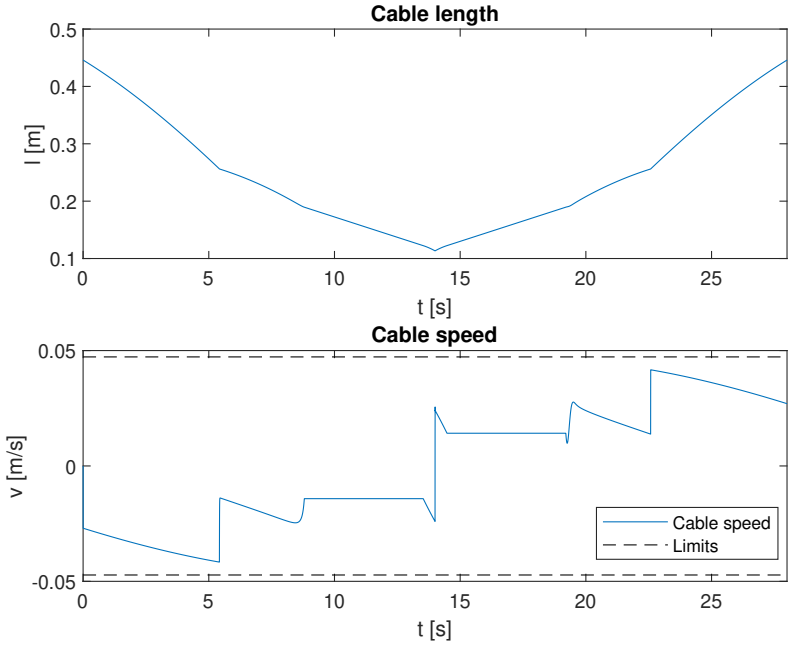


Figure 4.15: Evolution of the cable length and speed.

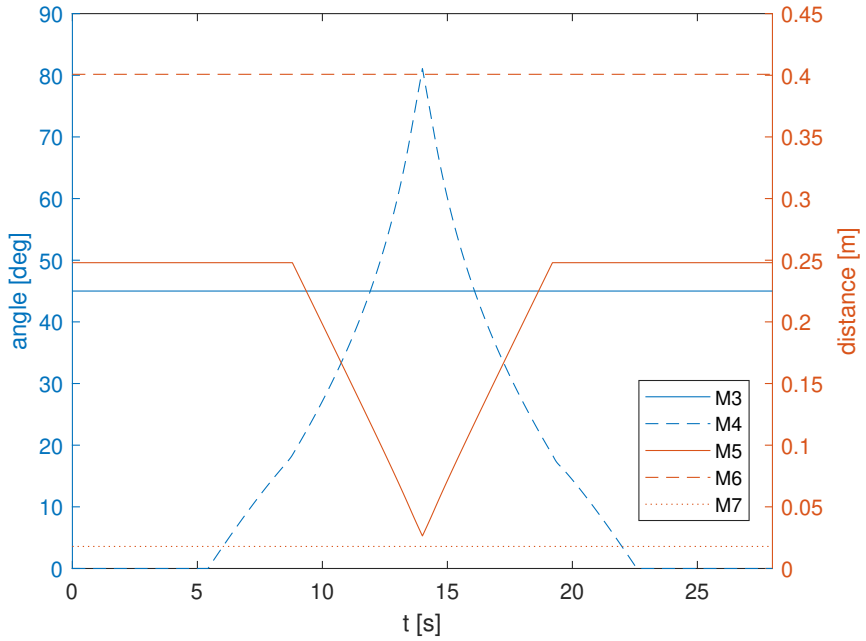


Figure 4.16: Position evolution of the structure's actuators.

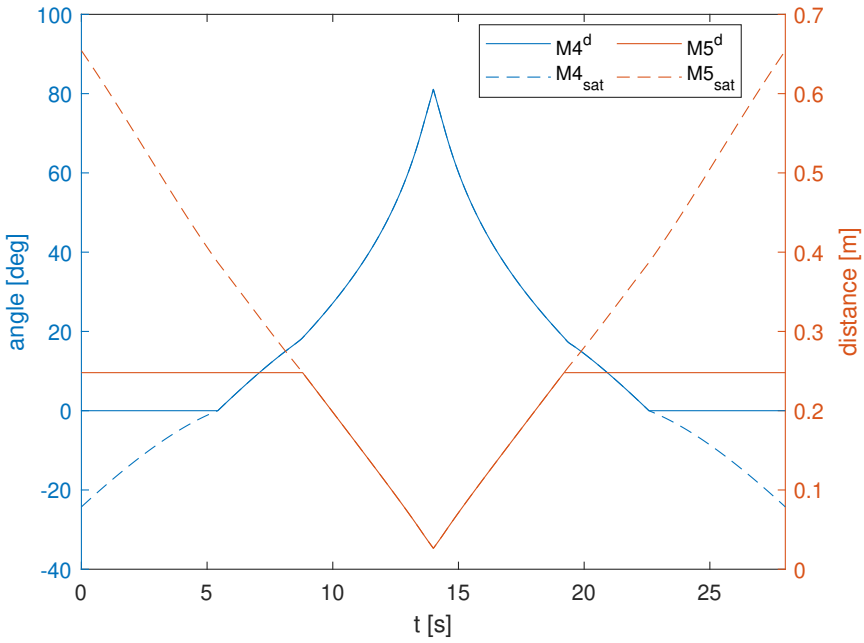


Figure 4.17: Non-saturated and saturated positions for M4 and M5.

Figure 4.17 shows the differences between the reference positions for M4 and M5 and the achievable ones. These positions were calculated to generate perpendicularity between the cable and the arm of the subject. The rigid structure is not able to position the end effector in a way in which perpendicularity is generated for every elevation angle φ [k], as θ_4 and d_5 are saturated. It is geometrically obvious this is not possible for low elevation angles since the elevation rod cannot be positioned in negative angles. Additionally, the longer the elevation rod were, the wider the range

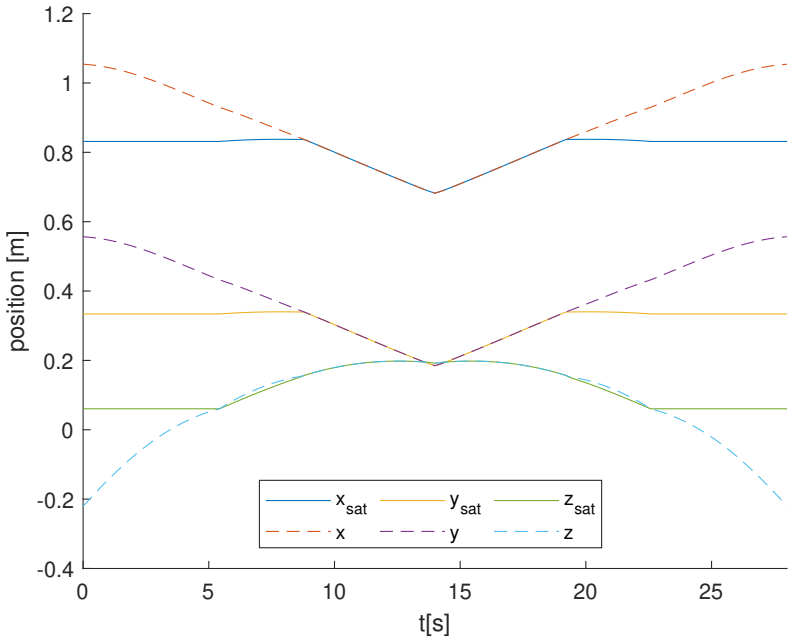


Figure 4.18: Coordinate evolution of Y and Y_{sat} in the ABS frame.

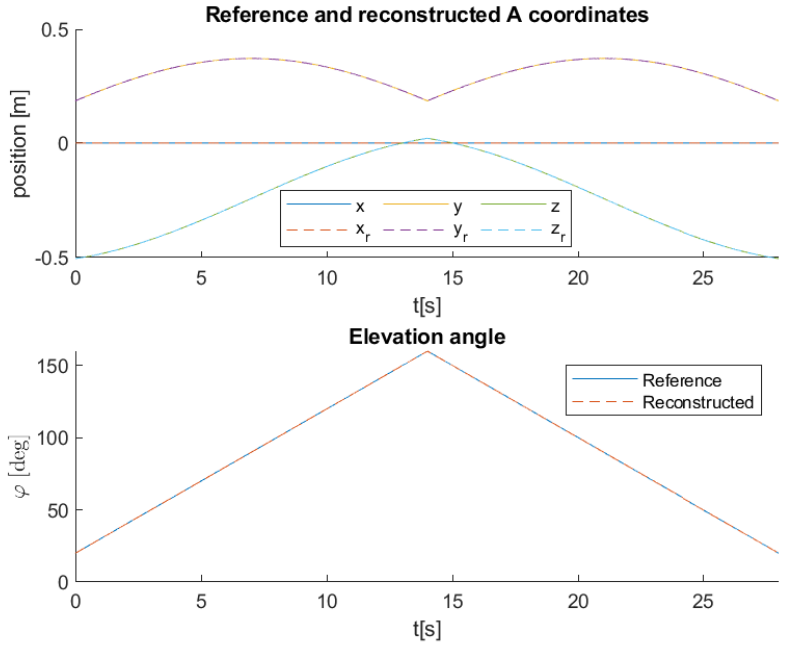


Figure 4.19: Evolution of A coordinates and elevation angle φ. The reconstructed values correspond with the ones set as reference.

of elevation angles in which d_5 were not saturated (and then perpendicularity would be possible) would be. However, there exists a trade-off between the compactness of the robot and the range in which perpendicular force can be applied. Due to the saturation in the actuators M4 and M5, Y cannot always be positioned at the position which generates perpendicularity between the cable and the subject's arm, so Y is substituted for Y_{sat}. Figure 4.18 shows the difference in the coordinates of

Y and Y_{sat}. When there is no saturation in any actuator, the three coordinates coincide and perpendicularity is granted.

Despite the saturation of Y, the coordinates of A and, therefore, the elevation angle φ are successfully tracked due to the proper control of the cable length, as Fig. 4.19 shows. The RMSEs for the coordinates of A are $\text{RMSE}_{A\text{x}} = 4.63\text{e}{-17}$, $\text{RMSE}_{A\text{y}} = 7.70\text{e}{-17}$ and $\text{RMSE}_{A\text{z}} = 6.92\text{e}{-17}$, and the RMSE for elevation angle tracking is $\text{RMSE}_{\varphi} = 3.53\text{e}{-16}$. The angle φ and the coordinates of A were reconstructed according to the geometry shown in Fig. 4.13. It is important to remark that the low-level controllers of the actuators were not included in this simulation as just the precision of the positioning algorithm was to be evalauted.

4.3.4 Motor control

In the CPISDO controller (see Section 4.2) the designed control laws depended on the articular feedback, model parameters and control parameters. Using the geometrical model approach for trajectory generation, the positions for each of the actuators which lead to the desired arm elevation angle are obtained. For this reason, the motors were controlled individually. Stepper motors (M6 and M7) were controlled in open-loop, counting steps. This is not a good practice if high speeds are necessary in the application, because steps could be skipped and, as no feedback is available, there would not exist a way to compensate for them. However, the stepper motors are only used to position the structure in the elevation plane, so the involved speeds in this process can be arbitrarily low, what makes the use of open-loop control a justified option.

To control the DC motors (M1, M3, M4 and M5), individual super-twisting sliding mode controllers were used. Super-twisting SMC was chosen due to its robustness to external disturbances and chattering attenuation. Similarly to the description of the super-twisting controller implemented for two motors in Section 4.2 for CPISDO validation, the individual controllers are described by:

$$\begin{cases} u_i = c_i \left|\sigma_i\right|^{\frac{1}{2}} \text{sign}\left(\sigma_i\right) + w_i \\ w_i = b_i \text{sign}\left(\sigma_i\right) \\ c_i = 1.5\sqrt{C_i} \\ b_i = 1.1 C_i \\ \sigma_i = \sigma_{i1} e_{i1} + \sigma_{i2} e_{i2} + e_{i3} \end{cases} \tag{4.88}$$

where, for the i^{th} motor, u_i is the control action, σ_i is the sliding surface determined by the coefficients σ_{ik}, w_i is the term for chattering attenuation, C_{ij} is a control parameter and e_{ij} are the errors associated to the state of the i^{th} motor (position, speed and current, in this order). Control parameters were set as follows: $C_1 = C_4 = C_5 = 10$, $C_3 = 50$, $\sigma_{11} = \sigma_{31} = \sigma_{41} = 80$, $\sigma_{51} = 2000$, $\sigma_{12} = \sigma_{32} = 25$, $\sigma_{42} = 5$ and $\sigma_{52} = 500$.

4.3.5 Experimental validation

The design of this trajectory generation method was focused in maximizing safety, comfort and reliability. To evaluate, from the patients point of view, the aforementioned characteristics of ExoFlex using the geometrical method for trajectory generation, the System Usability Scale (SUS) [148], [149] was used. This test provides a fast

and standardized tool for measuring the usability of a device. The clinicians' perceived usability, acceptability and satisfaction were also studied through a five-item Likert-type [150] questionnaire. Seven subjects between 50 and 79 years and two clinicians participated in the study. Among the participants, there were pathologies as rotator cuff tendinitis, supraspinatus tendinitis, frozen shoulder, supraspinatus tear and torquiter fracture. This work was conducted in collaboration with and under the supervision of the Physiotherapy, Occupational Therapy, Physical Medicine and Rehabilitation Department of the Rey Juan Carlos University of Madrid, Spain. The protocol was approved by the Research Ethics Committee of the Rey Juan Carlos University. This work was partially published in the author's publication *"Validation of a hybrid exoskeleton for upper limb rehabilitation. A preliminary study"*, MDPI Sensors, vol. 21, no. 21, p. 7342, 2021. doi: 10.3390/s21217342.

At the beginning of the session, the subject sat in the chair and the position of their acromion (H) was measured in the ABS reference frame. The aperture and elevation angles (θ and φ) and the elevation speed ω were selected by the clinicians. Different aperture angles, varying from pure flexion-extension motion ($\theta = 0°$) to pure abduction-adduction ($\theta = 90°$) were set for different subjects. The elevation angles varied between 120° and 160°, according to the level of injury of each of the patients. Each of the subjects performed several elevations for three different aperture angles. Figure 4.20 shows one participant during an elevation trajectory.

Table 4.10 and Table 4.11 respectively show the questions in the SUS and the clinicians' questionnaires. The SUS consists of a 10-item questionnaire with five response options from strongly agree (score of 5) to strongly disagree (score of 1). There are five positive statements and five negative ones, which are presented in alternation. Odd numbered questions (Q1, Q3, Q5, Q7, and Q9) are positive questions, and the recorded scores are the original scores minus by 1. Even numbered questions (Q2, Q4, Q6, Q8, and Q10) are negative questions, and the recorded scores are 5 minus the original ones. Once the results for the ten questions are treated, the score of each question is added and the result is multiplied by a 2.5 factor. The score of the SUS, therefore, ranges from 0 to 100, where a higher score means better usability, with a threshold of 68 that determines the usability of the device.

The SUS questionnaire scores for the subjects ranged from 67.5 to 92.5, with an



Figure 4.20: Patient performing a trajectory elevation up to $\varphi = 145°$ with an aperture angle of $\theta = 30°$. Different frames of the sequence are represented. Source: Author's publication ©Isabel-María Alguacil-Diego et al. 2021; published by MDPI (https://doi.org/10.3390/s21217342).

Table 4.10: SUS questionnaire.

Item	Question
Q1	I think I would use this device frequently
Q2	I find this device unnecessarily complex
Q3	I think the device was easy to use
Q4	I think I would need help from a person with technical knowledge to be able to use this device
Q5	The functions of this device are well integrated
Q6	I think the device has a lack of consistency
Q7	I think that most people would learn to use this device very quickly
Q8	I find the device very difficult to use
Q9	I feel safe using this device
Q10	I needed to learn many things before being able to use this device

Table 4.11: Clinician questionnaire.

Item	Question
Q1	Are you satisfied with ExoFlex?
Q2	Has ExoFlex been useful for the rehabilitation of the upper limb?
Q3	Do you think that ExoFlex could be helpful in the process of upper limb rehabilitation?
Q4	Would you recommend ExoFlex to other clinicians?
Q5	Do you think ExoFlex has advantages compared to other devices?

average score of 80.71, showing a high degree of acceptance by the subjects. The obtained score exceeds 68 which, according to the SUS questionnaire standards, defines a tool as usable. Additionally, as defined in [151], a device with this score can be classified as "Excellent" in the acceptability range. In addition to the SUS questionnaire, the participants were asked about any adverse effects that may have happened during the experiments and no adverse effects were reported. It is remarkable that one of the subjects reported that she felt less pain when the device performed the movement than when the therapist performed it in her regular therapy, reaching in both cases the same elevation angle.

As for the clinicians' questionnaire, the five items were evaluated on a Likert-type scale from 1 to 5 (strongly disagree to strongly agree). The average score for the two clinicians were 4.6 and 4.4, showing a high degree of satisfaction. The question with the lowest score for both clinicians was Q5, in which both remained neutral as a result of their lack of experience using other rehabilitation exoskeletons.

4.4 Discussion

Passive rehabilitation was approached in two very different ways. On the one hand, the CPISDO controller proved to be robust to uncertainty in model parameters and external disturbances, offering a very high accuracy in trajectory tracking, no overshoot and no need of user-specific parameter tuning, which drastically reduces the setup time. However, the fact of including on-body sensors (as IMUs) still gener-

ates some safety challenges. It is not that the IMUs are easily movable from their attaching area, but this still can happen, what compromises rehabilitation safety. A worst-case scenario would arise if an IMU were unattached from the exoskeleton and articular motion were not tracked by the IMU, what would cause the controller to apply maximum voltage with no correct articular feedback and this could harm the subject. In this regard, a very robust fixation system for the IMUs has to be addressed but, additionally, some sort of supervision system which monitors if the voltages applied to the motors and motor states correspond to reasonable articular feedback could be designed to increase safety and robustness to relative movements between the user and the sensor. It is important to remark that the on-body sensor safety issues are not related to the CPISDO controller, as this issues are the same no matter which controller is implemented, as long as on-body sensors are used. The performance of the CPISDO controller was very satisfactory, as analytical and experimental results showed, completely outperforming the super-twisting SMC, the PI controller and other state-of-the-art approaches.

On the other hand, precision in the geometrical method for motion control is limited to the imprecisions made at measuring the subject's acromion position H with respect to the absolute reference frame and the length of the upper-arm d_{AH}. Slacks in the system and modelling imprecisions also compromise the method accuracy. However, the setup time is considerably low, and the fact of not including on-body sensors does not only increase the safety of the system, but it also makes the exoskeleton more comfortable for the subjects. According to the knowledge learnt during the rehabilitation sessions with the clinicians, precision and repeatability are very important, but safety and the perception the subjects have of the device are, at least, as important. The implementation of the porposed geometrical method over ExoFlex without on-body sensors represents an already usable and reliable tool for passive rehabilitation, as shown by the conducted study.

CHAPTER 5

Control for active rehabilitation

5.1 Overview

After a certain time conducting passive rehabilitation, patients increase their range of motion and strength, but there is a point after which no significant improvement is anymore obtained [152]. At this point, strengthening therapies are required to keep increasing range of motion and gaining strength, and this moment is when active rehabilitation comes into play. In active rehabilitation [153], subjects need to actively move their limb. The exoskeleton can provide two types of behaviors: on the one hand, it can assist the motion in the desired direction and, on the other hand, it can oppose to the user motion. Although both options are considered active rehabilitation, it is clear to see that they are substantially different. However, they have in common that the exoskeleton responds in some way to user's motion (favoring or partially preventing the movement), in contrast to passive rehabilitation, in which the user's limb remains relaxed while some predefined trajectories were executed. It is important to remark that the control techniques applied for active rehabilitation are also usable for assistance-focused applications, in contrast to passive rehabilitation controllers.

Either for assisting or preventing the movement, it is necessary to measure the interaction between the subject and the exoskeleton somehow. This can be translated to the need of measuring the force between the user limb and the exoskeleton, the torque of an actuator, the motion of the limb or biological signals, as EMG or EEG. Depending on the exoskeleton design and the application, different methods and implementations can be applied, as will be seen in the following sections.

Two main types of control paradigms can be implemented for active rehabilitation with robots: force/torque control [154]–[163] and impedance/admittance control [164]–[173]. In force or torque control, a force or torque are set as a reference for a body articulation or exoskeleton actuator, and the controller tracks that reference. Talking about force or torque is basically the same, as they can be related via a mechanical model. It is more intuitive to talk about torque in rigid exoskeletons and about force control in cable-driven ones. The control reference can be constant or it can vary according to some kind of criterion, as the position of a specific joint. In this regard, a quite common use of force control is gravity compensation. In this particular mode, the reference force/torque for the interaction between the actuator and the human joint is varied according to the position of the limb, providing the necessary torque to maintain the limb in the position desired by the subject.

Impedance/admittance control consists of generating movement from an interaction force. Mechanical impedance is a measure of how much a body resists motion when force is applied to it. The impedance Z relates the force and speed in the frequency domain as in (5.1). Admittance Y is the inverse of impedance, $Y = Z^{-1}$.

$$F(s) = Z(s) \cdot v(s) \tag{5.1}$$

A high impedance (low admittance) implies that high interaction forces between the exoskeleton and the user have to be applied to generate motion in the system. In contrast, if a low impedance (high admittance) is selected, low forces will be required to generate movement. By properly selecting the impedance generated by the controller, the device can assist the movement or generate resistance to it.

In this thesis, control architectures for active rehabilitation were designed for three different upper-limb exoskeletons. Each of the exoskeletons is completely different to the others in terms of application and construction, so different control

architectures are proposed to properly meet the requirements of each. The actuation systems are different for the three of them, having cable driven transmission, traditional motor-in-articulation transmission and pneumatic actuation. However, all of them must be responsive to motion generated by the user, in one or another way depending on the application. As the exoskeletons presented in this chapter have very different characteristics, it has been structured device-wise. In each of the following sections, first the device is described and, afterwards, the control architectures are developed.

5.2 Elbow exoskeleton for active rehabilitation

According to the authors in [174], there are four basic principles for an elbow rehabilitation program: contention of drawbacks derived by immobilization, avoidance of stressing the healing tissues over a certain limit, fulfillments of some defined clinical criteria before moving from one rehabilitation stage to the next one and basing the rehabilitation plan on up-to-date clinical data that should be adapted to each patient. These principles can be grouped in four chronological stages [175]: *stage of early mobilization* (active-assisted or passive, improves the ROM, articular homeostasis, reduces edema and hematoma and, according to [176], should be started as soon as the inflammatory process is under control and as allowed by healing stage), the *intermediate stage of recovery* (when the elbow ROM is broad and it is possible to work on the recovery of neuromuscular control and gain strength), the *stage of advanced strengthening* (begins when the ROM is complete and it is possible to add resistance during flexion) and the *resumption of working and sporting activity stage* (the exercises depend on the specific former activity of the patient). An elbow exoskeleton that can be used as a tool in the first, second and third stages of the elbow rehabilitation was designed (Fig. 5.1).

The exoskeleton has one active degree of freedom, used for assistance in flexion

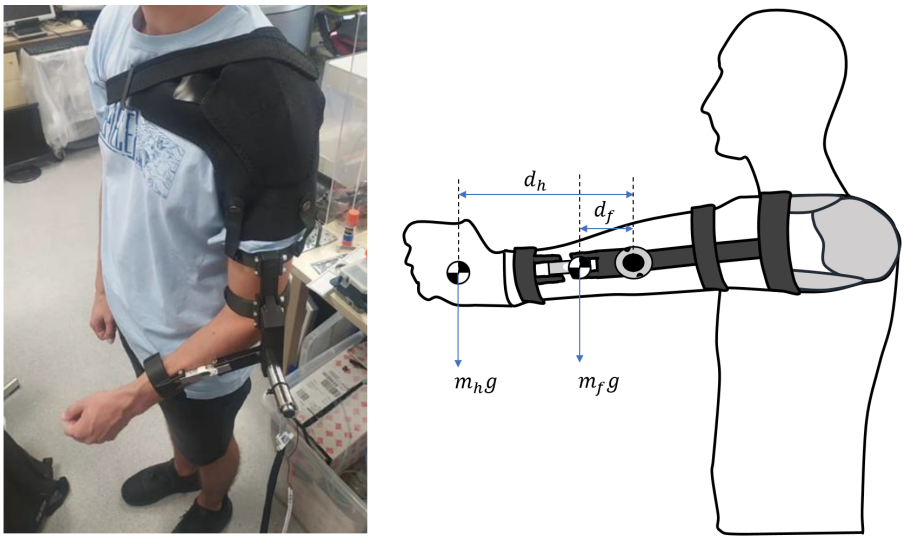


Figure 5.1: Elbow exoskeleton for active rehabilitation and assistance: (a) subject wearing the exoskeleton, (b) diagram of static forces with the arm fully extended.

and extension movements in the range from 0° to around 150°. A DCX22S GB KL 48V Maxon DC motor with a 326 to 1 gearbox drives the exoskeleton. The shaft is directly coupled to the exoskeleton joint, and it can deliver a nominal torque of 4.68 Nm. Considering men's average masses and lengths for the hand and forearm [177], and performing the static analysis of forces in Fig 5.1b, the necessary torque to hold the forearm flexed at 90 degrees is 3.14 N (slightly lower for an average woman), as calculated in (5.2), so the exoskeleton can still assist in the lifting a light load.

$$\tau = m_h g d_h + m_f g d_f = (0.46 \cdot 0.401 + 1.183 \cdot 0.115) \cdot 9.8 = 3.14 \text{ N} \tag{5.2}$$

The mechanical design is based on the EduExo Robotics Kit exoskeleton [178]. Most of the exoskeleton parts were 3D-printed in Onyx [179] (a micro carbon fiber filled nylon that forms the foundation of Markforged composite parts), with the exception of the part which is coupled to the motor's shaft due to the stress it supports (part 3 in Fig. 5.2c), which is made of aluminum. It is a simple design which contains two upper-arm fixations and one for the forearm. The fixations consist of curved structures that partially surround the user's arm and Velcro straps for proper fastening. Different CAD views of the assembly of the exoskeleton and the disassembled parts (along with the DC motor) are shown in Fig. 5.2. From a mechanical point of view, the most interesting part is the the forearm mechanism. The connection between parts 1 and 2, and the connection between parts 2 and 3 were not fully tightened, generating two passive degrees of freedom in those linkages. This allows the forearm fixation to passively reallocate during motion according to the small relative movement generated between the whole exoskeleton and the arm, the elbow flexion angle, and also as a function of the degree of pronosupination of the wearer's forearm. This mechanism increases comfort for the users, as they

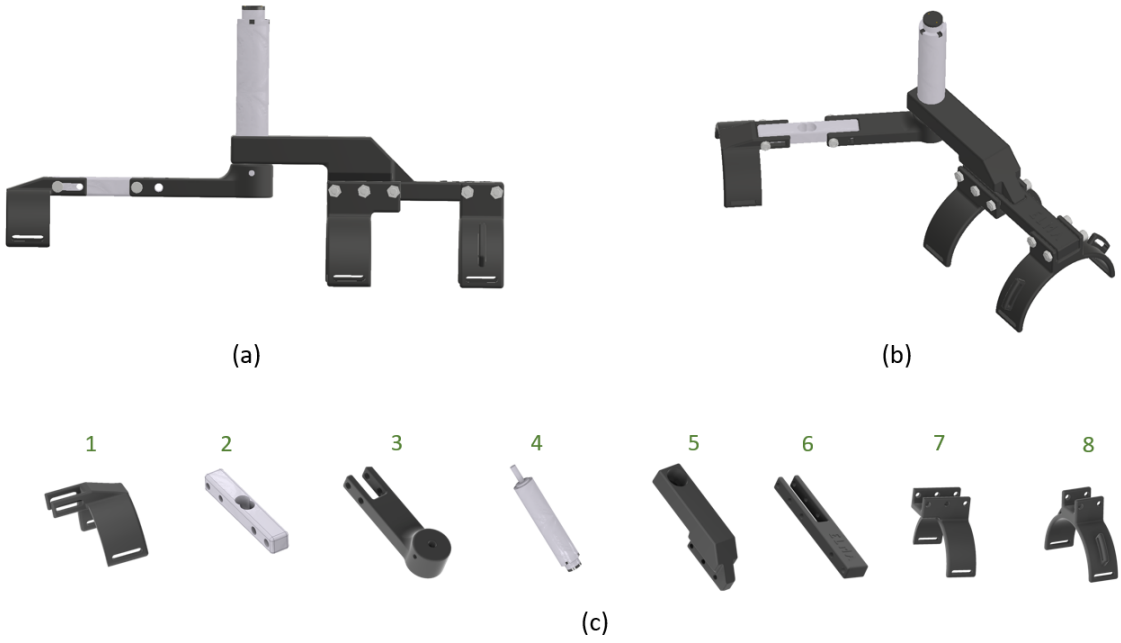


Figure 5.2: Elbow exoskeleton for active rehabilitation and assistance CAD designs: (a) side view of the assembly, (b) 3D view of the assembly, (c) exoskeleton parts and DC motor.



Figure 5.3: Adaptation of the forearm passive mechanism to the user's arm. (a) With the elbow fully extended, the forearm mechanism has a small angle. (b) For this subject, when the elbow is flexed to around 90°, the angle of the forearm mechanism increases.

reported during design stages. Furthermore, it partially overcomes the typical issue in rigid exoskeletons of misalignments between the joint center of rotation and the motor shaft. Figure 5.3 shows how the mechanism adapts to the wearer's body while performing a flexion movement. The exposed behavior was qualitatively observed and documented according to wearers' experience. However, no formal analysis was conducted in this regard since further mechanical studies are out of the scope of this thesis.

In order to improve the fixation of the exoskeleton to the body, a commercial shoulder pad to which the exoskeleton is attached through textile straps was included in the system, as shown in Fig. 5.1a. Fixation buttons were sewn to the shoulder pad to allow the connection with the exoskeleton. It was observed that as time went on using the exoskeleton, it gradually slipped down the arm. With the inclusion of the shoulder pad, fixation was considerably increased, preventing the slipping. It is worth remarking that the donning time for this exoskeleton is around 2 minutes.

5.2.1 System model

The model of the elbow is highly dependent on the shoulder motion. There exist several exercises for elbow active rehabilitation, which involve flexion-extension and pronation-supination movements [180]. Elbow flexion movements are performed with the shoulder at 0 degrees while standing up or sitting down (Fig. 5.4a). Extension exercises can be conducted in supine position (with the shoulder positioned at 0 degrees, Fig. 5.4b, or 90 degrees of flexion, Fig. 5.4c), or standing/sitting (with the shoulder positioned at 90 degrees, Fig. 5.4d, or 180 degrees of flexion, Fig. 5.4e). The shoulder remains in a fixed position while performing the exercises in all the cases. Given that the shoulder is in a fixed position during the exercise realization, it has no dynamic influence over elbow movement. However, the flexion angle for the shoulder and the body orientation of the subject influence the gravitational torque over the system. The system model is developed for the posture shown in Fig. 5.4a and afterwards it will be shown how to very easily adapt the model to the other postures.

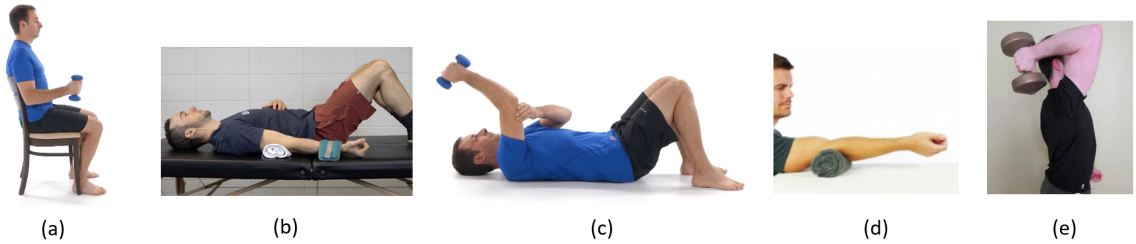


Figure 5.4: Elbow flexion and extension exercises: (a) sitting down, shoulder at 0°, (b) extension in supine position with shoulder at 0°, (c) extension in supine position with shoulder at 90°, (d) flexion/extension sitting down with shoulder at 90°, (e) extension standing up with shoulder at 180°.

A simple diagram of the system is presented in Fig. 5.5. The forearm and the exoskeleton were modelled as a simple rod with moment of inertia J_a, mass m and center of mass located at a distance l_c of the elbow. The torques τ_h and τ_e are the torques applied by the human and the exoskeleton, respectively. The electrical and mechanical components of the motor are also included in the diagram. Model variables are summarized in Table. 5.1.

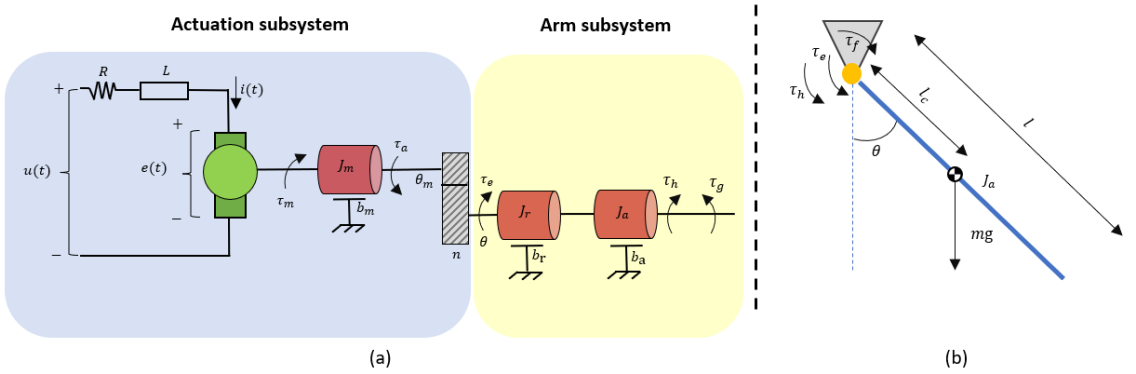


Figure 5.5: Model diagram of the elbow exoskeleton. a) Diagram of torque generation, moments of inertia and torques. b) Diagram of the forearm dynamics.

Table 5.1: Elbow exoskeleton model variables.

Variable	Description
u	Voltage applied to the motor
i	Motor current
e	Motor back electromotive force
τ_{m}	Motor torque
τ_{a}	Gearbox torque over the motor
τ_{e}	Torque delivered by the exoskeleton
τ_{g}	Gravitational torque of the forearm
τ_{h}	Torque applied by the human
τ_{f}	Friction torque
θ_{m}	Motor angle
θ	Elbow angle

Applying classical mechanics analysis to the rotation of the elbow, we have

$$\sum \tau(t) = \tau_{\mathrm{e}}(t) + \tau_{\mathrm{h}}(t) - \tau_{\mathrm{g}}(t) - \tau_{\mathrm{f}}(t) = \\ \tau_{\mathrm{e}}(t) + \tau_{\mathrm{h}}(t) - mgl_{\mathrm{c}} \sin(\theta(t)) - (\mathrm{b_r} + b_{\mathrm{a}})\,\dot{\theta}(t) = (\mathrm{J_r} + J_{\mathrm{a}})\,\ddot{\theta}(t) \quad (5.3)$$

where $\mathrm{J_r}$ and $\mathrm{b_r}$ are the moment of inertia of the gearbox (reductor) and the viscous friction coefficient, and J_{a} and b_{a} are the moment of inertia of the forearm and the elbow viscous friction coefficient. The torques are described in Table. 5.1. Using the same reasoning in the motor's shaft:

$$\sum \tau(t) = \tau_{\mathrm{m}}(t) - \tau_{\mathrm{a}}(t) - \mathrm{b_m}\dot{\theta}_{\mathrm{m}}(t) = \mathrm{J_m}\ddot{\theta}_{\mathrm{m}}(t) \quad (5.4)$$

where $\mathrm{b_m}$ and $\mathrm{J_m}$ are the motor viscous coefficient and moment of inertia, respectively. Applying the relations between angles and torques before and after the gearbox:

$$\tau_{\mathrm{m}}(t) - \frac{\tau_{\mathrm{e}}(t)}{\mathrm{n}} - \mathrm{nb_m}\dot{\theta}(t) = \mathrm{nJ_m}\ddot{\theta}(t) \quad (5.5)$$

The motor torque τ_{m} is generated as follows:

$$\begin{cases} \tau_{\mathrm{m}}(t) = \mathrm{k_p} i(t) \\ u(t) = \mathrm{R}i(t) + \mathrm{L}\frac{\mathrm{d}i(t)}{\mathrm{d}t} + \mathrm{nk_e}\dot{\theta}(t) \end{cases} \quad (5.6)$$

where R is the motor resistance, L is the motor inductance, $\mathrm{k_p}$ is the torque constant and $\mathrm{k_e}$ is the speed constant. Solving (5.5) for τ_{e}, substituting it in (5.3), solving the resulting equation for $\ddot{\theta}(t)$ and considering as state variables $x_1 = \theta(t)$, $x_2 = \dot{\theta}(t)$ and $x_3 = i(t)$, the following state space model is obtained:

$$\begin{cases} \dot{x}_1(t) = x_2(t) \\ \dot{x}_2(t) = \frac{1}{J}\left(-mgl_{\mathrm{c}} \sin(x_1(t)) - bx_2(t) + \mathrm{nk_p}x_3(t)\right) + \frac{1}{J}\tau_{\mathrm{h}}(t) \\ \dot{x}_3(t) = \frac{1}{\mathrm{L}}\left(-\mathrm{nk_e}x_2(t) - \mathrm{R}x_3(t)\right) + \frac{1}{\mathrm{L}}u(t) \end{cases} \quad (5.7)$$

where $b = \mathrm{n^2 b_m} + \mathrm{b_r} + b_{\mathrm{a}}$ is the total viscous friction coefficient and $J = \mathrm{n^2 J_m} + \mathrm{J_r} + J_{\mathrm{a}}$ is the total moment of inertia.

Analogously to what was done in Section 4.2.1, considering model uncertainties and disturbances, for control purposes, it is useful to represent the system in the following way:

$$\dot{\mathbf{x}}(t) = \mathbf{f_0}(\mathbf{x}(t)) + \mathbf{g} \cdot u(t) + \mathbf{g_d} \cdot \mathbf{p}(t) \quad (5.8)$$

with

$$\mathbf{f_0}(\mathbf{x}) = \begin{bmatrix} x_2, & f_{2\mathrm{b}}(x_1, x_2) + f_{2\mathrm{i}}x_3, & f_{03}(x_2, x_3) \end{bmatrix}^\intercal$$

$$f_{2\mathrm{b}}(x_1, x_2) = \frac{1}{J}\left(-mgl_{\mathrm{c}} \sin(x_1) - bx_2\right),\ f_{2\mathrm{i}} = -\frac{\mathrm{nk_p}}{J}$$

$$f_{02} = f_{2\mathrm{b}}(x_1, x_2) + f_{2\mathrm{i}}x_3,\ f_{03} = \frac{1}{\mathrm{L}}\left(-\mathrm{nk_e}x_2 - \mathrm{R}x_3\right),\ \mathrm{q} = \frac{1}{\mathrm{L}}$$

$$\mathbf{g} = \begin{bmatrix} 0 & 0 & \mathrm{q} \end{bmatrix}^\intercal,\ \mathbf{g_d} = \begin{bmatrix} 1 & 0 & 0 \\ 0 & \frac{1}{J} & 0 \\ 0 & 0 & 1 \end{bmatrix},\ \mathbf{p}(t) = \begin{bmatrix} p_1(t) & p_2(t) & p_3(t) \end{bmatrix}^\intercal$$

Note that the human torque τ_{h} is included in the lumped uncertainty and disturbance vector $\mathbf{p}(t)$ as $p_2(t) = \tau_{\mathrm{h}}(t) + d_2'(t) = \tau_{\mathrm{h}}(t) + d_2(t) + \Delta f_2(\mathbf{x})$, being $d_2(t)$ disturbances other than τ_{h} and $\Delta f_2(\mathbf{x})$ the model uncertainty.

If the exercises are performed in the positions shown in Fig 5.4b or Fig 5.4d, the previous model is valid simply considering $x_1 = \theta + \pi/2$. If the exercises are performed in the positions shown in Fig 5.4c or Fig 5.4e, then $x_1 = \theta + \pi$ has to be applied. For simplicity, in the rest of the section, the exposed model, valid for the position in Fig 5.4a, is used.

5.2.2 Impedance control design

An impedance control was proposed for the elbow exoskeleton. This controller allows to regulate the mechanical impedance of the exoskeleton in response to the interaction with the human. Choosing different impedances, the exoskeleton can assist human motion or partially prevent it with different degrees of resistance. As first presented by Hogan in his work [164], [166], [167], this controller is based on an inner-loop position controller. The interaction force between the robot and the environment is measured and, considering a desired impedance Z_d, the motion that would be generated corresponding to the measured interaction force and the desired mechanical impedance is commanded as reference for the position controller. A general diagram of this type of control is shown in Fig. 5.6. The performance of the

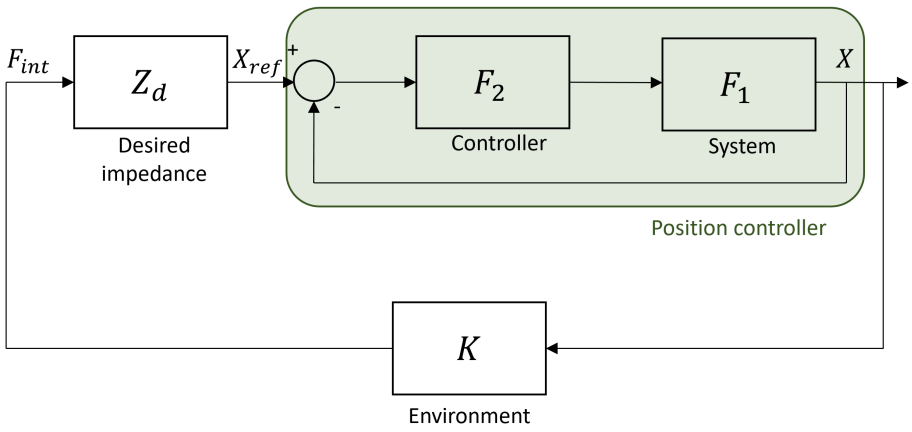


Figure 5.6: General impedance control diagram. Motion reference is generated according to the interaction force F_int and the desired impedance Z_d.

impedance controller highly depends on the position controller. If a zero error were obtained in the inner control loop, the dynamics of the system would correspond to the desired impedance. The lower the position error is, the more similar the controlled impedance will be to the desired one. For this reason, an accurate and robust position controller is necessary to implement an impedance controller.

The proposed impedance controller is shown in Fig. 5.7. Three different controllers were tested in the motion controller block: a PID controller, a super-twisting SMC controller and the CPISDO motion controller, designed in Chapter 4 for ExoFlex. Motion references ($\mathbf{x}_\mathrm{m}^\mathrm{d}(t) = [x_1, x_2]^\intercal$) are computed from the virtual impedance Z_d and the estimation of the torque exerted by the human $\hat{\tau}_\mathrm{h}$, obtained via a model-based approach. The design of the different modules which constitute the impedance controller is exposed in the following subsections.

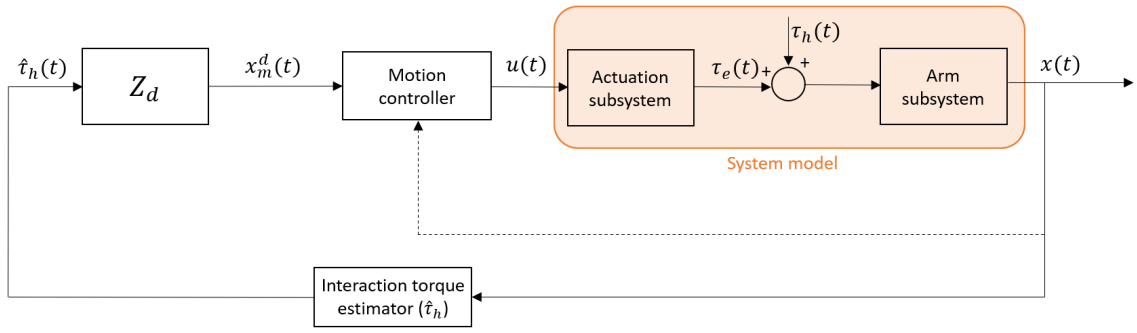


Figure 5.7: Impedance control diagram for the elbow exoskeleton. Motion reference is generated according to the interaction torque estimation $\hat{\tau}_\mathrm{h}$ and the desired impedance Z_d. The state feedback for the motion controller is dashed because only the CPSIDO controller requires state information, but not the PID and super-twsiting SMC.

Inner-loop motion controller

As mentioned before, three different motion controllers were implemented over the exoskeleton. The PID controller does not require further explanation as it is well known and the super-twisting SMC was described in (4.47) and (4.48), so this section is focused on the design of the CPISDO controller.

The mathematical development followed here is analogous to the one in Chapter 4, but particularized for the elbow exoskeleton model. For deeper details on the CPISDO design, Chapter 4 should be consulted. According to the model in (5.8), the error dynamics are derived as

$$\begin{cases} \dot{e}_1 = x_2 + p_1 - \dot{x}_1^\mathrm{d} \\ \dot{e}_2 = f_{2\mathrm{b}}\left(x_1, x_2\right) + f_{2\mathrm{i}} x_3 + p_2 - \dot{x}_2^\mathrm{d} \\ \dot{e}_3 = f_{03}\left(x_2, x_3\right) + \mathrm{q}u + p_3 - \dot{x}_3^\mathrm{d} \end{cases} \tag{5.9}$$

with $e_i = x_i - x_i^\mathrm{d}$, being $x^\mathrm{d}d_i$ the reference for the state x_i. The proposed sliding manifold is:

$$\sigma = \sigma_1 e_1 + \sigma_2 e_2 + e_3 + \sigma_2 \hat{p}_1 + \frac{\hat{p}_2 + \dot{\hat{p}}_1}{f_{2\mathrm{i}}} \tag{5.10}$$

The nonlinear disturbance observer used for this control was the one described by (4.30), presented here again for clarity

$$\begin{cases} \dot{\mathbf{z}} = -\mathbf{L}\mathbf{g_d}\mathbf{z} - \mathbf{L}\left[\mathbf{g_d}\mathbf{L}\mathbf{x} + \mathbf{f_0}(\mathbf{x}) + \mathbf{g}u\right] \\ \hat{\mathbf{p}} = \mathbf{z} + \mathbf{L}\mathbf{x} \end{cases} \tag{5.11}$$

where $\hat{\mathbf{p}} \in \mathbb{R}^3$ is the estimation of the disturbance and uncertainty vector $\mathbf{p} \in \mathbb{R}^3$, $\mathbf{z} \in \mathbb{R}^3$ is the internal state vector of the nonlinear observer and $\mathbf{L} \in \mathbb{R}^{3\times3}$ is the observer gain diagonal matrix. The control input is designed as

$$u(t) = -\frac{1}{\mathrm{q}}\Bigg(\sigma_1\left(x_2 + \hat{p}_1 - \dot{x}_1^\mathrm{d}\right) + \sigma_2\left(f_{02}(\mathbf{x}) + \hat{p}_2 - \dot{x}_2^\mathrm{d}\right) + f_{03}(\mathbf{x}) - \dot{x}_3^\mathrm{d} + \mathrm{k}\psi(\sigma) + \sigma_2\dot{\hat{p}}_1 + \frac{\dot{\hat{p}}_2 + \ddot{\hat{p}}_1}{f_{2\mathrm{i}}}\Bigg) \tag{5.12}$$

being $\psi(\sigma)$ the boundary layer to attenuate chattering already defined in (4.37). Finally, the PI controller which controls the current reference is:

$$x_3^{\mathrm{d}} = \mathrm{k_p}\left(x_1 - x_1^{\mathrm{d}}\right) + \mathrm{k_i}\int_0^t \left(x_1 - x_1^{\mathrm{d}}\right)\mathrm{d}\tau \tag{5.13}$$

The error dynamics of the CPISDO controller are not analyzed here since the procedure and result are analogous to the ones presented in Section 4.2.3.

Proposition 4 *The controller defined by the control law (5.12), the sliding manifold (5.10) and the NDO (5.11) for the system (5.8) assures that the system reaches the sliding mode, if* k *is properly chosen.*

The previous proposition can be proven following the procedure in Appendix C.4 applied to the CPISDO design for ExoFlex.

Human torque estimation

Considering uncertainty in model parameters and the possible application of external disturbances other than the user torque τ_{h}, equation (5.3) can be written as:

$$\tau_{\mathrm{h}}(t) + d_2'(t) = mgl_{\mathrm{c}}\sin(\theta(t)) + b\dot{\theta}(t) + J\ddot{\theta}(t) - \tau_{\mathrm{e}}(t) \tag{5.14}$$

From the model equations, the exoskeleton torque τ_e can be written as:

$$\tau_{\mathrm{e}}(t) = \mathrm{nk_p}x_3(t) - \mathrm{n}^2\left(\mathrm{b_m}x_2(t) + \mathrm{J_m}\dot{x}_2(t)\right) \tag{5.15}$$

Combining both equations, an estimation of τ_h and d_2' can be obtained based in the model. Note that the model uncertainty in this case is critical, since the lower the uncertainty $\Delta f_2(\mathbf{x})$ is, the more accurate the estimation of τ_h will be. Note that in rehabilitation applications, the main source of disturbances will be τ_h, so the term d_2 will not play an important role. The estimation of τ_h assumes no model uncertainty, and is then defined by

$$\hat{\tau}_{\mathrm{h}}(t) = mgl_{\mathrm{c}}\sin(\theta(t)) + b\dot{\theta}(t) + J\ddot{\theta}(t) - \tau_{\mathrm{e}}(t) \tag{5.16}$$

Desired impedance

If we imagine the elbow joint without exoskeleton and with desired inertia J_{d}, desired damping b_{d} and desired elasticity k_{d}, the motion of the forearm, generated by the human torque τ_{h} would be determined by the following dynamic equation:

$$\tau_{\mathrm{h}}(t) = J_{\mathrm{d}}\ddot{\theta}(t) + b_{\mathrm{d}}\dot{\theta}(t) + k_{\mathrm{d}}\theta(t) \tag{5.17}$$

In the Laplace domain and in a more general way, (5.17) can be written as

$$\tau_{\mathrm{h}}(s) = Z_{\mathrm{d}}(s)\,\omega(s) \tag{5.18}$$

were ω is the angular speed and Z_{d} is the system desired impedance, determined by J_{d}, b_{d} and k_{d}. Selecting values for the impedance parameters and having an estimate of τ_{h}, motion references which make the system behave with the desired impedance can be computed by solving (5.17) or (5.18). In other words, the desired impedance determines how motion should be generated according to the input torque τ_{h}.

The most intuitive implementable impedance for active rehabilitation of the elbow is a pure damping ($J_\mathrm{d} = 0$, $k_\mathrm{d} = 0$):

$$\tau_\mathrm{h}(s) = b_\mathrm{d}\dot{\theta}(s) \tag{5.19}$$

With this type of impedance, the motion references (speed and position) for the control period k are computed as

$$\begin{cases} \dot{\theta}^\mathrm{d}[k] = \frac{1}{b_\mathrm{d}}\tau_\mathrm{h}[k] \\ \theta^\mathrm{d}[k] = \theta^\mathrm{d}[k-1] + \mathrm{T}\dot{\theta}^\mathrm{d}[k] \end{cases} \tag{5.20}$$

where T is the control period.

In order to implement an inertia plus damping impedance, the system has the following admittance:

$$Y(s) = \frac{\omega(s)}{\tau_\mathrm{h}(s)} = \frac{1}{J_\mathrm{d}s + b_\mathrm{d}} \tag{5.21}$$

Mapping (5.21) to the z-domain and applying the inverse Z-transform, the motion references are

$$\begin{cases} \dot{\theta}^\mathrm{d}[k] = c_1\dot{\theta}^\mathrm{d}[k-1] + c_2\tau_\mathrm{h}[k-1] \\ \theta^\mathrm{d}[k] = \theta^\mathrm{d}[k-1] + T\dot{\theta}^\mathrm{d}[k] \end{cases} \tag{5.22}$$

with

$$c_1 = e^{-\frac{b_\mathrm{v}}{J_\mathrm{v}}T},\ c_2 = \frac{1}{b_\mathrm{v}}(1 - c_1)$$

In case an elastic component is to be added to the system impedance, the relation between angular position and applied torque is

$$\frac{\theta(s)}{\tau_\mathrm{h}(s)} = \frac{1}{J_\mathrm{d}s^2 + b_\mathrm{d}s + k_\mathrm{d}} \tag{5.23}$$

and the motion references can be computed in the same way.

5.2.3 Experimental tests

The diagram of the electronics used for this setup is presented in Fig. 5.8. It is a much simpler version of the ExoFlex setup (Fig. 3.7), but the modularity in the electronics architecture design eases the obtention of different electronic setups that might be required by different exoskeletons and/or their applications. The ALICE board was used with one motor for these experiments. The motor current x_3 was measured using one of the current sensors included on the ALICE supplementary board (Appendix B). The sensor was calibrated applying currents between -0.4 A and 0.4 A with steps of 0.1 A. As a result, a polynomial of first order with $R^2 = 0.9999$ was obtained. Articular position and speed were measured via the motor encoder. The acceleration $\ddot{\theta}$ was computed by discrete differentiation of the angular speed measured by the motor encoder.

The implementation of this controller requires the use of different variables which not only are noisy, but also have extremely sensitive dynamics, as the motor current x_3, the rotational acceleration of the elbow $\ddot{\theta}$ and the human torque τ_h. In simulations conducted in Matlab, it was observed that the noise of these signals highly

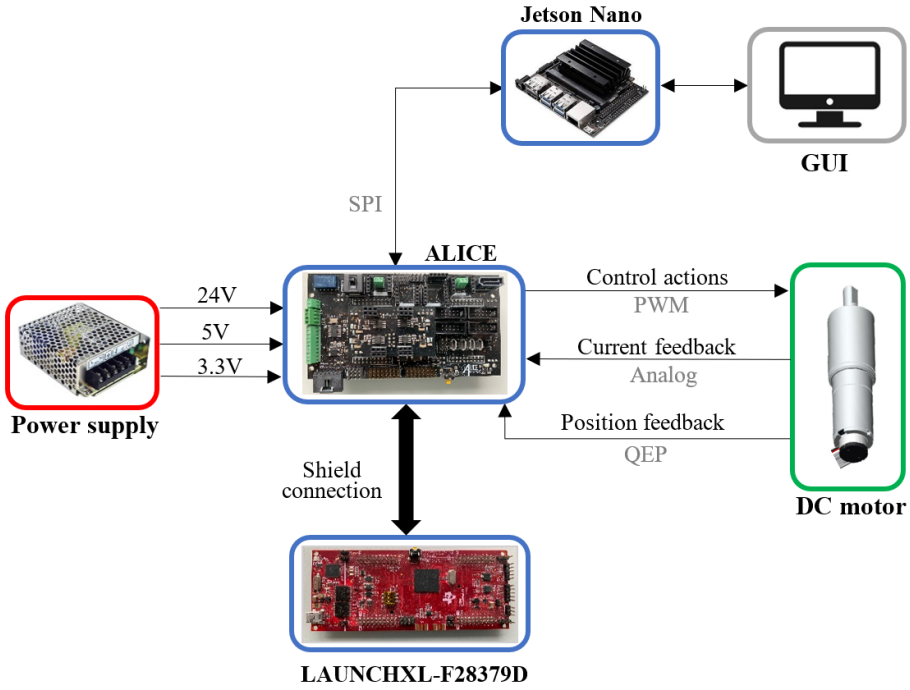


Figure 5.8: Diagram of the electronic system implemented for the elbow exoskeleton for active rehabilitation.

deteriorated the performance of the controllers, even leading to instability. The estimation $\hat{\tau}_{\mathrm{h}}$, which determines the references for the motion controller, depends on the motor current and the elbow acceleration, so $\hat{\tau}_{\mathrm{h}}$ is noisy. When feeding the motion controller with noisy motion references, the overshoot in the motion controller generates more noise in both the motor current and the elbow acceleration, and this serves as a positive feedback for vibratory behavior amplification, which leads to an oscillatory response or instability. In the previous statements, noise is understood as both the classical noise introduced by the sensors and also high frequency components that are part of the signal which, not only are useless for the application, but also worsen the controller behavior.

To mitigate the aforementioned effects, digital low-pass filters were applied to x_3, $\ddot{\theta}$ and $\hat{\tau}_{\mathrm{h}}$. The three signals were filtered with eighth-order low-pass filters with cut-off frequencies of 50 Hz. When the CPISDO was used as motion controller, for its internal execution x_3 was filtered with a second-order low-pass filter with a cut-off frequency of 100 Hz, but the eighth-order filter was still used for the exoskeleton torque estimation. The filters, as well as the controllers, were executed with a period of T = 1 ms.

The system was preliminary tested over two healthy subjects in the laboratory environment (one male and one female). The impedance controller with the three inner-loop motion controllers was simulated in Matlab to obtain initial values of control parameters. The control parameters were slightly adjusted when testing with participants. The sliding surface for the CPSIDO controller and for the super-twisting SMC was the same, to perform a more objective comparison. Control parameters are presented in Table 5.2, and they were the same for both subjects.

For human torque estimation, and prior to starting the experiment, the product ml_{c} in equation (5.16) was estimated for each subject by positioning the subjects

Table 5.2: Control parameters used in experimental tests.

CPISDO	**Super-twisting**	**PID**
$k = 18000$	$C = 20$	$k_p = 110$
$[\sigma_1, \sigma_2] = [24, 11]$	$[\sigma_1, \sigma_2] = [24, 11]$	$k_i = 70$
$\phi = 5$		$k_d = 10$
$[L_{11}, L_{22}] = [2, 2]$		
$[k_p, k_i] = [5, 0.1]$		

elbow at 90°. In that steady position, that product can be computed by measuring the motor current using (5.16) which, under those conditions, simplifies to:

$$ml_c = \frac{nk_p x_3}{g} \tag{5.24}$$

The experiments conducted over the subjects consisted on the execution of two sets of three repetitions of elbow flexion-extension movements, starting with the elbow fully extended. The users were told to flex the elbow above 90 degrees in each repetition, but they had freedom to choose were to stop both flexion and extension movements. The shoulder was left in the relaxed position, adducted to the body.

In this first prove of concept, the desired impedance was set as a pure damping. This type of impedance does not offer an initial extra effort due to an inertia component, nor a position-dependent torque, as an elastic constant does. The author believes this can be a good starting point for evaluation of the controllers for rehabilitation purposes. Each controller was tested with two different damping coefficients: $Z_{d1} = b_{d1} = 3.33\ \frac{Nm}{rad/s}$ and $Z_{d2} = b_{d2} = 1.43\ \frac{Nm}{rad/s}$. These values were chosen arbitrarily after some preliminary tests. Particularly, the inverse of these impedances were selected ($0.3\ \frac{rad/s}{Nm}$ and $0.7\ \frac{rad/s}{Nm}$, respectively) and this is why the impedance values may seem too exact or conveniently selected, so this is why the author offers this clarification. The objective was to evaluate the performance of the controllers with a lower and a higher impedance, as well as to qualitatively evaluate the users' perception with these two proposed impedances. The exact numerical values selected for the impedances are not critical.

Tables 5.3 and 5.4 present the RMSEs associated to the position and speed tracking of the inner motion control loop. Table 5.5 shows the RMSEs of the obtained impedances with respect to the desired ones. For computing the RMSE of the estimated impedance, data points in which the absolute value of the speed is close

Table 5.3: Inner-loop position tracking RMSE [deg].

	Subject	**Subject 1**		**Subject 2**		**Average**	
	$\boldsymbol{Z_d}\ \left[\frac{\mathbf{Nm}}{\mathbf{rad/s}}\right]$	3.33	1.43	3.33	1.43	3.33	1.43
Control	**CPISDO**	0.225	0.728	0.387	0.380	0.306	0.554
	Super-twisting	0.186	0.184	0.218	0.260	0.202	0.222
	PID	0.716	1.582	0.821	1.994	0.768	1.788

Table 5.4: Inner-loop speed tracking RMSE [deg/s].

	Subject	**Subject 1**		**Subject 2**		**Average**	
	$\boldsymbol{Z_d}$ $\left[\frac{\mathbf{Nm}}{\mathbf{rad/s}}\right]$	3.33	1.43	3.33	1.43	3.33	1.43
Control	**CPISDO**	0.315	6.297	0.330	5.492	0.323	5.894
	Super-twisting	0.932	2.238	1.250	2.596	1.091	2.417
	PID	0.943	2.774	1.299	5.042	1.121	3.908

Table 5.5: Impedance RMSE [Nm/(rad/s)].

	Subject	**Subject 1**		**Subject 2**		**Average**	
	$\boldsymbol{Z_d}$ $\left[\frac{\mathbf{Nm}}{\mathbf{rad/s}}\right]$	3.33	1.43	3.33	1.43	3.33	1.43
Control	**CPISDO**	0.145	0.740	0.215	0.759	0.180	0.749
	Super-twisting	0.675	0.772	1.039	0.954	0.857	0.863
	PID	0.426	0.645	0.632	1.074	0.529	0.859

to zero (under 1.5 deg/s) were not taken into account. This was done because the impedance in this case is computed as the ratio of the torque to the angular speed. As the speed gets close to zero, the noise present in both the torque estimation and the speed gain a predominant effect over the real values of the signals, conducting to misleading impedance results. The points which were not considered in the computation of the impedance RMSE are not represented in the impedance plots, leaving blank space to maintain temporal consistence with the plots of the other variables. The RMSEs gathered in Tables 5.3 to 5.5 for both subjects are presented in a graphical way in Fig. 5.9 and Fig. 5.10 for a more intuitive interpretation.

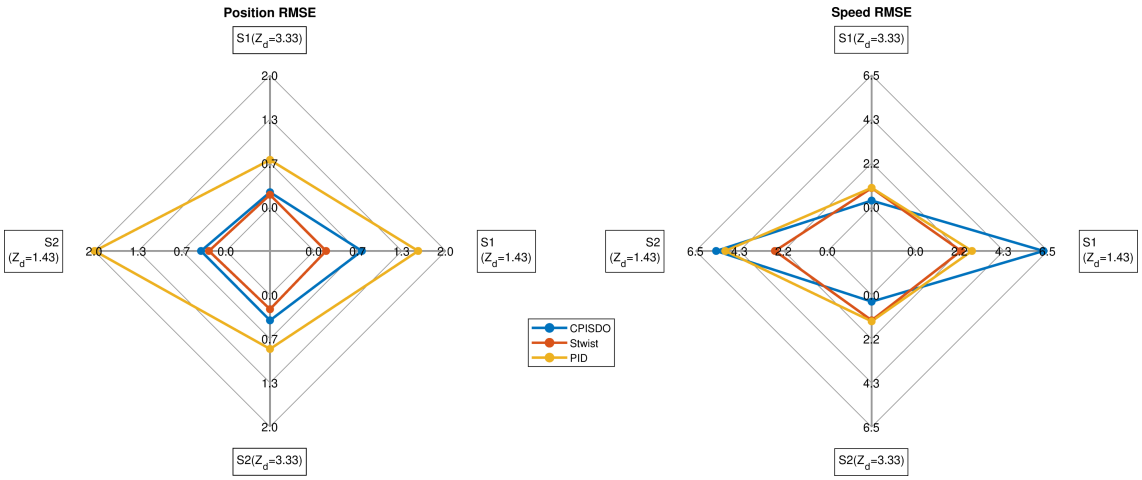


Figure 5.9: Position and speed RMSEs for each controller, subject and target impedance. The units of the RMSEs are the ones corresponding to Table 5.3 and Table 5.4.

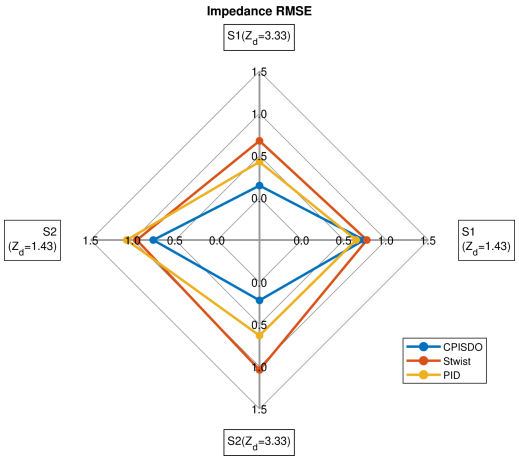


Figure 5.10: Impedance RMSEs for each controller, subject and target impedance. The units of the RMSEs are the ones corresponding to Table 5.5.

With respect to the position RMSE, the super-twisting controller offers the most invariant performance to the subject and target impedance, as well as the lowest RMSE in all cases, as shown in Fig. 5.9a. The position RMSE obtained with the super-twisting controller and the CPISDO are lower than the one provided by the PID, with which position RMSE is considerably lower for both subjects with high impedance than with lower one.

As for the speed RMSE, it is clearly seen in Fig. 5.9 that the tracking errors increase as the target impedance is reduced. This is due to the fact that torque variations with lower target impedance generate higher speed variations, and this hinders the speed tracking for the three controllers. With the higher impedance, the CPISDO offers the lowest RMSE of the three controllers for both subjects. However, the super-twisting SMC provides the best average behavior for the two tested target impedances. The PID controller yields an intermediate performance between the two sliding mode controllers in speed tracking RMSE.

Regarding the impedance RMSE (Table 5.5, Fig. 5.10), the super-twisting SMC generated lower RMSE for subject S1 than for subject S2. The RMSEs provided by the CPISDO for both subjects are noticeably lower with the higher impedance than with the lower one. The highest RMSEs for the CPISDO and PID controllers were obtained for the trial with lower impedance for subject S2, while for the super-twisting SMC, the highest RMSE was observed for the test with higher impedance for S2. In contrast, the lowest RMSEs for all the controllers were obtained for subject S1 using the higher target impedance. In terms of impedance tracking, the three controllers adapted better to subject S1 as the RMSEs are lower for subject S1 than for S2 with any combination of controller and target impedance.

Figure 5.11 and Fig. 5.12 represent the evolution of position, speed, torques, impedance and control action for the experiments conducted over subject S1. Impedance deviates more from the target when the estimated torque is noisy. This can be clearly seen looking at the torque and impedance plots of Fig. 5.11 and Fig. 5.12. The amplitude of the oscillations of the impedance estimations correspond to oscillations in the estimated human torque $\hat{\tau}_\mathrm{h}$. This is mainly observed for the CPISDO and super-twisting controllers. The cause of the oscillation in the estimations of the human torque is directly related to the chattering observed in the control actions for

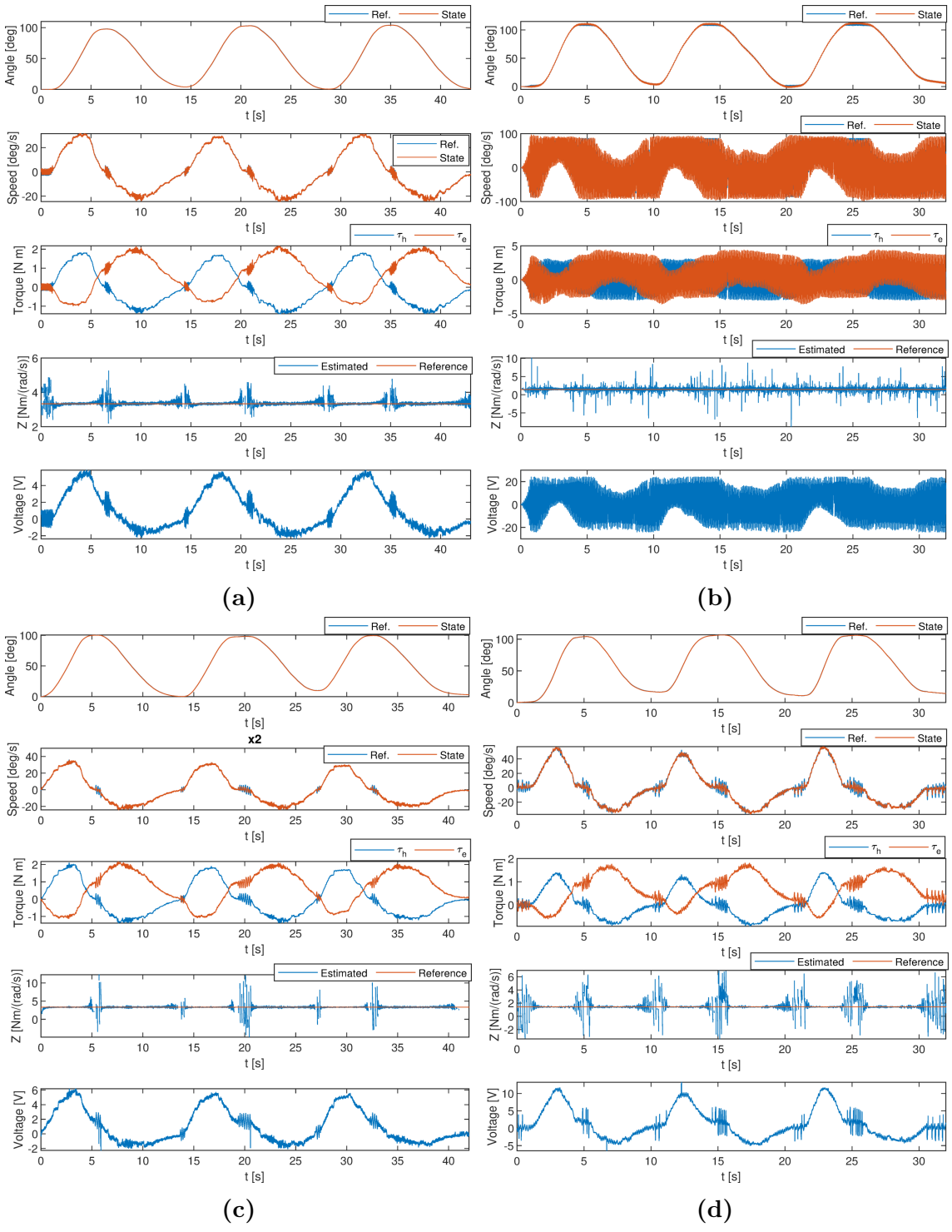


Figure 5.11: Position, speed, torques, estimated impedance and control action for subject S1 using: (a) CPISDO controller with $Z_{\mathrm{d}} = 3.33\ \frac{\mathrm{Nm}}{(\mathrm{rad/s})}$, (b) CPISDO controller with $Z_{\mathrm{d}} = 1.43\ \frac{\mathrm{Nm}}{(\mathrm{rad/s})}$, (c) super-twisting controller with $Z_{\mathrm{d}} = 3.33\ \frac{\mathrm{Nm}}{(\mathrm{rad/s})}$, (d) super-twisting controller with $Z_{\mathrm{d}} = 1.43\ \frac{\mathrm{Nm}}{(\mathrm{rad/s})}$.

these two controllers. The human torque is estimated using the exoskeleton torque, and this is computed using the current of the motor, which is directly affected by the voltage applied to the motor. At the same time, abrupt changes of speed and

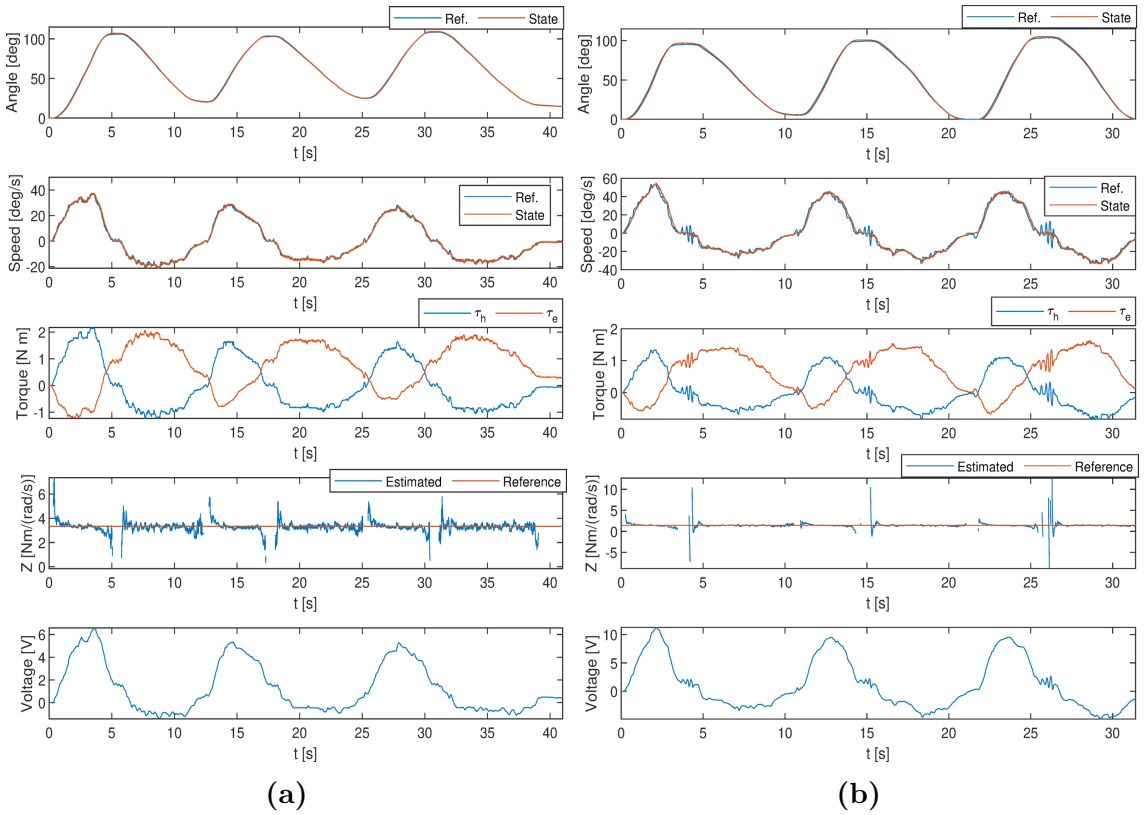


Figure 5.12: Position, speed, torques, estimated impedance and control action for subject S1 using: (a) PID controller with $Z_{\mathrm{d}} = 3.33\ \frac{\mathrm{Nm}}{(\mathrm{rad/s})}$, (b) PID controller with $Z_{\mathrm{d}} = 1.43\ \frac{\mathrm{Nm}}{(\mathrm{rad/s})}$.

position references due to the varying torque estimations imply stronger control efforts for the controllers, which lead to a chattering increase. A clear example of this behavior can be observed for the CPISDO controller with the low target impedance (Fig. 5.11b). Although the position, speed and impedance RMSEs do not suggest this extremely noisy response, as observed in the plots, the behavior of the CPISDO is not suitable for being used with low target impedances, although with the higher impedance, the best behavior was obtained with this controller. Similar results were obtained for subject S2. In contrast to the sliding mode controllers, the PID controller does not present chattering in its control action. For this reason, the torque estimations using the PID controller are cleaner than the ones obtained for the two sliding-mode controllers and, therefore, the deviations from the target impedance due to abrupt variations in the estimated human torque are lower. It is worth mentioning that in the sections in which there is no chattering in the control actions, both the CPSIDO and the super-twisting SMC provide a lower impedance RMSE than the PID controller, although the global performance is deteriorated, as aforementioned, by the chattering.

In regard to the subjects' perception, they did not report major significant comfort issues during the tests, except for the CPISDO controller for the low impedance, which provided an unacceptable oscillatory behavior. Both of them stated they felt more comfortable with the other two controllers using the low target impedance, as they could move with less effort and in a more natural way.

5.3 Shoulder rotation active rehabilitation

Several shoulder injuries are related to the rotator cuff. The rotator cuff is the common name given to the group of four distinct muscles (supraspinatus, infraspinatus, teres minor and scapularis) and their tendons, which provide strength and stability during shoulder motion. Some of the most common pathologies are the rotator cuff tear [181] and the rotator cuff tendinitis [182]. According to [183], full-thickness rotator cuff tears are present in approximately 25% of individuals in their 60s and 50% of individuals in their 80s. The etiology of rotator cuff tearing is multi-factorial and likely a combination of degenerative changes and trauma. Non-trauma rotator cuff tear can be generated by repeating the same shoulder movements during very long periods of time, as a result of a sports activity such as playing baseball or weight lifting, or by tasks associated to repetitive works.

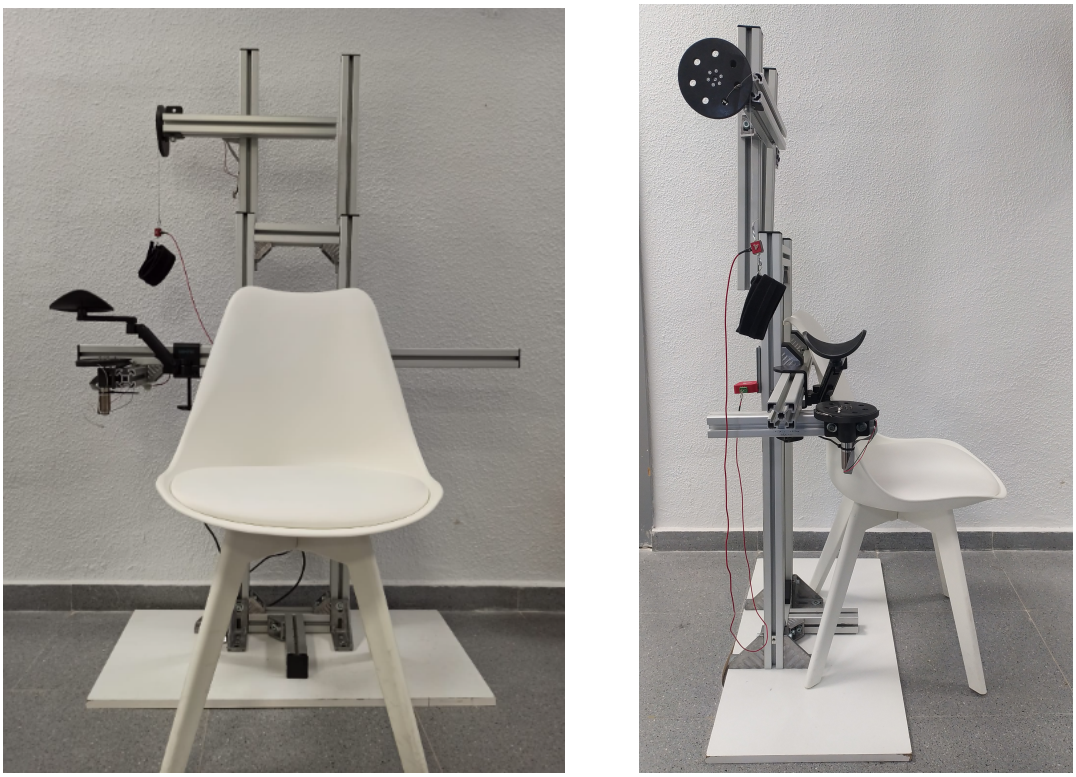
The rotator cuff rehabilitation process should start with a gentle passive range-of-motion program to prevent stiffness. This program can be combined with stooping exercises [184]. Then, internal and external shoulder rotations should be introduced in the therapy to gain strength [185]. According to [186], rotator cuff reaches between high and very high levels of activity when performing shoulder external and internal rotation at 0° and at 90° of abduction.

The results obtained using ExoFlex for passive rehabilitation in collaboration with the Physiotherapy, Occupational Therapy, Physical Medicine and Rehabilitation Department of the Rey Juan Carlos University were promising (Section 4.3.5). As a consequence, the doctors showed interest in including shoulder rotation movements in ExoFlex. In accordance with what has been exposed at the beginning of this section, the clinicians claimed that these movements are crucial for performing rehabilitation of the rotator cuff. ExoFlex had already covered a reasonably large shoulder ROM for passive rehabilitation, but the rotation movements were uncovered. With the objective of meeting the clinicians' proposal, the research group decided to develop a new cable-driven exoskeleton (or rehabilitation device) to perform active rehabilitation of the rotator cuff through internal and external shoulder rotations. Differently to the work previously exposed on the cable-driven exoskeleton ExoFlex for passive rehabilitation, for the shoulder rotation exoskeleton, motion is not generated according to predefined angular trajectories but, in this case, force commands are set for the tensions in the cables and the motion is generated according to the user's force application over the system.

5.3.1 Robot design

The rehabilitation robot presented in this section (Fig. 5.13) was designed to perform active shoulder external rotation with the arm adducted to the body and the elbow flexed at 90° (rotations in the transverse plane), as well as internal and external rotation with the shoulder abducted at 90° and the elbow flexed at 90° (rotations in the vertical plane).

The rehabilitation device is constituted by a chair on which the subjects sit to perform the rehabilitation. A fixed frame was built to allocate the electronics and actuators. The frame was built with Bosch Rexroth aluminum profiles, similarly to the ExoFlex exoskeleton. The location of the actuators is suitable for the performance of the shoulder rotation exercises in the transverse and vertical planes,



(a) **(b)**

Figure 5.13: Cable-driven rehabilitation device for shoulder rotation active rehabilitation: (a) frontal view, (b) lateral view.

and those positions can be modified to better adapt to the body of different subjects. Additionally, the frame can be easily reconfigured to perform rehabilitation of both shoulders. During the experimentation with the robot, no major actuator position adjustments had to be done, apart from switching to left or right shoulder depending on the subject's injured one. The robot has two actuators. One of them is used for external rotation in the vertical plane and the other one can be used for internal rotation in the vertical plane or for external rotation in the transverse plane. The actuators are DCX22S GB KL 48V Maxon DC motors with 326 to 1 gearboxes. They are attached to the rigid frame via 3D-printed coupling parts. An also 3D-printed pulley with a radius of 51 mm is attached to each of the motors' shafts in order to wind and unwind the cable and, therefore, vary the cable length. The radius of the pulley highly impacts the maximum speed at which the system can work, as well as the maximum deliverable torque to the human limb. It was chosen as a trade-off between these two magnitudes (more details are provided in the following subsection). Speed and position of the actuators are measured with incremental encoders. An armrest was added to increase user comfort when performing exercises in the vertical plane.

The electronics system used for this robot (Fig. 5.14) is an adaptation of the architecture presented in Fig. 3.7. The cable tension is measured through a LSB205 Futek load cell. This sensor can measure loads up to 111 N. The strain gauge analog amplifier IAA100 provided by Futek was used to condition the signal measured by the sensor. This amplifier provides a voltage output between -5 V and 5 V. The amplifier was configured to use the positive voltage range for tension forces

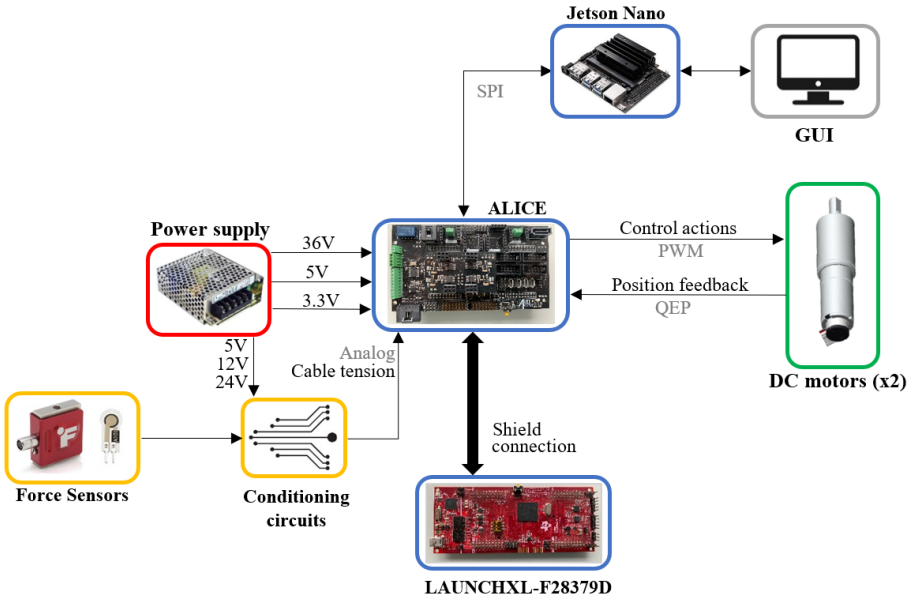


Figure 5.14: Diagram of the electronic system implemented for the shoulder active rehabilitation robot. In the "Force Sensors" box, the left sensor is the Futek LSB205 and the right one is the FlexiForce A101 sensor.

(which are the forces to be measured in the application as the system is cable-driven), while the negative was left for compression ones. The analog inputs for the F28379D microcontroller must be in the range between 0 V and 3 V, so an additional conditioning circuit was added at the output of the IAA100 to suppress the negative voltages and compress the 0 V to 5 V range to 0 V to 3 V. The proposed circuit was formed by a precision rectifier along with a voltage divider (Fig. 5.15), for which precision resistors with tolerances of 0.1% were selected. The set formed by the load cell and the conditioning circuitry provides a sensitivity of 27 $\frac{\text{mV}}{\text{N}}$. Given that the ADCs incorporated in the F28379D microcontroller have a resolution of 12 bits, the resolution of the ADC in newtons is 0.027 $\frac{\text{N}}{\text{LSB}}$.

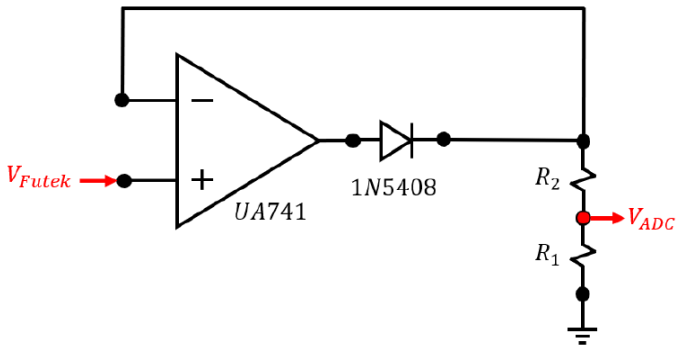


Figure 5.15: Conditioning circuit for Futek LSB205 load cell.

For the calibration process of the Futek load cell, the sensor was hung from an aluminum profile and a plastic bag was hung from the other end of the sensor. Precision weights were added to the bag and the system recorded the ADC readings for each of the selected calibration weights. The average of 10,000 ADC samples for each of the weights was used as the calibration value for those weights. Two sets of

Table 5.6: Futek LSB205 and FlexiForce A101 main characteristics.

Characteristic	**LSB 205**	**A101**
Hysteresis	0.10%	4.50%
Nonlinearity	0.10%	3.00%
Nonrepeatability	0.05%	2.50%
Full scale	111 N	44 N
Cost	$675.00	$10.73

precision weights were used. Each of them contained a 1 kg, two 500 g, a 200 g, two 100 g, a 50 g, two 20 g and a 10 g parts. The parts were combined to record data for weights in the range of 10 g to 4 kg, increasing the weight with smaller steps for low weights and with bigger steps for larger ones. A second-order polynomial which relates the ADC readings with the tension force was obtained through least-squares regression.

As an alternative for the Futek LSB205 load cell, the design of a low-cost cable tension sensor was proposed. The sensor was based on the FlexiForce A101 piezoresistive [187] force sensor (see Fig. 5.14). The A101 is 7.6 mm × 15.6 mm and has negligible thickness. It can measure forces up to 44 N. The comparison of main characteristics of the Futek and FelxiForce sensors is shown in Table 5.6 (errors are presented as percentage of full scale). If the system escalated in number of cables, as for example, performing active rehabilitation with the two shoulders at the same time or adding simultaneous elbow mobilization, the use of a less precise sensor could be justified by a drastic reduction in the sensor system cost. The cable tension sensor based on the FlexiForce A101 sensor is still in development stages and has not been employed in this study. Details on the design of this novel sensor are presented in Appendix E.

5.3.2 Kinematic model

The obtention of the system's kinematic model accomplishes two main purposes. First, it allows to obtain the relationship between the tension in the cables and the normal force to the rotation movement which generates torque for shoulder rotation. Secondly, the model allowed to study the ranges in which the radii of the pulleys could be designed, according to the speed relationship between the motor pulley and the shoulder rotation, considering also the motor torque.

Figure 5.16 presents the kinematic diagrams for shoulder rotation movements in the transverse and vertical planes. The following kinematics analysis corresponds to the movement in the transverse plane (Fig. 5.16a), but if the same process is applied to the situation in Fig. 5.16b, the same results are obtained for shoulder rotation in the vertical plane. Table 5.7 describes the main variables involved in the geometrical model for rotation in the transverse plane. The variables involved for rotation in the vertical plane are analogous to the ones in the transverse plane, but with a subscript corresponding to the superior or inferior motor.

The relation between the cable length and motor angle is given by

$$l_3(t) = l_{30} - r\theta(t) \tag{5.25}$$

where l_{30} is the cable initial length with minimal tension and the shoulder rotated

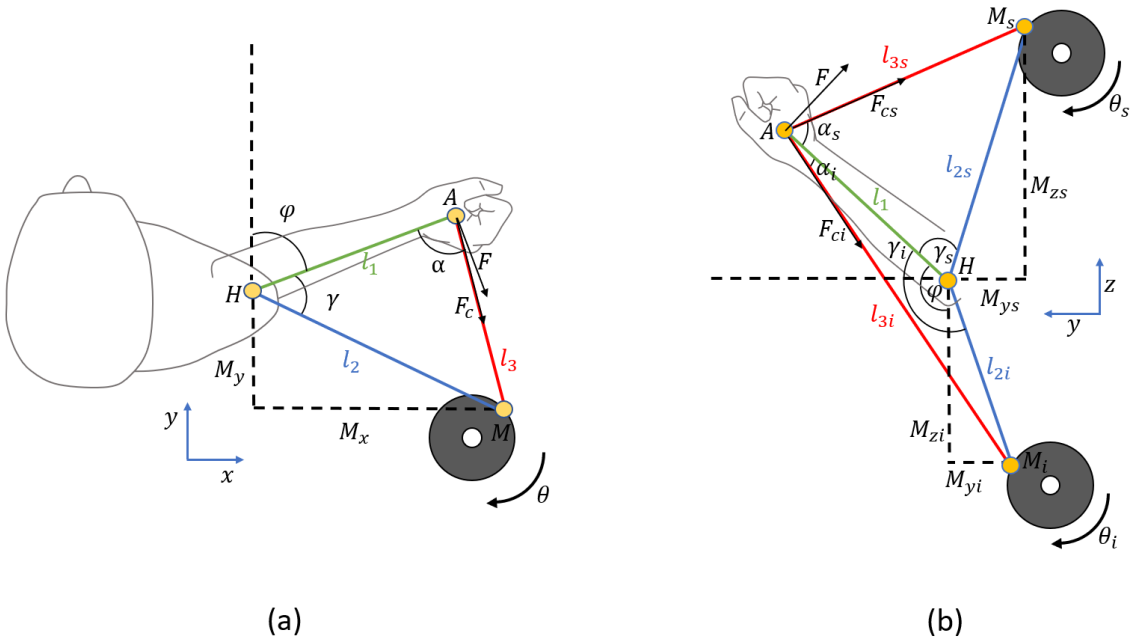


Figure 5.16: Geometrical diagram of shoulder rotation movements in: (a) transverse plane, (b) vertical plane. Subscripts "s" and "i" stand for superior and inferior motors, respectively.

Table 5.7: Geometrical model parameters for shoulder rotation.

Variable	Description	Variable	Description
H	Shoulder rotation center	A	Contact point between human and cable
M	Insertion point of the cable over the pulley	φ	Shoulder rotation angle
α	Angle between the arm and the cable	γ	Angle between the arm and the HM segment
θ	Motor angle	l_1	Distance from H to A in the XY plane
l_2	Distance from H to M in the XY plane	l_3	Cable length
F_c	Cable tension force	F	Normal force to the arm

at 0°, and r is the radius of the motor pulley. Applying the law of cosines to the triangle defined by the points H, A and M and using (5.25), the relation between α and θ is obtained as follows:

$$\alpha\left(t\right)=\arccos\left(\frac{l_1^2+\left(l_{30}-r\theta\left(t\right)\right)^2-l_2^2}{2l_1\left(l_{30}-r\theta\left(t\right)\right)}\right) \tag{5.26}$$

Using expression (5.26), the relation between the axial tension in the cable F_c and the normal force to human limb F, which generates the shoulder rotation motion, is obtained as

$$F\left(t\right)=F_c(t)\sin\left(\alpha(t)\right) \tag{5.27}$$

Expression (5.27) can be used to generate force control references for the cable which correspond to a certain normal force applied to the arm.

To obtain the relationship between the shoulder rotation angle φ and the motor angle θ, φ can be computed as the difference in γ between the initial position and whatever position depending on time, making use again of the law of cosines over the MAH triangle:

$$\varphi(t) = \gamma(\varphi = 0) - \gamma(t) = \pi - \arctan\left(\frac{M_\mathrm{x}}{|M_\mathrm{y}|}\right) - \arccos\left(\frac{l_1^2 + l_2^2 - (l_{30} - \mathrm{r}\theta(t))^2}{2l_1 l_2}\right) \tag{5.28}$$

The relation of arm and motor speeds ($\dot{\varphi}$ and $\dot{\theta}$, respectively) is obtained through derivation of (5.28):

$$\dot{\varphi}(t) = \frac{\mathrm{r}}{l_1 l_2} \frac{l_{30} - \mathrm{r}\theta(t)}{\sqrt{1 - k_1(t)^2}} \dot{\theta}(t) \tag{5.29}$$

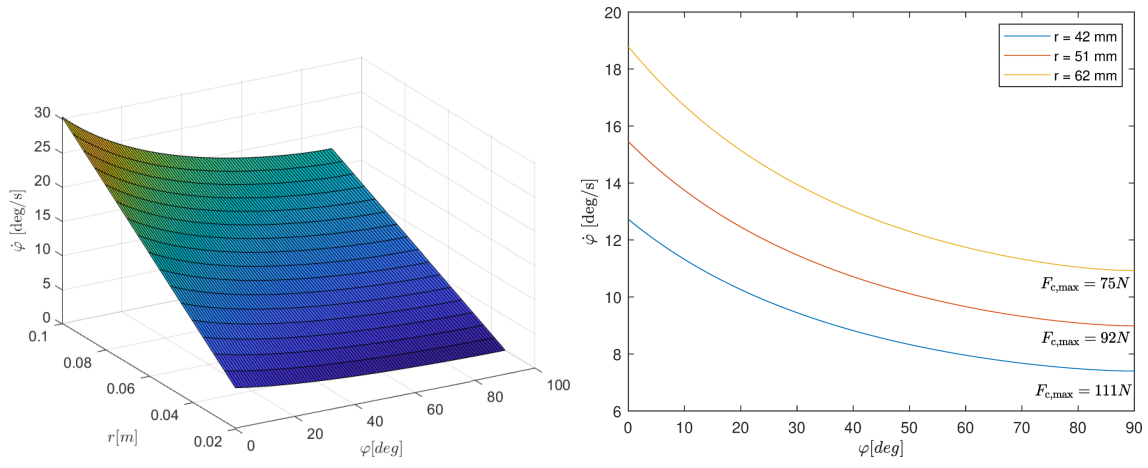
with

$$k_1(t) = \frac{l_1^2 + l_2^2 - (l_{30} - \mathrm{r}\theta(t))^2}{2l_1 l_2} \tag{5.30}$$

Expression (5.29) can be written as a function of φ instead of θ, which is more convenient to study the influence of the shoulder rotation angle on the achievable speed:

$$\dot{\varphi}(t) = \frac{\mathrm{r}}{l_1 l_2} \sqrt{\frac{l_1^2 + l_2^2 - 2l_1 l_2 \cos\left(\pi - \arctan\left(\frac{M_\mathrm{x}}{|M_\mathrm{y}|}\right) - \varphi(t)\right)}{1 - \cos^2\left(\pi - \arctan\left(\frac{M_\mathrm{x}}{|M_\mathrm{y}|}\right) - \varphi(t)\right)}} \dot{\theta}(t) \tag{5.31}$$

Analyzing (5.31), it can be observed that, for low shoulder rotation angles, a concrete motor speed $\dot{\theta}$ generates a greater shoulder rotation speed $\dot{\varphi}$ than for high angles. The dependence of this relation on the pulley's radius was studied for a



(a) **(b)**

Figure 5.17: Shoulder rotation speed plots with maximum motor speed for a subject: (a) surface dependent on pulley radius and shoulder rotation angle, (b) speed as a function of rotation angle for three different radii along with the corresponding maximum cable forces.

close-to-average male subject (70 kg, 1.82 m), for whom the main geometrical variables were $l_1 = 0.35$ m, $l_2 = 0.33$ m and $l_{30} = 0.56$ m. Figure 5.17a shows the surface constituted by the pulley radius, the rotation angle and the resulting shoulder speed when the maximum motor speed $\dot{\theta}_{\max} = 3.03$ rad/s is applied. Figure 5.17b represents equation (5.31) for the selected pulley radius $r = 51$ mm and two other values, assuming the motor maximum speed. Achievable rotation speeds are adequate for rehabilitation therapy, in which fast movements are not required.

The maximum torque applicable by the motor is 4.68 Nm and, as aforementioned, the LSB205 measurement range is up to 111 N. These two constraints determine the minimum pulley radius such that the maximum motor torque generates a cable tension in the sensor measurable range:

$$\mathrm{r}_{\min} = \frac{\tau_{\max}}{F_{\max}} = \frac{4.68}{111} = 42 \text{ mm} \tag{5.32}$$

Applying the constraint in (5.32) and observing Fig. 5.17a, a radius of $r = 51$ mm was selected, offering a speed increase with respect to $\mathrm{r}_{\min}$ but not leading to a loss of applicable force F_{m}, as larger radii would do according to (5.32). The maximum tension forces in the cables corresponding to three different radii values are annotated in Fig. 5.17b.

5.3.3 Control design

A force controller for cable tension was proposed. However, when the system starts, there might be a certain amount of unwinded cable. Applying force control in this situation can generate a big overshoot in the controller. For this reason, a speed controller was proposed to control the motor in this first stage of the movement. The speed controller is used until the measured force by the sensor surpasses a predefined threshold $F_{\min} = 1.5$ N during a certain time t_{w}. Once this condition is met, the force controller for cable tension control is executed. A PI controller was used as the speed controller. The transfer function between the motor's voltage and speed was obtained, the controller was adjusted cancelling the slowest pole of the system and the gain was adjusted through simulation. A fast and overshoot-free response was obtained.

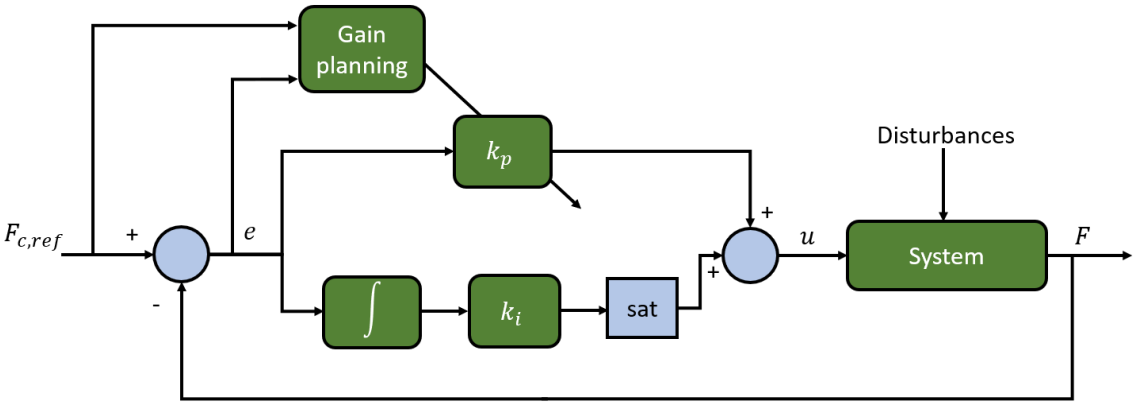


Figure 5.18: Diagram of the proposed adaptive PI controller for cable tension control.

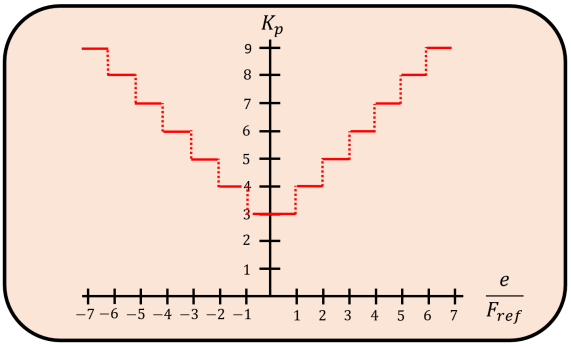


Figure 5.19: Gain planning protocol for proportional gain k_p of the adaptive PI controller.

For the force control of the cable, a PI with anti-windup and gain planning was proposed (Fig. 5.18). A simple PI controller was first tested, but the results were not satisfactory as high proportional gain generated vibrations in the system of a too high amplitude, while a lower proportional gain generated a too high force tracking error. The proposed gain planning is presented in Fig. 5.19. The proportional gain of the PI controller is modified in discrete steps according to the ratio of the force error to the force reference. This approach offered a more stable and precise performance than using a classic PI controller. The integral gain was set as $k_\mathrm{i} = 2$. The parameter tuning was performed experimentally.

The performance of the tension controller was evaluated through three in-lab tests over shoulder rotation in the transverse plane with a healthy participant. Force cable references of 5 N, 10 N and 15 N were used, as recommended by the clinicians involved in the study. The tests started with a 0° shoulder rotation angle (hand pointing to the front). The subject had freedom to move their arm as desired, letting the robot assist the rotation or preventing its movement. Figure 5.20 shows the force and control action for the 5 N and 15 N tests. The areas in which the force error considerably increases correspond to movements performed by the user, against which the motor has to generate a considerable cable length variation to follow the

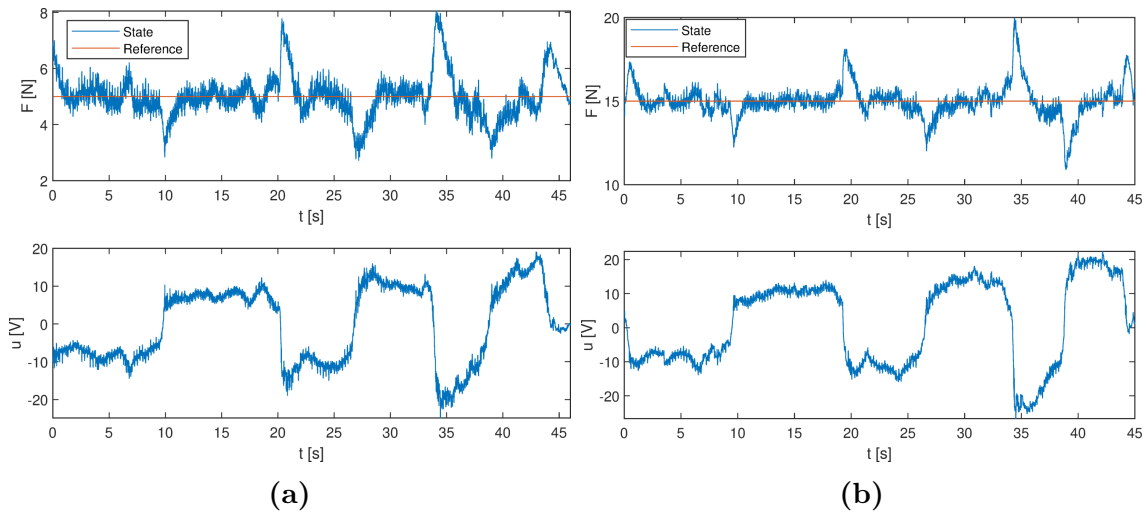


Figure 5.20: Plots for force control and control action in validation of the adaptive PI controller for cable tension control: (a) $F_{\mathrm{c,ref}} = 5$ N, (b) $F_{\mathrm{c,ref}} = 15$ N.

force reference. The RMSEs obtained for force tracking in these validation tests were as follows: $RMSE_{5N} = 0.81$ N, $RMSE_{10N} = 0.81$ N and $RMSE_{15N} = 1.05$ N.

5.3.4 Clinical trials

A preliminary clinical trial was conducted over 11 participants (total of 12 shoulders, as one of the patients suffered a pathology in both), males and females between ages of 35 and 67 years. The subjects' pathologies are presented in Table 5.8. This study was performed in collaboration with and under the supervision of the Physiotherapy, Occupational Therapy, Physical Medicine and Rehabilitation Department of the Rey Juan Carlos University of Madrid, Spain. The protocol was approved by the Research Ethics Committee of the Rey Juan Carlos University. The study had two main goals. On the one hand, to evaluate if the subjects obtained an increase in their shoulder rotation range of motion after using the robot. On the other hand, a *System Usability Test* ([148], [149]) was conducted to evaluate the usability of the device perceived by the participants.

Table 5.8: Age, sex, shoulder and pathology of the subjects involved in the shoulder active rehabilitation evaluation.

Subject	**Age**	**Sex**	**Side**	**Pathology**
Subject 1	66	M	Right	Supraspinatus tear
Subject 2	45	F	Right	Supraspinatus tear with luxation and calcific tendinitis
Subject 3	67	M	Right	Full rotator cuff tear
Subject 4	57	M	Left	Supraspinatus calcific tendinitis
Subject 5	46	M	Right	Supraspinatus suture due to subacromial syndrome
Subject 6	42	F	Right	Supraspinatus tendinitis
Subject 7	66	M	Right	Recovery after arthrolysis due to shoulder capsulitis
Subject 8	52	F	Right	Supraspinatus tear
Subject 9	65	F	Right	Rotator cuff tendinopathy
Subject 10	35	F	Right	Supraspinatus tendinitis
Subject 11	61	F	Right Left	Rotator cuff tendinitis Supraspinatus and infraspinatus tear

The procedure followed with each of the participants was as follows:

1. The participant received their normal rehabilitation therapy with the physical therapist.
2. The shoulder rotation range of motion was measured with a goniometer after the therapy and it was annotated.
3. Using the robot, the subject performed 30 shoulder rotation movements in the transverse plane and 30 rotation movements in the vertical plane.
4. The shoulder rotation range of motion was measured again with a goniometer and it was annotated.

5. The subject was asked to fill in the SUS questionnaire.

The exercises performed with the robot started with a force reference for the cable of $F_{c,ref} = 5$ N, and as long as the subjects felt more confident and comfortable with the device, the reference force was elevated up to a value between 10 N and 15 N, depending on the subject's feelings and always according to the clinician's indications. The participants were told to perform the repetitions at a speed with which they felt comfortable. At the same time, they did not have an angular target, but the clinicians instructed the participants to move out of their comfort area while not suffering too much pain. The pain, of course, was associated to their pathology and the participants reported that the level of pain during the repetitions was not higher than in the previous traditional therapy session. Figure 5.21 shows one of the participants performing shoulder rotation exercises in both the transverse and vertical planes.

The shoulder rotation angles before and after performing the exercises with the robot assistance are presented in Fig. 5.22. The results show that there was an increases in the angular range for 10 of the 12 treated shoulders. The increase in the angular range of motion for subjects S5, S7 and S9 is remarkable, obtaining differences beyond 20°. However, subjects S3 and S6 suffered a decrease in the maximum achieved rotation angle. This could be due to a need of force reference increase for these subjects, for whom the applied forces during experimentation might have not been high enough for their requirements, therefore leading to a cooling down of the shoulder. Another explanation is that these subjects might have not felt confident enough using the device as to let it rotate the shoulder as much



(a) **(b)**

Figure 5.21: Subject performing active rehabilitation with the shoulder rotation robot. Shoulder rotation movements are performed in: (a) transverse plane, (b) vertical plane.

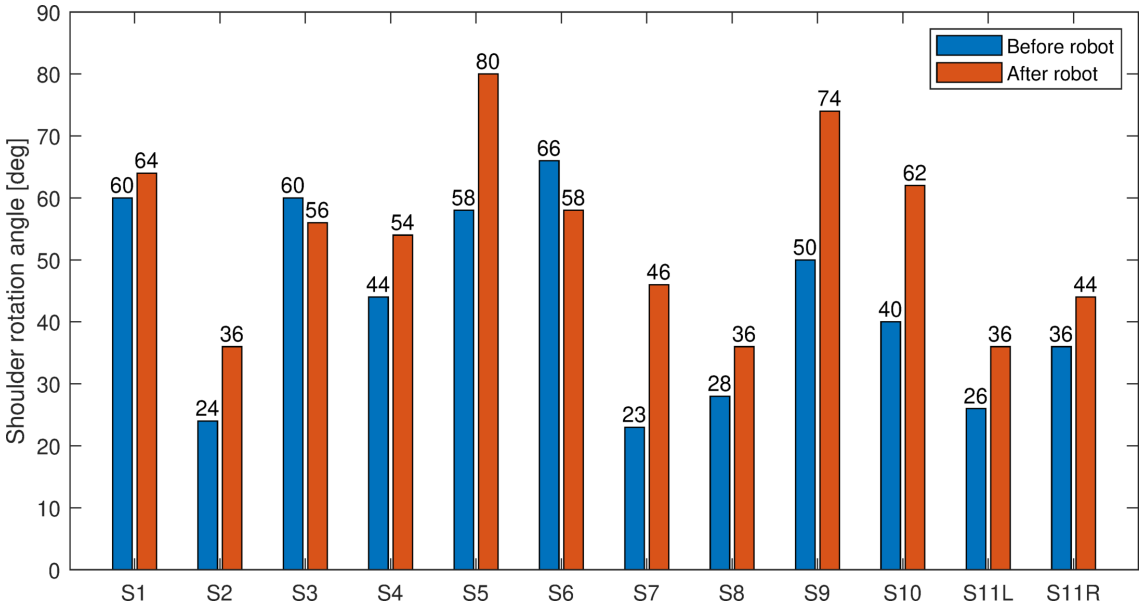


Figure 5.22: Comparison of shoulder rotation angular range before and after performing therapy with the robot.

as the other subjects. It is well worth remembering the fact that all the subjects had been treated with traditional therapy just before using the rehabilitation robot, which increases the significance of the obtained results in comparison with a scenario in which the subjects had been resting before using the device.

Regarding the SUS questionnaire results, an average score of 80.68 was obtained which, according to [151], allows to classify the device usability as "Excellent". The SUS questionnaire has been previously presented in Table 4.10. The scores obtained for each participant are represented in Fig. 5.23.

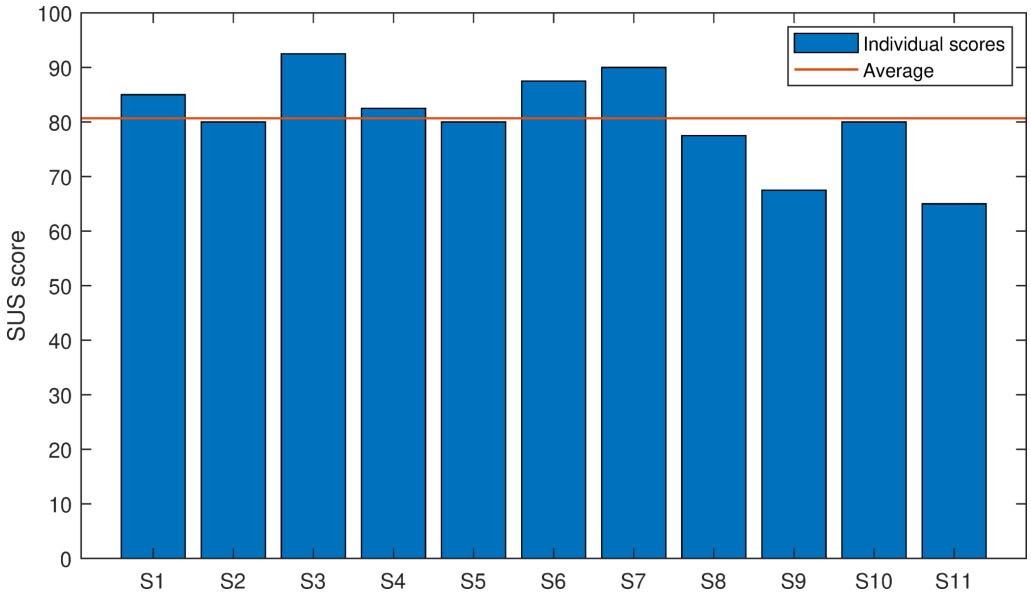


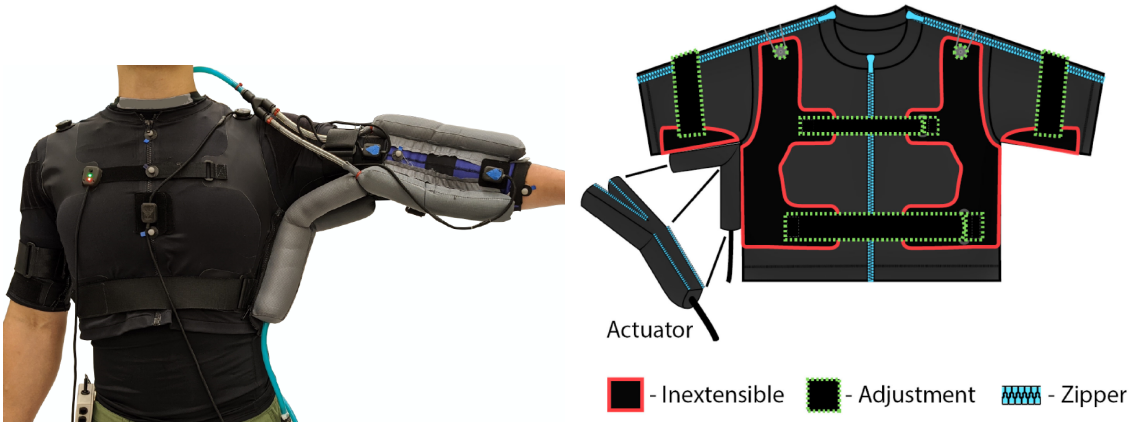
Figure 5.23: SUS scores for the shoulder active rehabilitation assistive robot.

5.4 Inflatable soft wearable robot

The work presented in this section was conducted at the Harvard Biodesign Laboratory, Harvard University, Cambridge, MA, USA, during the author's doctoral stay. The purpose of this collaboration was to contribute to the control and electronics systems of an inflatable soft wearable robot.

5.4.1 Robot description

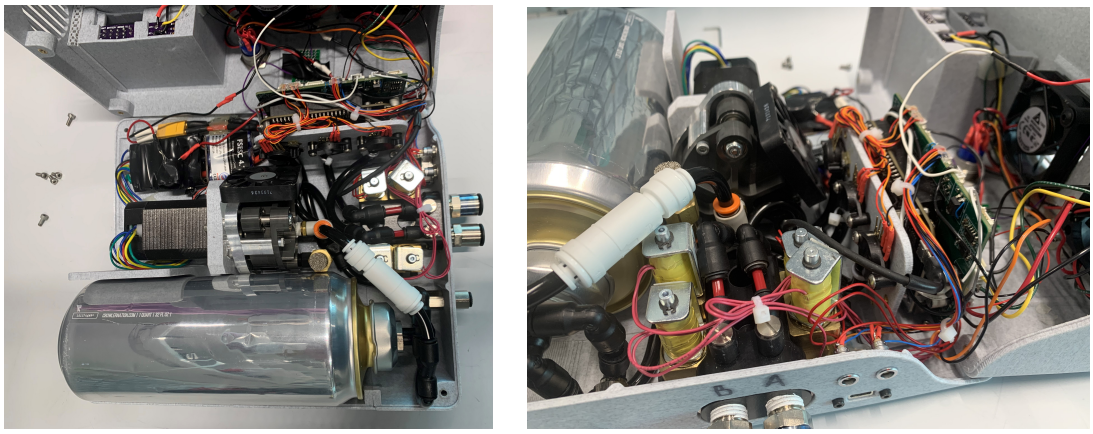
The device described in this section [188]–[190], designed by the research group, is a textile-based multi-joint soft wearable robot which assists the upper limbs, particularly, elbow extension and arm elevation (shoulder flexion-abduction in any plane). Figure 5.24a shows a subject wearing the soft robot and Fig. 5.24b presents the structure of the wearable device. The main goal of this robot is to provide assistance to stroke survivors in ADLs. Shoulder motion is actuated by a textile-based inflatable actuator which is anchored to the torso and upper-arm via functional apparel. The actuator has a bifurcation at the end which attaches to the arm side to better adapt the user's anatomy and increase comfort. The apparel contains inextensible elements, which are used for anchoring the actuator and to transmit forces around the torso, as well as adjustment elements to better adapt to each user's physical constitution. The zippers installed along the top of the sleeves help donning the robot. When the shoulder actuator is inflated, torque is applied over the glenohumeral joint and the device assists arm elevation. Similarly, another inflatable actuator was designed to assist elbow flexion and extension. The work conducted by the author with this robot was focused on arm elevation control, so the elbow will be left aside in the rest of the section.



(a) **(b)**

Figure 5.24: Soft wearable robot for upper-limb assistance: (a) subject wearing the robot, with elbow and shoulder actuators (picture extracted from [190]), (b) diagram of the soft wearable robot (picture extracted from [188]).

The actuation system consists of an air pump, a VESC (Vedder electric speed controller) for the pump speed control, a 1 L air accumulator, a custom designed 3D-printed air manifold and four proportional valves. The valves are structured such that the device has two actuation channels (one for the shoulder and one for the elbow, or one for each shoulder, as the modularity of the system allows



(a) **(b)**

Figure 5.25: Opened actuation and control box: (a) top view, (b) lateral view.

interchangeability of actuators), for each of which one valve can introduce air into the inflatable actuator and the other one opens the actuator to the atmosphere so that air is released from the inflatable chamber. The system includes three analog pressure sensors (one for each actuator and another one for the accumulator). The pump can work with pressures up to 40 psi and the actuators maximum pressure is around 15 psi. For articular motion measurement, a set of IMUs is used. To interface all the actuators and sensors, a Beaglebone Black Wireless is used. This board includes an ARM Cortex A8 at 1 GH and two PRU 32-bit microcontrollers. A Linux OS can be run in the main processor, will the Processing Realtime Units can be used in parallel for fast computing. A shield-like PCB was designed for the Beaglebone. This board includes all the necessary hardware to interface sensors and actuators, as well as the power electronics modules. This PCB was already partially designed and the author contributed to its completion. The system is powered by two 4S batteries connected in series. The control box is compact and the user can easily carry it attached to their waist with a belt.

In the following subsections, the control architecture proposed for the system

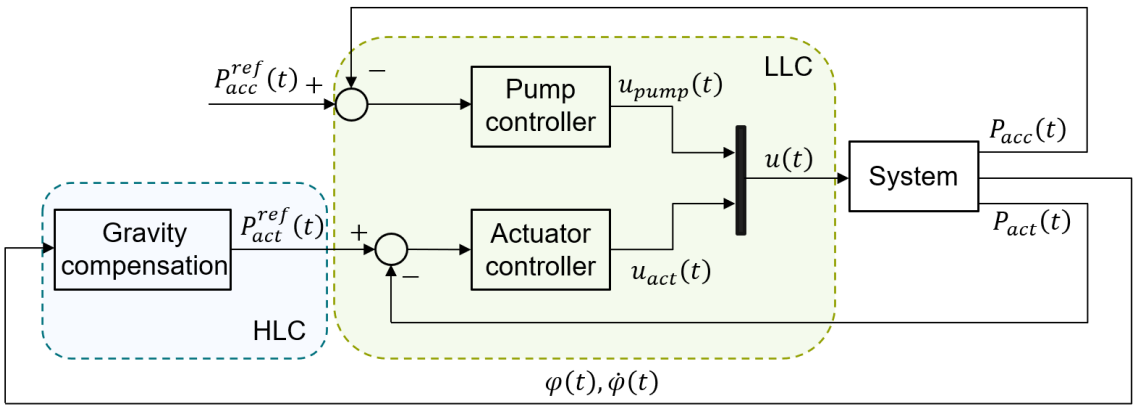


Figure 5.26: Control architecture for shoulder gravity compensation control over the soft wearable upper-limb assistive robot. The low-level controller is shaded in green and the high-level controller is shaded in blue. Variables φ and $\dot{\varphi}$ are the arm elevation angle and speed, respectively.

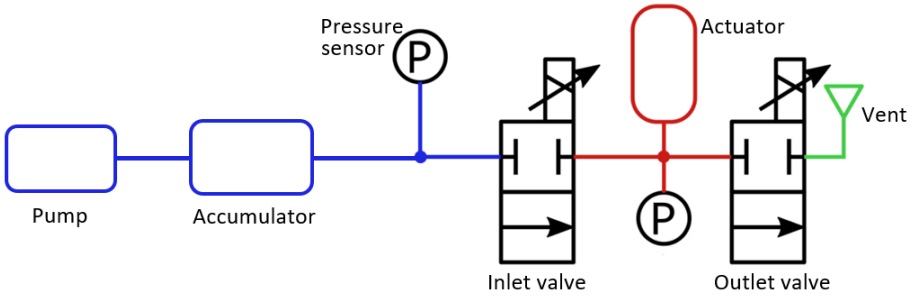


Figure 5.27: Diagram of the elements involved in one actuation channel. This is the setup used for the experimentation in this section.

is exposed. The controller design of a robot highly determines the performance of the system. Control architecture design for complex systems is typically made of different layers. High-level layers are application-focused, while low-level layers are intended to control the relevant physical variables of the system. The proposed approach was based on the design of a two layer architecture, consisting of a robust and precise low-level controller (LLC) to control the pump and actuator pressures, and a high-level controller (HLC) for shoulder gravity compensation control. The control architecture is shown in Fig. 5.26. As observed, the only external input for the controller is the accumulator pressure reference $P_{\text{acc}}^{\text{ref}}(t)$. The control diagram presents the control of just one actuator, but the actuation for both shoulders can be easily implemented via replicating the gravity compensation and actuator controller blocks. For the rest of the section, the control of one shoulder will be considered. The diagram of the pneumatic elements involved in one actuation channel are represented in Fig. 5.27.

5.4.2 Low-level control

Low-level control design is crucial, since the performance of task-focused controllers will highly depend on the low-level performance. Traditionally, prior to designing the low-level controller of a system, the system is modelled and control parameters can be selected according to a set of requirements for the desired response. However, this approach is highly imprecise and time-consuming for wearable devices, since these soft systems are highly non-linear, variant among different subjects and time-variant within a single subject due to relocation of different components, shrinks and hysteresis during its use. For these reasons, an experimental tuning is a reasonable approach for this kind of systems, as long as the control objectives are clear and a deep qualitative knowledge of the system is available. As depicted in Fig. 5.26, the low-level control of the system consists of the control of the accumulator and actuator pressures.

Accumulator pressure control

An "on-off" controller for the pump based on the pressure error in the accumulator had already been developed. The proposed control is also quite simple, being based on the previously developed control, but significantly improved. It is a combination of "on-off" and proportional controllers. The main objectives were to allow for a more constant pressure in the accumulator and increase its pressure faster. It was

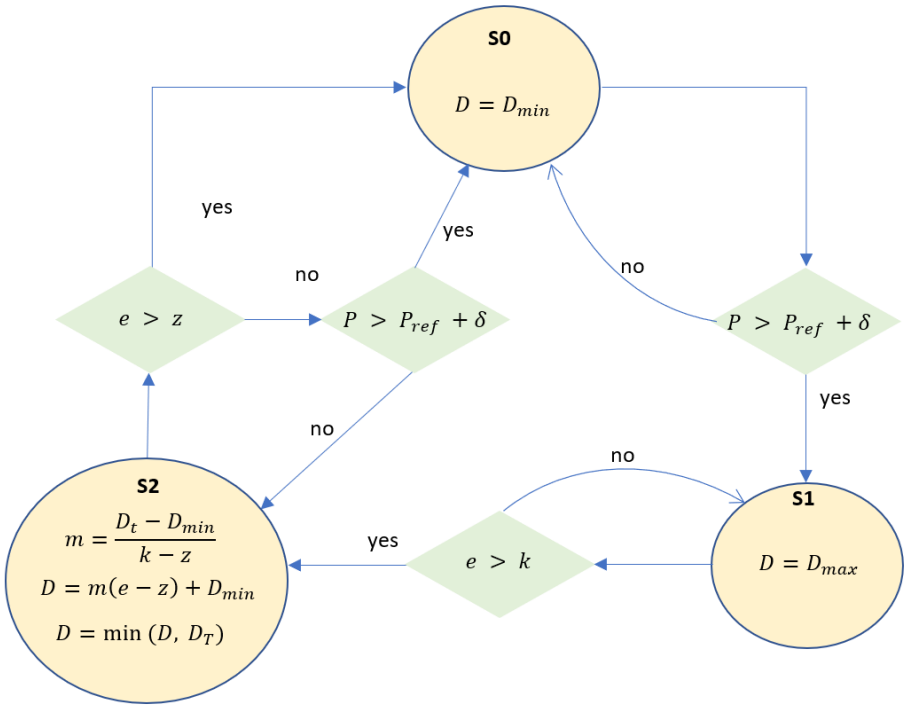


Figure 5.28: Parameters δ, k and z are thresholds used to switch between different states. As duty cycle is inverted by hardware, $D_{\min}$ is associated to full speed and $D_{\max}$ to pump off.

observed that the pneumatic circuit had very slight air leakage, so the proportional control can account for that non-desired phenomenon. On the other hand, when there is an air demand from the actuator, the "on-off" control rapidly provides maximum airflow into the accumulator.

The electronics which drive the pump were designed in a way such that the PWM signal is inverted, so maximum speed is achieved for the minimal duty cycle (achieved with the maximum PWM value $D_{\min}$) and minimal speed is obtained for maximum duty cycle (achieved with the minimum PWM value $D_{\max}$). The controller is based on a state machine with three states (Fig. 5.28). Given a reference pressure, a deadband of width δ is defined around the reference to avoid the constant switching of the pump. The state operation is as follows:

- State S0: move pump at maximum speed ($D_{\min} = 135{,}000$) until pressure reaches $P_{\text{ref}} + \delta$, then switch to S1. Deadband δ is introduced to reduce the influence of the noise in the pressure sensor.
- State S1: while measured error is within the threshold k, stop the pump ($D_{\max} = 180{,}000$). When the pressure error is beyond the threshold, switch to S2.
- State S2: apply proportional control while $e = P_{\text{ref}} - P_{\text{meas}} < z$ (z is the second pressure threshold). If the error is above z, switch to S1. If $P_{\text{meas}} \leq P_{\text{ref}} + \delta$, switch to S2. The proportional control is given by

$$D = \frac{D_{\text{T}} - D_{\min}}{k - z}(e - z) + D_{\min} \tag{5.33}$$

  where D_{T} is an intermediate duty cycle, which was experimentally adjusted to $D_{\text{T}} = 160{,}000$.

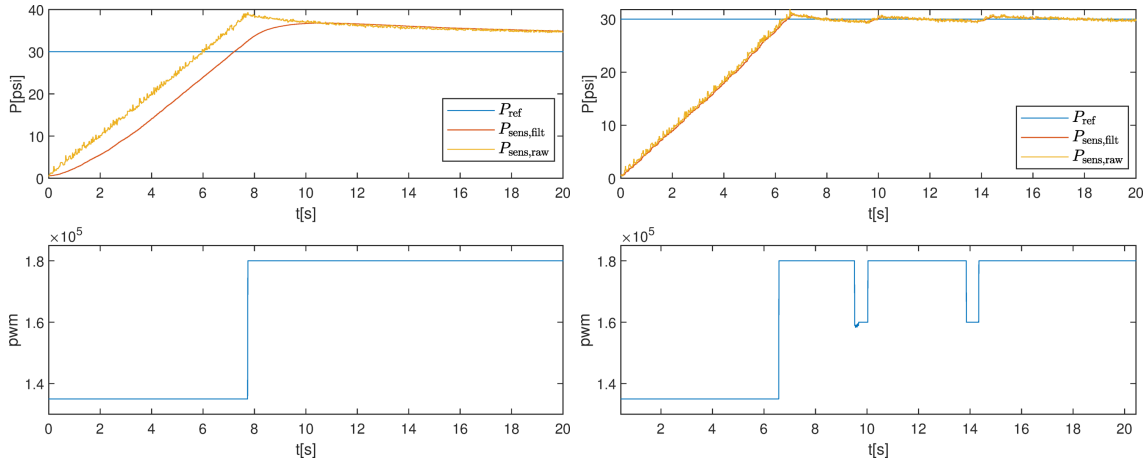


Figure 5.29: Accumulator pressure control performance: (a) "on-off" previous implementation, (b) new implementation with the state-machine controller.

The width of the deadband δ was selected as a trade-off between the amount of time the pump is working and an admissible pressure error. Similar considerations need to be done to select the values of the thresholds k and z. The reduction of the time the pump works is beneficial for saving energy. The values of these parameters were experimentally tuned to $\delta = 0.25$ psi, $k = 0.5$ psi and $z = 2$ psi.

A crucial parameter for the accumulator pressure control, apart from the proposed architecture, is the cut-off frequency of the low-pass filter applied to the pressure sensor. In the previous implementation with the "on-off" control, the cut-off frequency was too low, leading to a very smooth pressure signal, but with high overshoot. The cut-off frequency was increased to reduce the considerable delay introduced in the system and the behavior of the controller was significantly improved. A comparison of control performance using the previous and new implementations for the accumulator pressure control are provided in Fig. 5.29. Reference, raw and filtered pressure signals are represented. A reference of 30 psi was commanded and the valve that releases air into the actuator was closed. It can be observed how the new implementation generates a noisier pressure response, but with a drastically reduced filtering delay, overshoot and error. The percentage of overshoot with the old implementation was 29.93%, while with the new approach it was reduced to 4.27%.

Actuator pressure control

A PD controller with a deadband had been originally implemented for the pressure control of the actuators. The main problems observed with this controller were the tracking error, a slow response at low pressures, and a remarkable overshoot, which generated discomfort for the users, air wasting and an oscillatory behavior. Without forgetting the final goal of the gravity compensation control, these issues not only are undesirable for a pressure controller by itself but, most importantly, they are a burden for the implementation of the HLC.

The proposed approach aims to reduce the aforementioned problems by implementing a PI controller with anti-windup, maintaining the deadband. The key as-

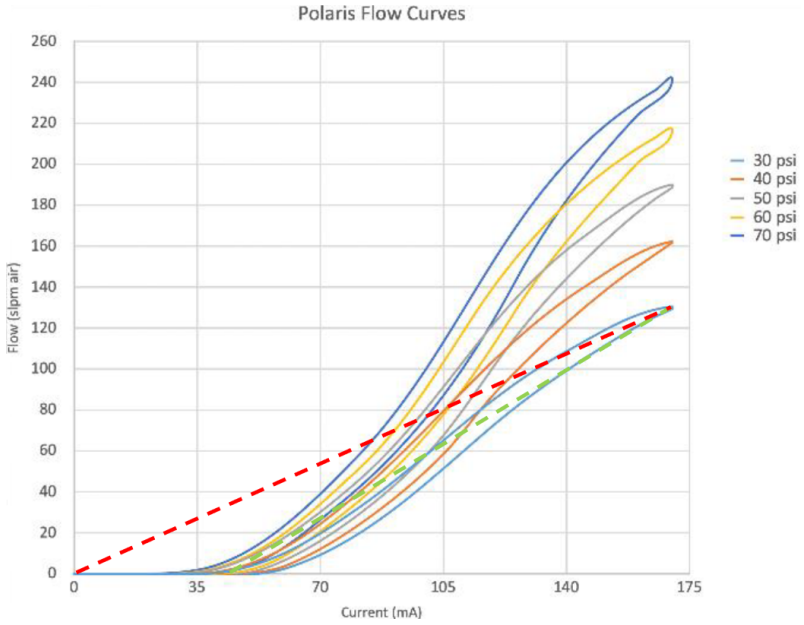


Figure 5.30: Proportional valve flow curves. The proportional valve presents a flat area for low currents that has to be considered in the control action generation.

pects which allowed to improve the performance of the actuator pressure controller are the parameter tuning (conducted experimentally), the increase of the pressure filter cut-off frequency (analogously to the accumulator pressure controller), the linearization of the proportional valves and the increase of the proportional gain at low pressures to accelerate the inflation and deflation of the actuator.

The control action applicable to the proportional valves is a PWM value between 0 and 100,000. When the control action generated by the controller is positive, it is applied to the inlet valve and the outlet valve is closed. For negative control actions, roles are switched. After the control action is computed, an offset accounting for the valve linearization is added prior to applying the action to the valve. This offset term is due to a flat area present in the proportional valve's flow curves (Fig. 5.30). The valves need a minimal current to start opening, leading to an airflow generation. If this effect is not considered, for low duty cycles there is no airflow generation, and the lower range of the control action is completely useless. The valve offset was experimentally obtained by filling the accumulator with air at a certain pressure, applying a fixed PWM value to the valve and monitoring the pressure in the accumulator after a certain amount of time to check for air leakage. This experiment was repeated for several PWM values and it was determined that an offset of 17,500 was an appropriate value (which represents a 17.5% of the control action range). Considering this effect, the controller has a more proportional behavior, as the green dashed line in Fig. 5.30 shows. Otherwise, the expected behavior is the one determined by the red dashed line, which is quite far from the real valve response. The offset was adjusted to the 30 psi curve, as it is normally the accumulator pressure. However, future work should include the influence of the differential pressure variation across the valve in the control action computation.

The control gains were set to $k_\mathrm{p} = 35,000$ and $k_\mathrm{i} = 8,000$. However, for actuator pressures under 1 psi, the proportional gain is set to $k_\mathrm{p} = 55,000$. When the actuator pressures are low, a huge amount of air is necessary to generate a pressure increase,

since the actuator is fully or partially deflated. With this gain increase, the initial inflation and deflation are noticeably faster. The saturation value for the integral action was set to $i_{\text{sat}} = 17,000$ and, when the pressure error is greater than 3 psi, the increase of the integral actions is stopped. The pressure deadband was set to 0.05 psi.

To evaluate the controller's performance, a subject (1.87 m, 72 kg) wore the inflatable robot and left his arm limp. The controllers were tested with two different control references. The first of them consisted of manually commanded step-wise variations in the commanded pressure, while the second one consisted in a linear increasing and decreasing pressure sweep. This kind of reference is used for gravity compensation calibration (will be explained further on), so evaluating the controller's performance under these conditions is relevant. A comparison of control performance using the previous PD and the new PI implementations for the actuator pressure control applying the two types of inputs is provided in Fig. 5.31. Reference, raw and filtered pressure signals are plotted. A reference of 30 psi was commanded for the accumulator.

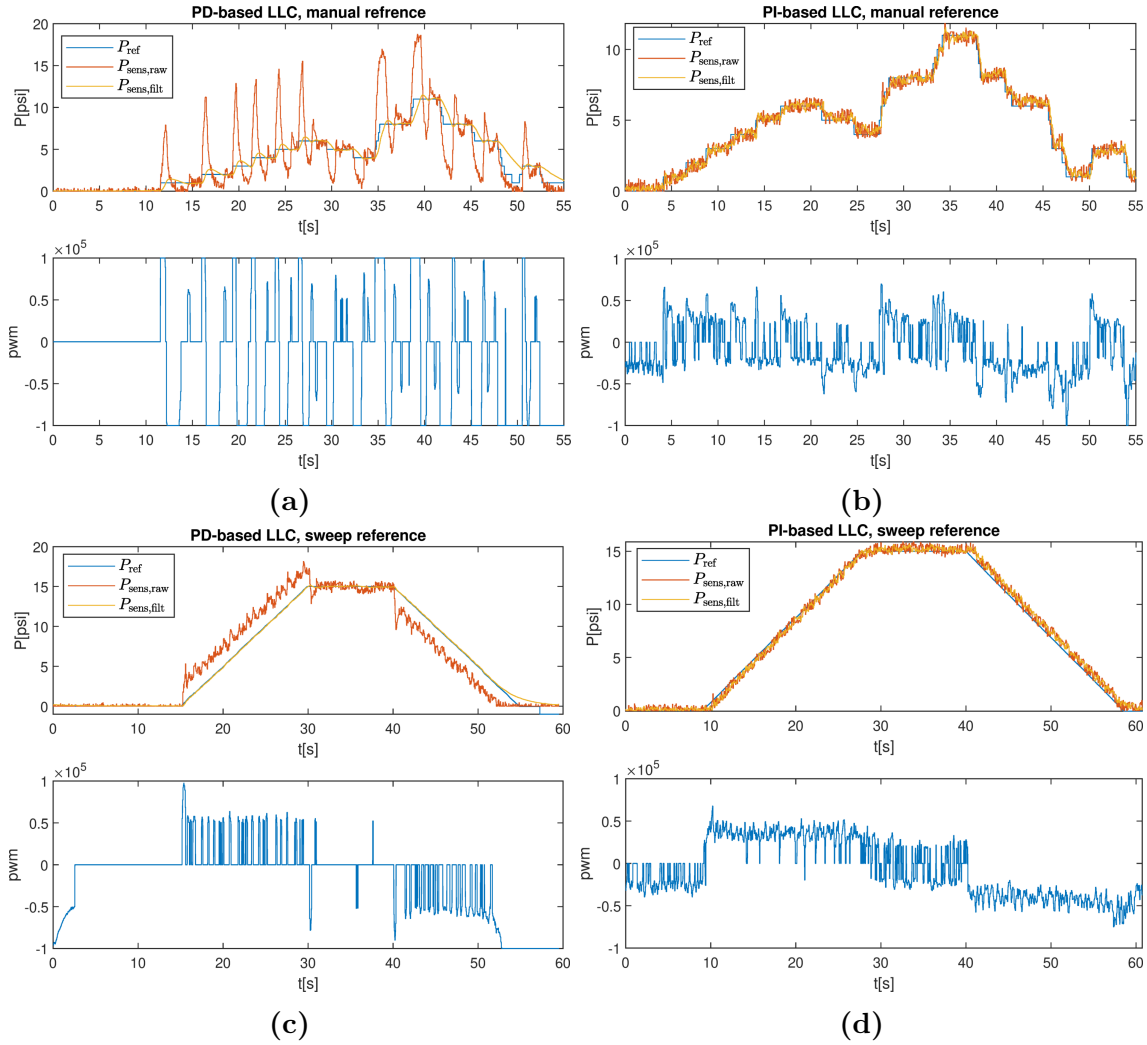


Figure 5.31: Actuator pressure control performance: (a) PD-based LLC with manual control reference, (b) PI-based LLC with manual control reference, (c) PD-based LLC with sweep control reference, (d) PI-based LLC with sweep control reference.

To compute the pressure tracking RMSEs, only the points after the initial reference was commanded were considered, eliminating in this way the influence of the initial stage in which both the commanded and sensed pressured are 0 psi. For the step-wise manual reference, the RMSEs for the PD and PI-based controllers were 2.78 psi and 0.44 psi respectively, reducing the RMSE in around 85%. When the pressure sweep reference was applied, the obtained RMSEs were 1.98 psi for the PD-based controller and 0.50 psi for the PI-based one.

As can be observed in the plots, the PD-based controller generated a massive overshoot when the commanded pressure was varied step-wise. Mainly, this was due to the delay introduced by over-filtering of the actuator's pressure signal, and was solved by increasing the cut-off frequency of the applied filter. However, the linearization of the proportional valves' behavior also contributed in reducing the overshoot. For the pressure sweep reference, the initial overshoot generated a pressure offset of around 2 psi, which was maintained during the whole pressure-increasing stage, it vanished for the constant pressure reference and it appeared again in the pressure-decreasing stage. To quantify the overshoot reduction, a test in which a step reference of 10 psi was commanded to the actuator was performed with both controllers. With the PD-based one, the percentage of overshoot was around 42%, while with the PI-based one, it was about 3%. Reducing the overshoot is a key factor for the implementation of a gravity compensation controller. This kind of high-level controller generates pressure reference commands according to the arm's angular position and speed. An overshoot in actuators' pressure at inflation or deflation leads to overshoot in arm motion, what generates misleading information on how the subject desires to move their arm, even generating instability in the system.

5.4.3 High-level control

A gravity compensation controller was implemented as HLC. This controller aims to dynamically support the user's arm by providing the estimated gravitational torque for the limb, according to the measured angle using the IMU sensor. The controller provides an angle-dependent pressure command to the actuator LLC such that the necessary torque for supporting the limb is generated. The function which relates the arm elevation angle and the necessary pressure to support it is obtained through a calibration process, in which a pressure sweep between 0 psi and 15 psi, and then back to 0 psi after a holding time (as the one shown in Fig. 5.31) is commanded. During the pressure sweep, the user is asked to leave their arm relaxed so that it is passively moved by the robot. Obtained data are fitted to two third-order polynomials, one for the inflation sweep and another one for the deflation one. According to the sense of the speed measured by the IMU and a filter, the controller determines if the inflation or deflation polynomial should be used. Then, according to the selected polynomial, the pressure command for the actuator $P_{\text{act}}^{\text{ref}}(t)$ is computed and fed to the LLC.

The gravity compensation HLC was tested with stroke survivors in the performance of several ADLs, under the guidance and supervision of an occupational therapist (OT). The PD-based LLC developed by the research group was used in these tests. During the experimentation stage, some issues with the behavior of the controller were observed. First, actuator inflation was sometimes triggered involuntarily. This was due to the fact that a slight increase in the elevation angle generated

an increase in the actuator pressure command which, due to the overshoot in the LLC, generated a too high angular increase, which at the same time increased the pressure reference and so on in a positive feedback loop. Similarly, it was observed there existed a difficulty in holding the arm at intermediate positions, as an oscillatory response, which had to be actively compensated by the user, appeared. Even full inflation or deflation were triggered. The origin of this issue relies on the imprecisions in the calibration process (hysteresis and slacks are not properly modelled by a third-order polynomial, plus, there was a too high error in pressure tracking with pressure sweep mode, as presented in Fig. 5.31c) and, again, on the LLC overshoot. Additionally, it was observed that to trigger actuator deflation, the subjects needed to apply an uncomfortable level of force, which was considerably more than what they would expect. The participants and researchers also noticed there was a delay between motion performed by the robot wearer and the inflation/deflation of the actuator. This was difficultly noticeable for slow movements and did not present a problem under those conditions, but it was specially remarkable for fast motion performed by the user.

Prior to introducing variations in the HLC, the influence of using the PI-based controller as the LLC was studied. Two different motion situations were analyzed for this purpose over one healthy subject. On the one hand, *motion M1* consisted of an elevation from the relaxed position to 70°, a stable period at 70° and a decrease to 45° (Fig 5.32). On the other hand, *motion M2* consisted of an elevation from the relaxed position to 45°, a holding time at that position and an increase to 70° (Fig. 5.33). The subject was told to leave their arm limp in the aforementioned equilibrium positions, and only applied torque for varying from one position to another. Both elevation movements were performed as shoulder abductions using both LLCs. Of course, the achieved angles were not exact, as the subject's perceived position of their arm was not perfect. However, the exact positions are not important, but how the controller responds to user motion, in terms of their intention to raise, lower or hold their arm.

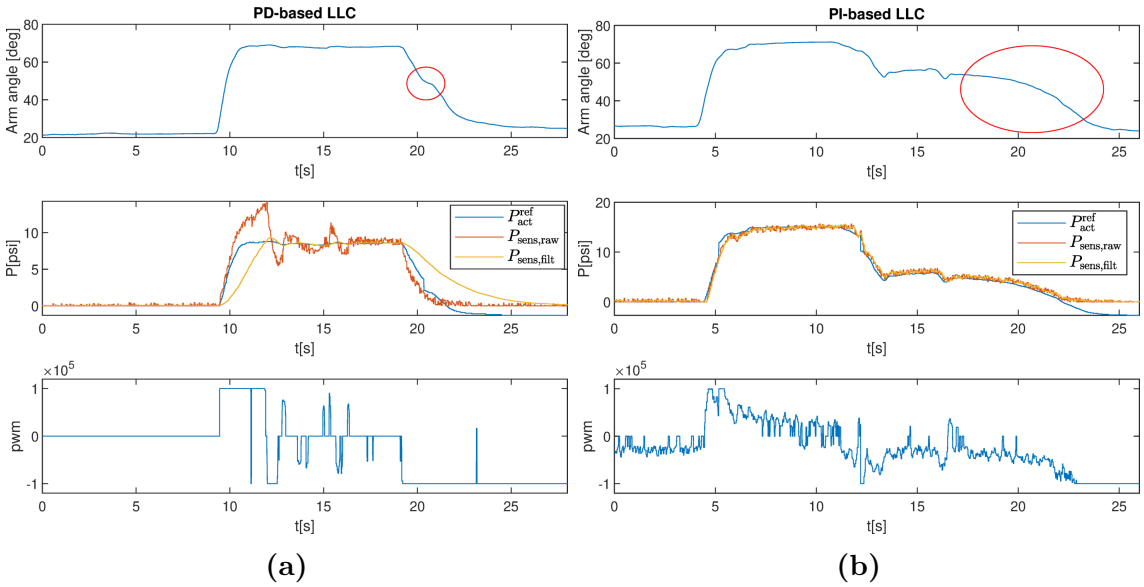
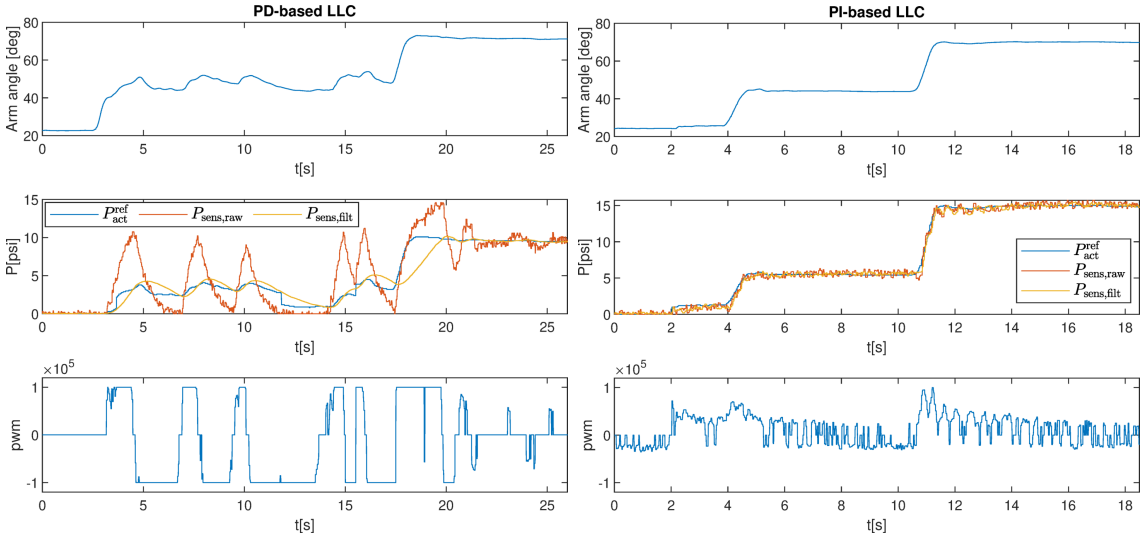


Figure 5.32: Gravity compensation control for *motion M1* using as LLC: (a) PD-based previous implementation, (b) PI-based proposed implementation.

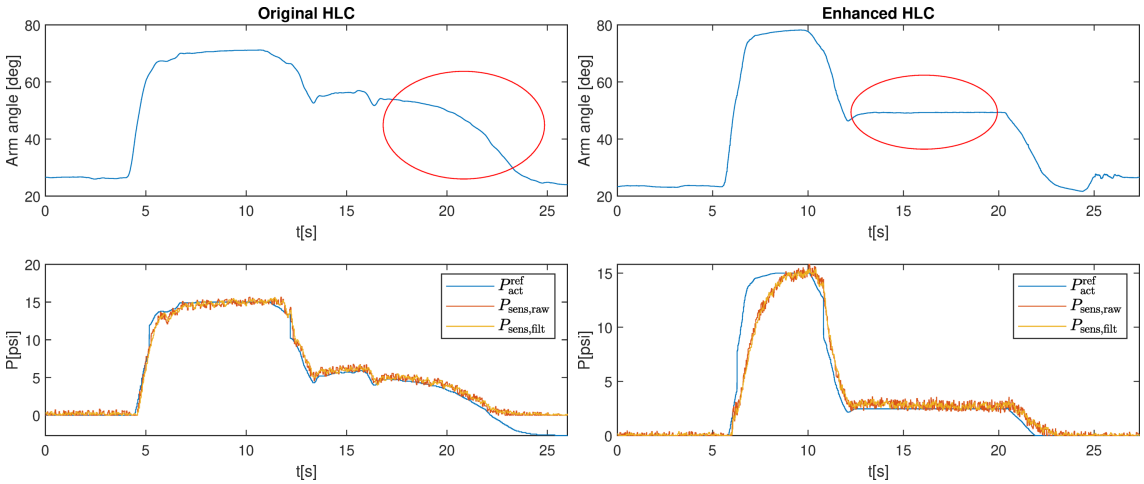


(a) **(b)**

Figure 5.33: Gravity compensation control for *motion M2* using as LLC: (a) PD-based previous implementation, (b) PI-based proposed implementation.

The main improvements introduced by the PI-based LLC are a more responsive and stable behavior. For *motion M1*, it can be observed how both LLCs allow to achieve a stable position at around 70°. However, using the PD-based LLC, the position at around 45° cannot be maintained, as marked with the red ellipse. In contrast, with the PI-based LLC, the position can be maintained for a few seconds, although a slow deflation is triggered and the arm slowly decreases its elevation angle. Regarding *motion M2*, the PI-based LLC allows to stably hold the user's arm at the intermediate position of 45° in inflation, whereas the PD-based LLC generates an oscillatory response around the 45° target equilibrium point.

The proposed PI-based LLC clearly had positive impact on the HLC performance in comparison with the PD-based LLC. However, there still were some unsolved



(a) **(b)**

Figure 5.34: Gravity compensation control for *motion M2* using: (a) original HLC, (b) enhanced HLC.

issues with the HLC performance, as the undesired slow commanded deflation that prevented achieving equilibrium at 45° in *motion M1*, the aforementioned delay in the control output and the need to apply high forces to trigger deflation. The first and second issues were addressed by introducing some modifications in the HLC, while the third one was left out of the scope of this work. To avoid the slow deflation triggered for an intermediate equilibrium point, a speed threshold was introduced. If the speed measured by the IMU is below the threshold, no pressure variation commands are fed to the LLC. The deadband generated by the introduction of this threshold allowed to hold the arm at intermediate angles without drift, as Fig. 5.34 shows, comparing the original HLC with the enhanced one, both of them using them PI-based LLC.

The elimination of the delay in the control action with respect to the user's start of motion was solved attenuating the IMU speed filter used for switching between inflation and deflation calibration profiles. A test in which several abductions between the relaxed position and angles below 45° was performed by a subject (Fig. 5.35)

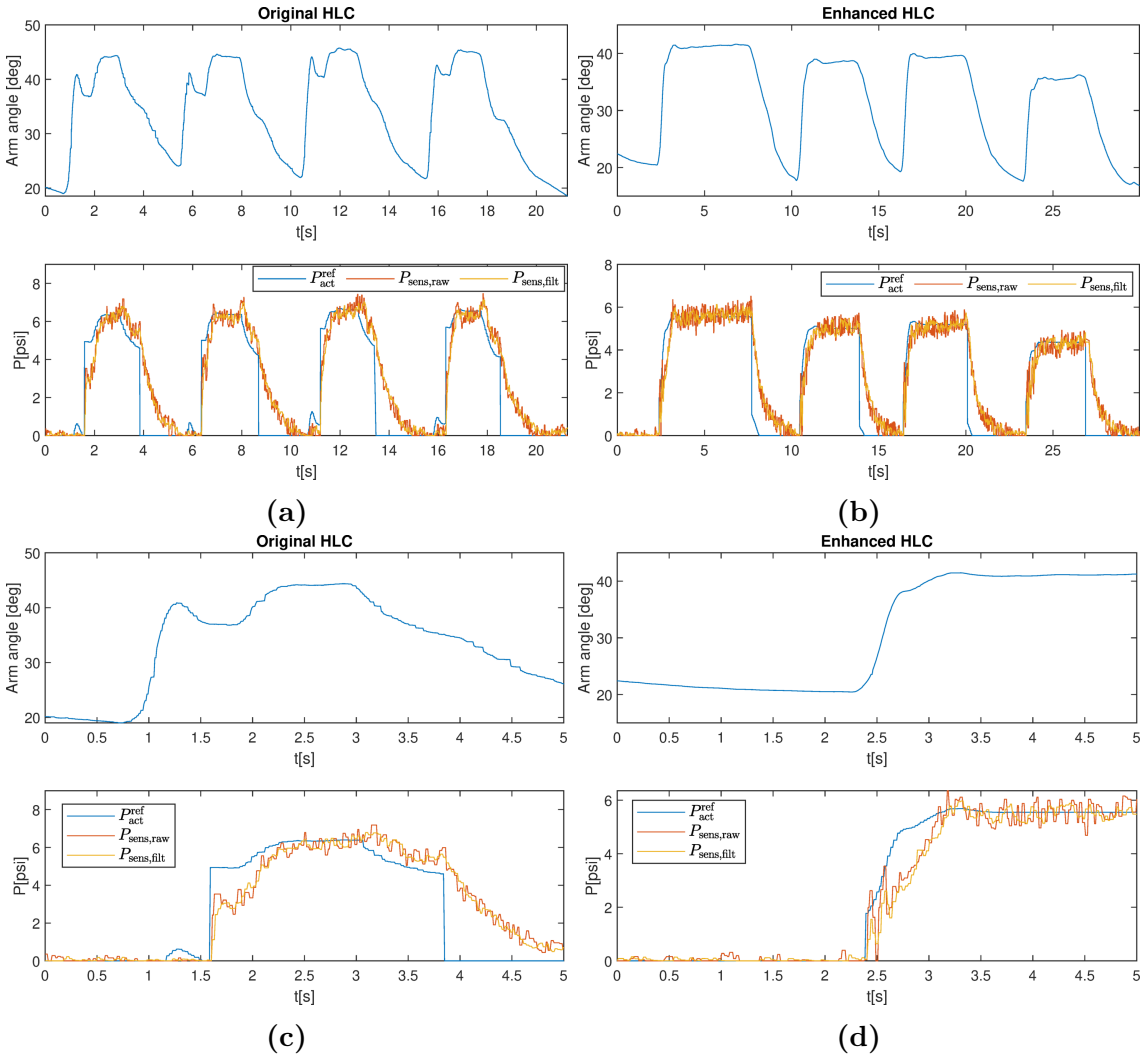


Figure 5.35: Comparison of the performance of the HLC with and without the velocity threshold and the filter attenuation: (a) original HLC data, (b) enhanced HLC data, (c) zoom-in to the original HLC data, (d) zoom-in to the enhanced HLC data.

using the HLC with and without the speed threshold and the filter reduction. It can be observed in Fig. 5.35b how the arm position is stable at the equilibrium angles (leaving the subject their arm limp) whereas the user has to generate corrections using HLC without the velocity threshold (Fig. 5.35a). In the zoom-ins presented in Fig. 5.35c and Fig. 5.35d, it is shown how the filter modification eliminated the delay between the start of motion and the trigger of the actuator pressure command. For the original HLC (Fig. 5.35c), there is a delay of around 0.8 s between the user start of elevation and the inflation command, whereas for the enhanced HLC (Fig. 5.35d), there does not exist noticeable delay.

5.5 Discussion

Control architectures for different robots developed to apply active rehabilitation have been designed in this chapter. The set of robots analyzed in this work can provide rehabilitation for pathologies of trauma origin, as well as active assistance for patients with neurological diseases, such as stroke survivors. In this context, not only the control requirements for each kind of rehabilitation are different, but also the structure and actuation system of each of the robots had a key influence in the controller design. Three different control architectures were designed for three different robots intended for three different types of active assistance (direct drive elbow rehabilitation, cable-driven shoulder rotation rehabilitation and pneumatic-actuated active assistance in ADLs). Hence, a broad and diverse picture of control architectures for active rehabilitation has been provided through the design of impedance, force and gravity compensation controllers.

The controller should always be developed according to the application target for the robot and its electromechanical characteristics. As a clear example of this, an impedance controller based on a complex motion inner-loop was proposed for the elbow rehabilitation exoskeleton. In that context, the design of a complex controller was justified by high precision requirements and the good capabilities DC motors have to be driven to an exact position. In contrast, for the soft inflatable wearable robot, a PI-based controller was enough as the LLC implementation since pneumatic systems are much less precise and fast than the ones driven by DC motors.